Mitigation of Geyser Boiling in a Gravity Heat Pipe

By

Reem AlRashed

Department of Mechanical Engineering
McGill University, Montréal
June, 2021

A thesis submitted to

McGill University

in partial fulfilment of the requirements for the degree of

Master of Science (M.Sc.) in Mechanical Engineering

Abstract

Gravity heat pipes (GHPs) are closed two-phase (liquid-vapor), gravity-driven, wickless thermosyphons, constructed by first evacuating and then filling a straight closed tube with a suitable amount of a working fluid. Heat input to the lower section of the tube (evaporator) causes the liquid phase of the working fluid to evaporate; the generated vapor (density significantly lower than that of the liquid) moves upwards through the evaporator and the central (effectively adiabatic) sections, and then condenses in the cooled upper section of the tube (condenser); the liquid condensate returns to the evaporator under the action of gravity; and this cycle continues. Very high values of the overall conductance (significantly greater than equivalent copper rods), one-way or thermal-diode-like operation, simple construction with no moving mechanical parts, and a wide operating-temperature range make GHPs very attractive for use in a variety of thermal energy systems: examples include HVAC (heating, ventilating, and air-conditioning), thermal energy storage, permafrost preservation, and geothermal systems. However, at relatively low rates of heat input and fill ratio (liquid volume/evaporator volume) close to or greater than one, GHPs could operate in an intermittent and chaotic manner, due to a phenomenon called geyser boiling: alternating periods of relatively quiescent (pool) and almost explosive boiling (the latter caused by slugs of superheated vapor moving through the liquid pool in the evaporator towards the condenser). In this research, an available GHP operating with water was modified (enhanced) and used in an experimental investigation of its characteristics and four proposed techniques for the mitigation of geyser boiling. A description of this GHP, an overview of the experimental investigation, and a discussion of some key findings and results are presented in this thesis.

Résumé

Les caloducs par gravité (CG) sont des thermosiphons biphasés (liquide-vapeur), entraînés par gravité, sans mèche, construits en évacuant d'abord puis en remplissant un tube droit fermé avec une quantité appropriée d'un fluide de travail. L'apport de chaleur à la partie inférieure du tube (évaporateur) provoque l'évaporation de la phase liquide du fluide de travail; la vapeur produite (dont la densité est considérablement inférieure à celle du liquide) se déplace vers le haut par l'évaporateur et la section centrale (efficacement adiabatique), puis se condense dans la partie supérieure refroidie du tube (condenseur); le condensat liquide retourne le long de la surface intérieure du CG jusqu'à la section d'évaporateur sous l'action de la gravité; et ce cycle se poursuit. Des valeurs très élevées de la conductance globale (nettement supérieures à celles des tiges de cuivre équivalentes), un fonctionnement unidirectionnel ou de type diode thermique, une construction simple sans pièces mécaniques mobiles et une large plage de températures de fonctionnement rendent les CG très attractifs pour une utilisation dans une variété de systèmes d'énergie thermique : les exemples incluent le CVC (chauffage, ventilation et climatisation), le stockage d'énergie thermique, la préservation du pergélisol et les systèmes géothermiques. Cependant, à des taux d'entrée de chaleur relativement faibles et à un taux de remplissage initial (ou statique) (volume de liquide / volume d'évaporateur) proche ou supérieur à un, les GHP pourraient fonctionner de manière intermittente et chaotique, en raison d'un phénomène appelé ébullition du geyser : en alternant des périodes de bassin relativement calme et d'ébullition presque explosive (cette dernière est causée par des masses de vapeur surchauffée se déplaçant rapidement à travers le bassin de liquide, de l'évaporateur vers le condenseur). Dans cette recherche, un CG disponible fonctionnant avec de l'eau a été entièrement rénové, amélioré (en mettant en œuvre certaines modifications importantes) et utilisé dans une étude expérimentale sur ses caractéristiques et quatre techniques différentes proposées pour l'atténuation de l'ébullition du geyser. Les descriptions de la configuration expérimentale globale, du CG, des procédures expérimentales, de l'étude complète, des résultats et des principales découvertes sont présentées et discutées dans cette thèse.

Dedication

This work is dedicated to …

My backbone, and the greatest engineer I have ever known who first guided me to 'brainstorming', who believed in the richness of learning, and who always encouraged me to chase my scientific curiosity seeking logical answers.

My dear mom, **Hend AlMahteb**.

My soulmate, other half, and mentor who always enriched our convos by pouring his wisdom in, concluding with a whisper in my ears 'I believe in you, and you can do it'.

My big heart spouse **Sulaiman AlJalahmah**.

The positively inspiring father figure, who was always onboard a flight heading to (YUL) airport before we even attempt to hang up the call asking to send help.

My loving dad-in-law **Mohammad AlJalahmah**.

The ones whom I'm always complete when surrounded with, and whom I never feel the time when in their company.

My support system, the amazing siblings **Rashed**, **Ali**, **Dana**, **Dalal** *and* **Abdulaziz AlRashed**.

The sparkling tiny shiny stars in my sky, who, despite the very challenging times, never failed filling my heart with endless joy, warmth, and loads of love, and who pushed me keep going every single time when their little hands get all around my neck looking right in my eyes and telling me with a heart melting smile

'you're the best mom in the whole wide world'.

My handsome sons **Mohammad, Bishr**, *and* **Bader AlJalahmah.**

May you never stop learning, Amen.

..

My gratitude to your ultimate support, endless tolerance, and great inspiration throughout this entire journey as without your unconditional love, this work would have never been completed.

Acknowledgement

First and foremost, praises to Allah, the Almighty, for the showers of blessings throughout times spent away from home, and during the work of this research.

I would like to express my appreciation to my homeland, *Al-Kuwait*, for the financial support provided via The Public Authority of Applied Education and Training (*PAAET*), and The Embassy of Kuwait -Kuwait Cultural Office (*KCO*) in Ottawa, and for granting me a fully funded scholarship throughout the entire academic stay in Montréal, Canada.

I owe my deepest gratitude to my great academic supervisor Professor B. Rabi Baliga for his continuous enthusiasm, encouragement, support, and guidance during this challenging experimental based research. His scholarly knowledge, valuable inputs, and positive critical reviews made significant influence in shaping many of the concepts delivered in this work. It was an honor to work under his supervision and getting to hear the interesting stories and inspiring quotes he used to share with his students.

Furthermore, I am thankful to my colleagues in the Heat Transfer Laboratory research group, and all other friends in MD 371 for the beneficial academic knowledge and scientific discussions, great shared times, and cultural experiences we exchanged in overall.

For all the assistance related to graduate studies at McGill, thanks go to Ms. Anne-Marie Pierre, and all other staff members of the Department of Mechanical Engineering at McGill University.

In addition, I would like to thank Mr. Ariel Kemer and the technical staff at Exatec Atelier D'Usinage for machining the components required for the experimental runs at rather rapid pace and high quality of finishing.

This journey could not have been completed without having my extended family in Montréal who always accommodated my little sons and myself with their wide open hearts as well as their homes, Reem AlNusif and her spouse Dr. Meshal AlJassar, and Sara AlHuwaitan and her spouse Dr. Ali AlAjmi. In addition to my academic trip mate Fatima Hubaishi who almost never rejected an offer to sharing a warm cup of coffee among the long winter nights and who was always there when needed.

Finally, I would like to thank my siblings, my family, my in-laws, and my friends for all the prayers, support, and encouragement since I started pursuing this degree at McGill.

Table of Contents

Nomenclature, Abbreviations, and Acronyms

Bo	Bond number
Bo_{D_d}	Bond number based on the bubble departure diameter
$\{Bo\}_{Evap}$	Bond number in the evaporator section of the GHP
$c_{p,l}$	Liquid specific heat at constant pressure [J/kg.K]
$c_{p,s}$	Solid (wall of GHP containment tube) specific heat at constant pressure [J/kg.K]
C_{loss}	Overall heat-loss conductance of the GHP [W/ºC]
C_{GHP}	Conductance of the GHP [W/ºC]
$C_{s,f}$	Boiling coefficient for the surface-liquid combination (in Rohsenow correlation)
Co	Confinement number
D_i	Inside diameter of the GHP tube [m]
D_o	Outside diameter of the GHP tube [m]
D_d	Bubble departure diameter [m]
D_{perf}	Diameter of perforations in bubble-breaker disk [m]
$D_{departure\,bubble\,mesh}$	Bubble effective departure diameter through the mesh [m]
$D_{\substack{max\ departure\\ bubble\ mesh}}$	Maximum effective departure diameter of the bubble through the mesh [m]
FR	Fill ratio
g	Gravitational acceleration on earth [m/s^2]

Gr_M	Modified Grashof number
Ga	Galileo number
$\{Gr\}_{Evap;Cond}$	Grashof number in the evaporator and condenser sections of the GHP
h	Heat transfer coefficient [W/m^2.K]
h_x	Local heat transfer coefficient [W/m^2.K]
h_{av}	Average value of heat transfer coefficient [W/m^2.K]
h_{fg}	Latent heat of vaporization [J/kg]
h'_{fg}	Modified latent heat of vaporization [J/kg]
$H_{vert\,interval,disks}$	Vertical interval between the circular surfaces of adjacent disks [m]
Ja	Jacob number
$\{Ja\}_{Evap;Cond}$	Jacob number in the evaporator and condenser sections of the GHP
k_l	Thermal conductivity of the liquid [W/m.K]
k_s	Thermal conductivity of the solid (wall of GHP containment tube) [W/m.K]
L	Length of the plate [m]
$L_{Adiabatic}$	Length of the adiabatic section of the GHP [m]
$L_{Condenser}$	Length of the condenser section of the GHP [m]
$L_{Evaporator}$	Length of the evaporator section of the GHP [m]
L_{Total}	Total length of the GHP [m]

P_{atm}	Atmospheric pressure [Pa]
$\overline{P}_{cond}^{vapor}$	Time-averaged absolute vapor pressure in the condenser section of the GHP used in this work [mbar]
P_{sat}	Saturation pressure [Pa]
P_v	Absolute pressure of the vapor [Pa]; and in Equation (2.4) [bar]
Pr	Prandtl number
Pr_l	Prandtl number of the liquid
$\{Pr\}_{Evap;Cond}$	Prandtl number of the liquid in the evaporator and condenser sections of the GHP
q_{input}	Heat input [W]
q_{loss}	Rate of heat loss from the GHP to the ambient [W]
$q^{"}_{max}$	Maximum heat flux [W/m^2]
$q^{"}_{min}$	Minimum heat flux [W/m^2]
$q^{"}_{s}$	Heat flux at the surface [W/m^2]
Re	Reynolds number
Re_{film}	Condensate film Reynolds number
t	Time [s]
t_{period}	Time period [s]
T	Temperature [^{o}C]

T_l	Temperature of the bulk liquid [ºC]
T_s	Surface temperature [ºC]
T_{sat}	Saturation temperature [ºC]
$T_{sat,abs}$	Absolute value of the saturation temperature in Equation (2.3) [K]
T_{wall}	Wall temperature [ºC]
T_{WB}	Time-averaged temperature of the inlet water to the cooling jacket [ºC]
$\overline{T}_{cond}^{vapor}$	Time-averaged vapor temperature in the condenser section [ºC]
$\overline{T}_{cond}^{wall}$	Spatial- and time-averaged outer-tube-wall temperature of the condenser section [ºC]
$\overline{T}_{evap}^{wall}$	Spatial- and time-averaged outer-tube-wall temperature of the evaporator section [ºC]
$\overline{T}_{evap}^{water}$	Time-averaged temperature of the liquid water in the evaporator section [ºC]
$T_{\infty,adiab}$	Time-averaged ambient temperature adjacent to the adiabatic section [ºC]
$T_{\infty,cond}$	Time-averaged ambient temperature adjacent to the condenser section [ºC]
$T_{\infty,evap}$	Time-averaged ambient temperature adjacent to the evaporator section [ºC]
$\overline{T}_{\infty}$	Spatial- and time-averaged ambient temperature [ºC]
ΔT_e	Excess temperature: $(T_s - T_{sat})$ [ºC]
$(\Delta T)_{max}$	Maximum temperature variation on outside wall of the evaporator tube [ºC]
$(Vol)_{between\ solid\ components\ in\ Evap}$	Volume between solid components in the evaporator section of the GHP [m^3]

$(Vol)_{liquid\ pool}$	Volume of the liquid pool [m^3]
$Vol_{\substack{max\ departure \\ bubble\ mesh}}$	The maximum bubble volume departing through the mesh [m^3]
x	Specific indicated distance from the edge of a flat plate [m]

Greek Notation

α_l	Thermal diffusivity of the liquid [m^2/s]
Γ	Mass flow rate per unit of circumference [kg/s.m]
θ	Angle of tilt of the GHP from the vertical [degrees]
θ_B	Bubble contact angle [degrees]
λ_c	Capillary length [m]
μ_l	Dynamic viscosity of the liquid [kg/m.s]
ρ_l	Density of the liquid [kg/m^3]
ρ_s	Density of the solid (wall of GHP containment tube) [kg/m^3]
ρ_v	Density of the vapor [kg/m^3]
σ	Surface tension at the liquid vapor interface [N/m]

Abbreviations

Abs	Absolute
Adiab	Adiabatic section of the GHP
Cond	Condenser section of the GHP

Evap	Evaporator section of the GHP

Acronyms

8DSLWM	Eight-disks-single-layer-wire-mesh technique for mitigating GBP in the GHP
10D	Ten-disks technique for mitigating GBP in the GHP
GBP	Geyser boiling phenomena
GHP	Gravity heat pipe
SLWM	Single-layer-wire-mesh technique for mitigating GBP in the GHP
TLWM	Triple-layer-wire-mesh technique for mitigating GBP in the GHP

Chapter 1: Introduction

1.1 Background, Overall Goal, and Motivation

Gravity heat pipes (GHPs) are closed two-phase (liquid-vapor), gravity-driven, wickless thermosyphons [Lee and Mittal (1972); Chi (1976); Faghri (1995, 2012); Reay et al. (2013); Jafari et al. (2016)]. GHPs are constructed by first evacuating and then filling a straight closed tube with a suitable amount of a working fluid. A GHP and some of the thermofluid phenomena that take place within it are schematically illustrated in Figure 1.1: the heated bottom portion of the GHP tube serves as an evaporator; the cooled upper portion of the tube serves as a condenser; and the central portion of the tube is usually very well insulated and referred to as an adiabatic section. GHPs have features that make them very attractive for use in a wide variety of engineering systems: examples include HVAC (heating, ventilating, and air-conditioning), thermal energy storage and control, permafrost preservation, geothermal, heat recovery, and electronics and fuel-cell cooling systems. These points are elaborated later in this section. For the author, the *main motivation* for learning about and investigating GHPs is her desire to participate in current worldwide efforts to enhance the efficiency of HVAC and energy conversion systems, propose novel “green-energy” systems, and find ways to reduce or even reverse global warming and climate change (as elaborated in the *Montreal* and *Kyoto Protocols* and the *Paris Agreement*), particularly in her home country of Kuwait [Al-Marafie et al. (1989); Alklaibi (2008); Firouzfar et al. (2011); Alotaibi (2011); Al-Mudhaf et al. (2013); Choudhari and Sapali (2017); Nethaji and Mohideen (2017)].

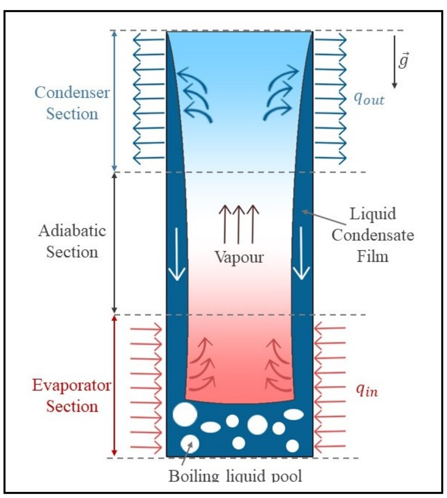

Figure 1.1 Schematic illustration of a gravity heat pipe.

GHPs are designed to operate continuously as follows [Lee and Mittal (1972); Shiraishi et al. (1981); Reed and Tien (1987); Faghri (1995, 2012, 2014); Dunn and Reay (2012); Reay et al. (2013); Naresh and Balaji (2017)]: the heat input to the evaporator causes the liquid contained within it to boil or evaporate; the resulting vapor (being lighter than the liquid) moves upwards and then condenses in the condenser section; the condensate returns to the evaporator under the action of gravity; and this cycle continues. However, at relatively low rates of heat input and fill ratio (liquid volume/evaporator volume) close to or greater than one, GHPs could operate in an intermittent and chaotic manner, due to a phenomenon called *geyser boiling* [Griffith (1962); Murphy (1965); Niro and Beretta (1990); Noie (2005); Jafari et al. (2016, 2017); Alammar et al. (2018a, 2018b); Pabon et al. (2019)]: it involves alternating periods of relatively quiescent (pool) and almost explosive boiling (the latter caused by slugs of superheated vapor moving through the liquid pool in the evaporator towards the condenser). Additional discussions of the geyser boiling phenomenon (GBP) are given later in this chapter. It should be noted here that the GBP in GHPs could lead to repeated impact loads on the cap of the condenser section, large intermittent and chaotic (but cyclical in an overall sense) variations in the tube-wall temperatures (which, in turn, lead to cyclical thermal stresses and the associated risks of fatigue-induced brittleness and cracks), and vibrations of the GHP [Jafari et al. (2017); Techio et al. (2017)]. *The overall goal of the work presented in this thesis* was to propose and assess techniques to mitigate the GBP in a GHP.

As boiling and condensation processes are associated with relatively high latent heat and effectively constant temperatures (for pure substances), GHPs can sustain high rates of heat transfer with relatively small temperature differences. In other words, their overall (or effective) thermal conductance is very high. Furthermore, as GPHs are only partially filled with the liquid phase of the working fluid (primarily in the evaporator section), their heat capacity and thermal response time are quite low. Typically, their overall thermal conductance is significantly higher, and their thermal response time is considerably smaller, than those of solid copper rods of corresponding dimensions. It is also important to note that GHPs function (under the influence of gravity) only when their condenser section is at a higher elevation than their evaporator section, a feature which is often referred to as a thermal-diode behavior; and GHPs are simple to construct, have no mechanical moving parts, and can operate over a wide temperature range (with the proper choice of working fluid and operating pressure).

The above-mentioned features of GHPs have made them very attractive for use in many engineering systems: examples include heating, ventilating, and air-conditioning (HVAC) and waste heat recovery systems [Azad and Geoola (1984); Azad et al. (1985); Wadowski et al. (1991); Yang et al. (2003); Lin et al. (2005); Danielewicz et al. (2014)]; solar energy systems [Mathioulakis and Belessiostis (2002); Abreu and Colle (2004); Hussein et al. (2006); Du et al. (2012)]; enhanced latent-heat thermal energy storage units [Shabgard et al. (2012)]; permafrost preservation systems [Haynes et al. (1992); Xu and Goering (2008)]; geothermal systems for deicing roads and bridges [Reay et al. (2013)]; systems for regulating temperature in oil wells [Ma et al. (2013); Zhang and Che (2013)]; and systems for cooling electronic devices and fuel cells [Tsai et al. (2010); Reay et al. (2013)]. Five such applications of GHPs are illustrated in the following figures borrowed from Boopathy (2017): Fig. 1.2 (a) [taken with permission from Alyeska Pipeline Service Company, http://www.alyeska-pipe.com]; Figs. 1.2 (b), (c), and (d) [included with permission from Arctic Foundations Inc., http://www.arcticfoundations.com]; and Fig. 1.2 (e) [main ideas adapted from http://long2.eng.sunysb.edu/project/thermosyphon.html].

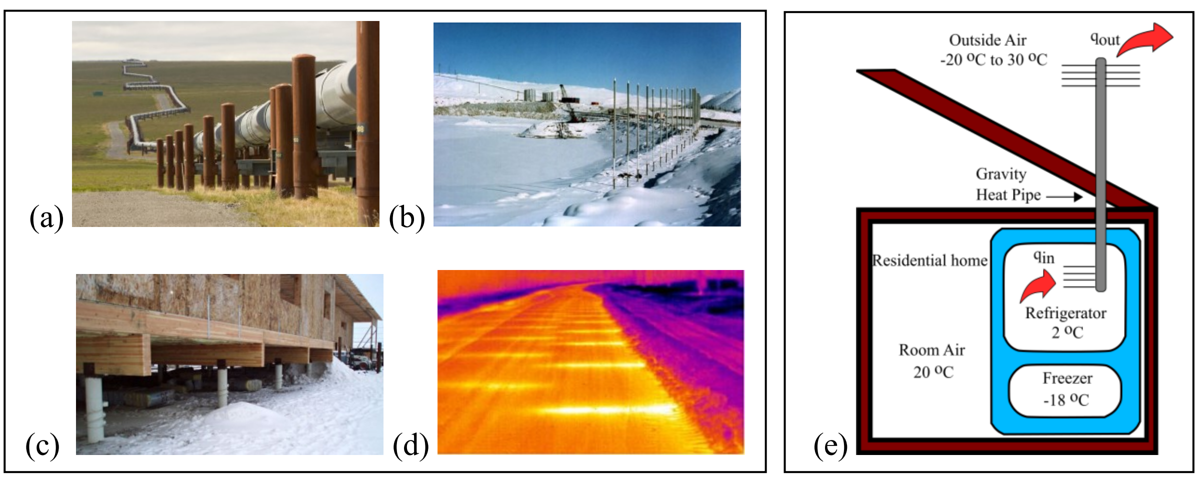

Figure 1.2 Some applications of GHPs: (a) thermopile support posts of the Trans-Alaska Pipeline (designed to preserve the permafrost); (b) creation of a frozen-soil wall for containment of hazardous wastes at the Kubaka gold mine in Russia; (c) thermo-helix-piles designed to strengthen the building foundation of a clinic in Selawik, Alaska, by freezing water in the soil underneath it; (d) infrared image of road de-icing using fully-buried GHPs for harnessing geothermal energy at the University of Alaska, Fairbanks; and (e) a GHP-assisted residential refrigerator designed for cold-climate locations (main ideas adapted from a set-up illustrated in the webpage of Professor J. P. Longtin's laboratory at the State University of New York, Stony Brook).

The above-mentioned and other similar engineering applications of GHPs demonstrate that they have the potential to provide significant socio-economic and environmental benefits, and thus play an important role in sustainable engineering and design. Such potential benefits of GHPs (coupled with the desire on the part of the author and her supervisor, Professor B. R. Baliga, to contribute to ongoing worldwide efforts directed towards designing efficient, sustainable, and environmentally friendly energy conversion and exchange systems) constitute the main motivation for the work described in this thesis.

1.2 Literature Review

There are numerous publications on GHPs, their various applications, and related topics. An exhaustive review of this extensive amount of literature related to GHPs is not intended here. Only a concise overview of some key books, review articles, and papers (on GHPs, boiling, condensation, and some related topics) that were directly used in the planning and execution of the work reported in this thesis is presented in this section.

1.2.1 Historical development, books, and review articles related to GHPs

The Perkins tube [Perkins (1836)], a wickless gravity-assisted heat pipe made of a closed tube containing a small quantity of water and operating as a two-phase thermosyphon, is a predecessor of modern-day GHP. Some of its applications were in locomotive boilers and fire-box superheaters. Descriptions of the Perkins tube are available in the works of King (1931) and Reay et al. (2013).

In contrast to GHPs, which are wickless gravity-driven devices, conventional heat pipes are driven by capillary forces produced at the liquid-vapor interface in a wick, or porous lining, attached to the inside surface of the tube. They will be referred to in the rest of this thesis as simply ‘heat pipes’, or abbreviated as HP. The key concept and operational aspect of heat pipes was first put forward in a US patent granted to Gaugler (1944). However, the term ‘Heat Pipe’ was coined by Grover (1963) in a US patent described in the context of a refrigeration system. Extensive research and development of heat pipes were conducted at the Los Alamos Laboratory in New Mexico, under the supervision of G. M. Grover: several prototype heat pipes were built with water as a working fluid; they were soon followed by a heat pipe operating with sodium at a temperature of about 1100 K [Grover et al. (1964)]. Preliminary theoretical results and design tools included in a report by Cotter (1965) established the heat pipe as a reliable and useful device with high thermal conductance and no mechanical moving parts. Numerous research works on heat pipes were initiated around the world following the publication of the report by Cotter (1965), as described in Reay et al. (2013): experiments with sodium heat pipes for use as thermionic diode converters were initiated at the United Kingdom Atomic Energy Laboratory at Harwell; similar work was also started at the Joint Research Centre (JCR) in Ispra, Italy, which soon became the most active research center on heat pipes outside the U.S.; and shortly after that, research activities on heat pipes were initiated in Germany, France, the former USSR, and several other countries.

As HPs are capillary-driven devices, they can operate in micro-gravity locations. Thus, most of the early research and development efforts on HPs were related to space applications, and the first space flight of a HP pipe took place in 1967 [Reay et al. (2013)]. Today, however, research, development, and commercialization of HPs for space as well as terrestrial applications are being carried out in many countries around the world, as is demonstrated by the numerous papers on these devices that have appeared in the published literature.

There are many books and review articles on HPs and GHPs. Examples of such publications include the works of Tien (1975), Chi (1976), Faghri (1995, 2012, 2014), Peterson (1998), Dunn and Reay (2012), Reay et al. (2013), Shabgard et al. (2015), Jafari et al. (2016), and Nethaji and Mohideen (2017).

1.2.2 Boiling phenomena

Liquid-vapor phase-change phenomenon is referred to as boiling when it occurs at the surface of a heated solid in contact with the fluid (liquid and vapor), and the temperature of the surface exceeds the saturation temperature of the liquid [Rohsenow (1973); Carey (1992); Whalley (1996); Hewitt (1998)]. Heat transfer from the solid surface to the liquid causes the formation of vapor bubbles (at nucleation sites), which grow and subsequently detach from the surface, and then rise through the liquid to the liquid-vapor interface.

The seminal works on boiling are those of Nukiyama (1966), first published in Japanese in 1934, and Rohsenow (1951). Nukiyama (1966) investigated boiling on the surface of an electrically heated wire immersed in water inside a container. He presented his results as a plot of the rate of heat input to the wire per unit area of its surface (heat flux from the wire surface to the water) versus the temperature of the wire. This plot is referred to today as the Nukiyama boiling curve [Rohsenow (1973); Carey (1992); Thome (2003)]. Rohsenow (1951) also investigated pool boiling and proposed an empirical correlation for the calculation of the pool-boiling heat transfer coefficient. This correlation is referred to today as the Rohsenow correlation for pool boiling [Carey (1992); Thome (2003)]. The Nukiyama boiling curve and the Rohsenow correlation for pool boiling are discussed further in Chapter 2. Correlations for free-convection and vapor-film modes of pool boiling, and also critical heat flux, are available and discussed in the published literature, for example, in the works of Rohsenow (1973), Carey (1992), and Hewitt (1998).

Extensive discussions of the various thermofluid processes involved in boiling (including the dynamics of bubble formation, growth, and detachment; and critical heat flux and burn-out), its categorization into various different regimes (such as natural-convection, nucleate-pool, and vapor-film boiling in containers or vessels; and bubbly-, slug-, churn-, and annular-flow regimes in forced convection boiling in tubes), and references to publications related to these topics, are available, for example, in the works of Fritz (1935), Cole (1967), Mikic et al. (1970), Frost and Li (1971), Rohsenow (1973), Carey (1992), Stephan (1992), Whalley (1996), Dobson and Chato (1998), Hewitt (1998), Thome (2003), Kolev (2007), and Dhir et al. (2007).

Discussions of pool boiling heat transfer phenomena in the evaporator section of GHPs, including related modelling aspects and critical heat flux, are available, for example, in the works of Casarosa et al. (1983), Imura et al. (1979, 1983), Reed and Tien (1987), Noie (2005), and Guichet et al. (2019). Extensive research on these phenomena was also carried out in the former Soviet Union: references to some of the related publications and brief reviews of them are available in the work of Casarosa et al. (1983).

There have also been many investigations of the departure diameter of the vapor bubbles and their rate of growth in pool boiling. The departure diameter is the diameter of a sphere with the same volume as that of the vapor bubble (of spherical or non-spherical shape) just after it detaches from the surface on which it was formed. Most of the published works on these topics pertain to pool boiling on horizontal flat surfaces at pressures above the standard atmospheric pressure. However, in some of the investigations, sub-atmospheric pressures, and the inner surface of tubes akin to those used for the construction of GHPs, were considered. Contributions in this area include the works of Fritz (1935), Cole (1967), Dhir et al. (2007), and Hamzekani et al. (2014, 2015). A comprehensive review of these works has been provided by Guichet et al. (2019). Some additional discussions of these topics are provided in Chapter 2.

1.2.3 Condensation phenomena

Condensation is vapor-liquid phase-change phenomenon, and it occurs when the temperature of a vapor is reduced below its saturation temperature [Rohsenow et al. (1961); Rohsenow (1985); Carey (1992); Marto (1998); Incropera and DeWitt (2002)]. It is categorized into different modes as follows [Marto (1998)]: surface condensation, which occurs when a vapor comes in contact with a cold surface; homogeneous condensation, in which the vapor condenses in the form of droplets suspended in a gas (forming a fog or mist); and direct contact condensation, which occurs when the vapor is brought in direct contact with a cold liquid. Surface condensation is the primary mode of condensation in GHPs. In surface condensation, the latent heat involved in the vapor-liquid phase-change phenomenon is released and transferred to the cooled surface, and a liquid condensate is formed on it. It can occur in two sub-modes [Marto (1998)]: film condensation, in which the condensing vapor forms a continuous liquid film on the cold surface; and drop-wise condensation, in which liquid drops are formed on the cold surface. Film condensation is the predominant mode of condensation in most engineering applications and in GHPs [Rohsenow et al. (1961); Chen et al. (1984); Carey (1992); Marto (1998); Incropera and DeWitt (2002)]. A few key publications related to film condensation, including those pertaining to its occurrence in GHPs, are reviewed in the remainder of this subsection.

The publication by Nusselt (1916) is the seminal work on film condensation. He formulated a mathematical model of laminar film condensation of a saturated vapor of a pure substance on a vertical isothermal cooled surface and solve it analytically. In this model, Nusselt (1916) invoked the following assumptions: 1) the vapor is effectively stationary far from the vertical isothermal cooled surface and the liquid condensate flows down this surface under the action of gravity; 2) the thermophysical properties of the condensate remain constant (at values pertaining to the arithmetic mean of the temperatures of the saturated vapor and the cooled isothermal surface) and those of the vapor also remain constant (at values corresponding to its saturation temperature); 3) the shear stress between the vapor and liquid condensate flowing down the vertical surface is zero (negligibly small); 4) the rates of viscous transport and heat conduction in the vertically downward direction inside the condensate layer are negligible compared to those in the direction normal to it; 5) the rates of advection transport of momentum and enthalpy in the vertically downward direction inside the condensate layer are negligible compared to the rates of viscous transport and heat conduction across it, respectively; and 6) the variation of static pressure across the downward flowing condensate layer is negligible. The analytical solution of this model obtained by Nusselt (1916) provides expressions for the velocity and temperature distributions in the condensate layer; the variations of the condensate-layer thickness and mass flow rate with the downward distance along the plate starting from its upper edge; and the local and average values of the heat transfer coefficient. Additional details of the results obtained by Nusselt (1916) are presented in Chapter 2. Even though Nusselt proposed his model and solution back in 1916, they continue to be the starting points of many of the latest works on film condensation.

Dhir and Lienhard (1971) showed that the model and solution of Nusselt (1916) can provide good predictions of laminar film condensation on the upper surface of cooled flat isothermal plates inclined at an angle θ from the vertical, by using $g\cos(\theta)$ in place of g (where g is the gravitational acceleration), provided the value of θ does not approach 90^{o}. The model and solution of Nusselt (1916) may also be used to predict laminar film condensation on the inner and outer surfaces of vertical tubes, with good accuracy, if the radius of the tube is significantly greater than the condensate film thickness throughout the length of the tube [Rohsenow (1985); Marto (1998)].

A film Reynolds number, based on the mass flow rate inside the condensate layer per unit width of the plate and the dynamic viscosity of the liquid (condensate), is used to characterize conditions that cause transitions from laminar to wavy and then turbulent film condensation: it is generally assumed that when this film Reynolds number is less than or equal to 30, the conditions correspond to laminar-wavy film condensation; and when this number is greater than or equal to about 1800, the transition from laminar to turbulent film condensation is complete [Incropera and DeWitt (2002)]. Several empirical correlations have been proposed for the heat transfer coefficient in the laminar-wavy and the turbulent regimes of film condensation [Marto (1998); Incropera and DeWitt (2002)].

Seban and Hodgson (1982) adapted the work of Nusselt (1916) for predictions of laminar film condensation in vertical tubes with upward flow of the vapor. Extensions of this work to condensation in closed vertical two-phase thermosyphons have been presented by Seban and Faghri (1984) and Chen et al. (1984). Hijikata et al. (1984) have presented an analytical investigation of the influence of a non-condensable gas on condensation in a two-phase closed thermosyphon; and a theoretical analysis and some experimental studies of film condensation inside vertical and inclined closed two-phase thermosyphons have been presented in the work of

Wang and Ma (1991). Carey (1992), Whalley (1996), Dobson and Chato (1998), and El Hajal et al. (2003) have provided models, correlations, and flow-pattern maps for forced convection condensation in horizontal tubes.

Zhou and Collins (1991) have presented measurements of condensation heat transfer in a two-phase thermosyphon. An experimental investigation of turbulent film condensation of high-pressure steam in a vertical tube, with parameters relevant to the design of passive systems in advanced nuclear power plants, has been presented by Kim and No (2000). An experimental investigation of film condensation of water in a vertical tube in the laminar, wavy, and turbulent flow regimes, accounting for the influence of the counter-current vapor flow, has been presented and discussed, along with correlations for the friction factor and heat transfer coefficient, by Thumm et al. (2001). Pashkevich et al. (2015) have presented an experimental study of film condensation in a large-diameter (200 mm) tube with upward flow of steam; and a similar study for a small-diameter (2.0 mm) tube has been presented by Kubin et al. (2016). These studies revealed that the upward flow of steam causes waves on the surface of the condensate layer, an effect that was not accounted for in the seminal work of Nusselt (1916); and increases in the rate of heat transfer by up to 20.5 % could be obtained when such waves are present.

1.2.4 Geyser boiling phenomena in GHPs

When the geyser boiling phenomenon (GBP) occurs in a GHP, it operates in an unsteady, chaotic, and roughly cyclical manner, with intermittent explosive boiling (caused by slugs of superheated vapor moving through the liquid pool in the evaporator towards the condenser). The seminal works on this topic are those of Griffith (1962) and Murphy (1965). Some other early works on this topic were done by researchers in the former Union of Soviet Socialist Republics (USSR), and they have been reviewed concisely by Casarosa et al. (1983). Another early work that reported geyser boiling was by Bezrodnyi and Beloivan (1976), who referred to it as "geysering." The GBP in GHPs occurs mostly at relatively low operating pressures, with high fill ratios (≥ 100 %; the fill ratio is defined in Equation (2.15), Subsection 2.5.2), and low power inputs to the evaporator section (insufficient for continuous pool boiling) [Casarosa et al. (1983); Kuncoro et al. (1995);Lin et al. (1995); Khazaee et al. (2010); Liu et al. (2018)].

The following description of the GBP in a long vertical tube, closed at the bottom, filled with a liquid, connected to an open reservoir at the top (partially filled with liquid), and heated on its curved surface has been adapted from the work of Murphy (1965). In the initial stages of the GBP, the heat input to the wall of the tube is transferred to the liquid by natural convection. This natural convection process establishes fluid circulation that causes a portion of the heat input to be liberated at the surface of the liquid in the reservoir (primarily by evaporation) and the remainder results in sensible heating of the liquid (in the reservoir and the tube). As the heat input to the tube wall is continued, the liquid in the upper three-quarters (or so) of the tube reaches its saturation condition. Additional heat input to this saturated liquid results in the production of vapor bubbles on the inner surface of the tube (boiling). These bubbles detach from the tube surface, rise in the liquid, and begin to coalesce and form a larger bubble, which is often referred to as a Taylor bubble in honour of G.I. Taylor [Davies and Taylor (1950)]. As the density of vapor is much lower than that of the liquid, the formation of a Taylor bubble adjacent to the wall of the tube results in a pressure reduction below the bubble; this reduction in pressure causes the liquid that resides beneath bubble to become superheated, which, in turn, increases the rate of formation of the vapor; eventually, there is an explosive expulsion upwards of the heated liquid on top of the Taylor bubble; after that, the colder liquid from the reservoir refills the tube; and the cycle repeats. A schematic representation of a similar sequence of events during one cycle of the GBP in a GHP, where the expelled liquid hits the closed top of the GHP tube and falls back into the evaporator, has been provided by Khazaee et al (2010); an adaptation of their schematic depiction, taken from the work of Boopathy (2017), is presented below in Fig. 1.3. Another impression of GBP in GHPs can be obtained from the work of Xia et al. (2017), who conducted a visualization study of the instabilities in a flat two-phase thermosyphon.

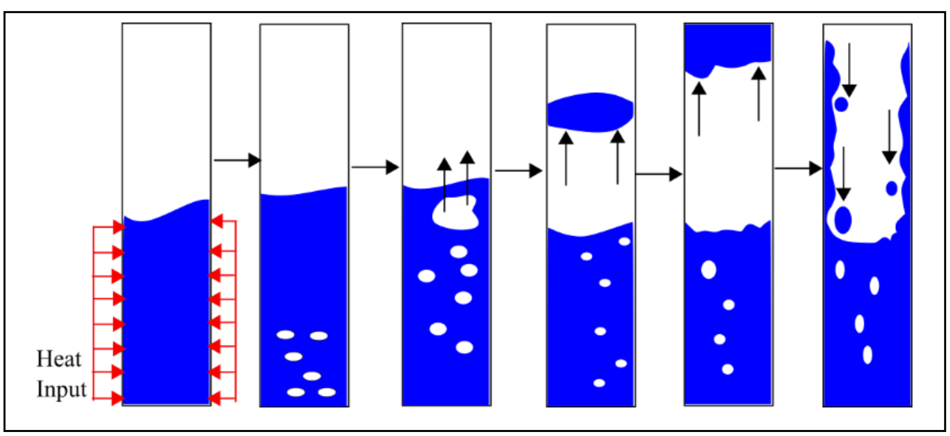

Figure 1.3 A schematic depiction of the sequence of events during the geyser boiling phenomenon in a closed two-phase thermosyphon with close to 100 % fill ratio [adapted from Khazaee et al. (2010) by Boopathy (2017)].

The parameters affecting the GBP in a GHP were investigated experimentally by Imura et al. (1983). Their experimental results agreed with the predictions of some of the previously published correlations to within ± 30 %. They also proposed a new correlation that suggests an adequate fill ratio based on the magnitude of the critical heat flux. In experiments conducted by Negishi and Sawada (1983), who described the GBP as "turbulent motion of the liquid caused by the explosive expansion of a boiling bubble" , geyser boiling was witnessed at fill ratios > 70%: it was indicated by a loud sound accompanied by tube oscillations, which were caused by the explosive expansion of the Taylor bubble and the expulsion of the liquid above it, which struck the top of the condenser section. They also reported that the GBP time period depended on the dimensions of the thermosyphon, with the eruptions in each cycle lasting for a longer time when the thermosyphon was shorter (for a fixed diameter); and this time period was reduced as the rate of heat input to the evaporator was increased. Similar conclusions were reached in the experimental investigations of Niro and Beretta (1990), Liu and Wang (1992), Kuncoro et al. (1995), Lin et al. (1995), Abreu and Colle (2004), Khazaee et al. (2010), and Smith et al. (2018a, 2018b).

In the experimental investigations of Noie et al. (2007), Emami et al. (2009), Chen et al. (2015), and Smith et al. (2016), the influences of fill ratio and the angle of inclination of the GHP on the GBP were studied. They concluded that the GBP occurred at fill ratios above 30 %; the GBP was facilitated when the GHP was close to the vertical orientation; and increasing the fill ratio increased both the period and the intensity of the GBP.

Mathematical models and numerical studies of GBP have also appeared in the published literature. Examples of such studies include the works of Shabgard et al. (2014) and Jouhara et al. (2016). Their results showed encouraging agreements with those of some of the above-mentioned experimental investigations. A combined CFD/visualization investigation of heat transfer during the GBP in a GHP has been presented by Wang et al. (2018), with encouraging agreement between the CFD predictions and the experimental results.

Over the last 10-15 years, there have been many published investigations on ways to mitigate or eliminate GBP in GHPs. The options studied in this regard include the following: 1) reducing the fill ratio; 2) increasing the inclination angle of the GHP away from the vertical orientation; 3) reducing the aspect ratio (length/inner diameter) of the core tube of the evaporator; 4) using suitable combinations of the base fluid, a chemical stabilizer, and nanoparticles as the working fluid; 5) adding surfactant to the working fluid; and 6) increasing the roughness of the inner surface of the core tube in the evaporator section. Concise discussions of these options, techniques to break up the generated bubbles before they cause geyser boiling, and a review of the key publications on these topics are postponed to Chapter 3, Section 3.6, to provide a suitable context there for introducing the techniques proposed in this work to mitigate the GBP in a GHP.

1.2.5 Operational limits of GHPs

GHPs have several operating limits that depend on many parameters, including the following: the rate of heat input to the evaporator and heat extraction from the condenser; geometric parameters (such as ratio of the tube length to its diameter; ratios of the lengths of the evaporator and condenser sections to the total length of the GHP; and inclination of the tube from the vertical); fill ratio (ratio of the volume of liquid to the total volume of the evaporator section); and thermophysical properties of the working fluid. In the published literature, these operational limits are referred to as the dry-out limit; burn-out or critical heat flux limit; flooding or entrainment limit; and sonic limit [Dobran (1985); Dunn and Reay (2012); Jafari et al. (2016)].

The dry-out limit is used to indicate one of the following conditions during the operation of the GHP [Nguyen-Chi and Groll (1981); Dobran (1985); El-Genk and Saber (1999); Dunn and Reay (2012)]: 1) amount of working fluid lower than the minimum required for a continuous circulation of the vapor and condensate at a specified rate of heat input to the evaporator; 2) a portion of the liquid condensate flowing down the wall of the tube in the evaporator section at fill ratios below 100 % evaporates at a faster rate than it can be replenished, due to either high input heat fluxes or high condensate-vapor shear stress which hinders the down-flow of the condensate; and 3) the GHP inclined with respect to the vertical and the condensate film on the inner surface of the tube is not uniform in the cross-section, due to the effects of gravity, causing portions of it to dry out.

The burn-out or critical heat flux limit is used to refer to a situation in which the rate of vapor formation on the inner surface of the evaporator tube is so high that a vapor film (or blanket) is formed there, and the heat transfer from this surface to the liquid pool has to occur through this relatively low-thermal-conductivity vapor film. It is similar to the critical heat flux limit in pool boiling [Nukiyama (1966)]. This limit usually occurs at high values of the fill ratio (close to, equal to, or higher than 100 %). The related details are available in the works of Dobran (1985), Dunn and Reay (2012), and Jafari et al. (2016).

The flooding or entrainment limit can occur at high fill ratios and large rates of heat input. It refers to the following conditions: 1) the high vapor flow rate which leads to high shear stress at the vapor-condensate interface, causing it to become unstable and wavy; and 2) as the heat input is increased further, the liquid in the condensate layer becomes entrained into the core vapor flow, causing flooding conditions in the tube, especially if it is of small diameter [Nguyen-Chi and Groll (1981); Dobran (1985); El-Genk and Saber (1997)].

The sonic limit refers to the following conditions: the vapor velocity reaches sonic (or supersonic) levels (during start-up or steady-state operation of the GHP), which leads to choking and/or shock waves. This limit could be reached when liquid metals are used as the working fluid in GHPs (such as potassium GHPs operating at 725 to 925 K) and subjected to very high input heat fluxes [Prenger et al. (1986); Jafari et al. (2016)]. In practice, however, this limit has never been reported in the published literature [Dunn and Reay (2012); Jafari et al. (2016)].

Another limit, referred to as an oscillation limit, in which the input heat flux is increased above the flooding limit and the GHP starts to operate intermittently, has been discussed by Dobran (1985). It should also be noted that the GBP is also considered as an operational limit by some authors, as it results in unsteady and chaotic operation of the GHP; and its explosive nature could also damage the GHP [Jafari (2016)].

1.2.6 Concluding remarks

In summary, based on the review of the published literature, it was concluded that the GBP in GHPs adversely affects their heat transfer performance; and it could also shorten the service life of the GHPs. Thus, it is desirable to mitigate or eliminate the GBP in GHPs, and many studies have been carried out to find ways to do this. However, there is a need for additional studies on this topic. The work presented in this thesis is an effort towards the fulfilment of this need.

1.3 Objectives

The specific objectives of this work were selected in the context of the overall goal presented in Section 1.1 and after the completion of the literature review presented in Section 1.2. They are summarized in pointwise form below:

1) Refurbish a gravity heat pipe (GHP) and the experimental facilities designed and setup earlier by Boopathy (2017) and improve them, if needed

2) Get familiar with the operation of the GHP and the experimental facilities mentioned above, by running some preliminary experiments and checking the results against those obtained by Boopathy (2017)
3) Establish the reliability of the GHP and the experimental facilities, by undertaking repeatability tests of the preliminary experiments and implementing additional improvements, if needed
4) Conduct benchmarking runs to establish baseline results pertaining to the geyser boiling phenomena (GBP) in the GHP (runs without any techniques for mitigating the GBP)
5) Propose and implement techniques for mitigating the GBP in the GHP
6) Conduct experiments to assess the proposed techniques for mitigating the GBP in the GHP, and provide recommendations for extensions of this work

1.4 Organization of the Thesis

In the earlier sections of this chapter (Chapter 1), the following topics were presented and discussed: the background, motivation, and overall goal of this work; a literature review; and the specific objectives of this work. In Chapter 2, some of the theoretical considerations that were used for developing a basic understanding of the various thermofluid processes that occur within GHPs are discussed. Descriptions of the GHP and the experimental facility that were refurbished and improved in this work, the proposed techniques for mitigating the GBP, and the procedures that were used to run the experiments are presented and discussed in Chapter 3. In Chapter 4, the experimental results, and assessments of the proposed techniques for mitigating the GBP in the GHP are presented and discussed. A review of the thesis, a summary of the main contributions of this work, and some recommendations for extensions of this work are presented in Chapter 5.

Chapter 2: Theoretical Considerations

The thermofluid phenomena that occur in gravity heat pipes (GHPs) include the following [Imura et al. (1983); Reed and Tien (1987); Niro and Beretta (1990); Guo and Nutter (2009); Faghri (2012, 2014); Reay et al. (2013); Jafari et al. (2016); Guichet et al. (2019)]: boiling and the related vapor-bubble dynamics (in the evaporator section); condensation (in the condenser section); condensate and vapor flows (in the adiabatic section); and heat conduction (in the wall of the containing tube). Some of the theoretical considerations that were used for developing a basic understanding of these thermofluid phenomena are discussed briefly in this chapter. These discussions are presented in six sections that address the following topics: 1) the boiling curve of Nukiyama (1966); 2) the correlation of Rohsenow (1951, 1973) for nucleate pool boiling and some extensions of it; 3) the laminar film condensation theory of Nusselt (1916) and some extensions of it; 4) notes on bubble dynamics; 5) some dimensionless parameters that govern GHPs; and 6) concluding remarks.

2.1 Boiling Curve of Nukiyama

For developing an understanding of the physical mechanisms of pool boiling (akin to that which occurs in GHPs) and its various modes, it is useful to examine the boiling curve of Nukiyama (1966). In his original work (which was performed in 1934), Nukiyama (1966) conducted an experimental investigation of pool boiling in which he passed electrical current through single nichrome and platinum wires immersed in water at atmospheric pressure. In each case, the heat flux from the heated-wire surface to the surrounding water, $q_s^{''}$, was controlled by adjusting the electrical voltage applied across it (and hence the current passing through it). The term 'power-controlled heating' is used to describe the wire-heating arrangement used by Nukiyama (1966) in his experimental investigation. For each value of the power input, the temperature of the wire was determined from a measurement of its electrical resistance (and a correlation that related electrical resistance of the wire to its temperature). In each case, the values of $q_s^{''}$ and the excess temperature, $\Delta T_e = (T_s - T_{sat})$, where the wire-temperature is T_s and T_{sat} is the saturation temperature of the surrounding water, were determined. Nukiyama (1966) presented these experimental results in a plot of $q_s^{''}$ *vs.* ΔT_e. This plot is now called the 'boiling curve of Nukiyama' [Rohsenow (1973); Carey (1992); Hewitt (1998); Incropera and DeWitt (2002)]. This boiling curve of Nukiyama is presented in Figure 2.1.

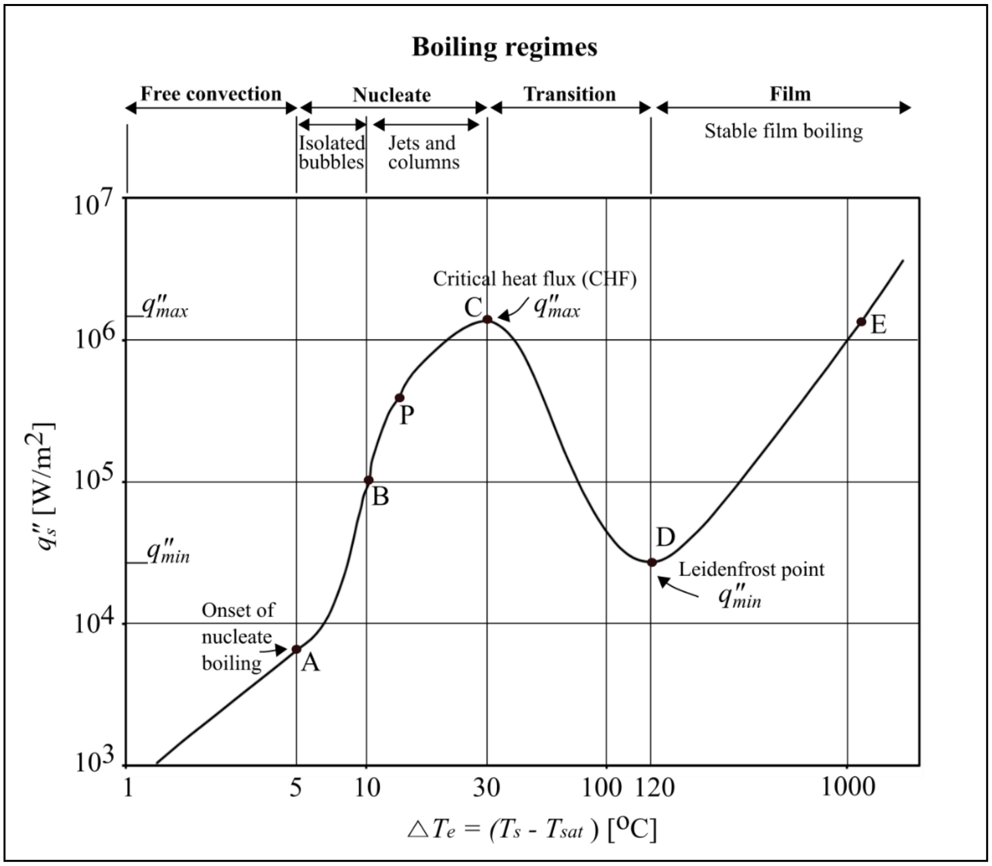

Figure 2.1 The boiling curve of Nukiyama (1966) for water at atmospheric pressure [adapted from a similar curve presented in Incropera and DeWitt (2002)].

The boiling curve of Nukiyama (1966) shown in Figure 2.1 pertains to water at atmospheric pressure. However, similar behavior characterizes the pool boiling of other fluids [Rohsenow (1973); Hewitt (1998)]. The initial portion of the boiling curve of Nukiyama (1966) shows that when the applied power input is increased, $q_s^{"}$ increases with ΔT_e, slowly at first and then very rapidly. In his experiments, Nukiyama observed that boiling (indicated by the presence of vapor bubbles) did not begin until $\Delta T_e \approx 5\ °C$. With further increases in input power, $q_s^{"}$ increased to very high levels until, at a value slightly larger than $q_{max}^{"}$, the wire temperature jumped to a value that caused the nichrome wire to melt ("burnout"). Nukiyama then continued his experiments with a wire made of platinum, which has a melting point of roughly 2045 K compared to about 1500 K for nichrome [Incropera and DeWitt (2002)]. This switch to a platinum wire allowed him to obtained data that are represented by the full curve illustrated in Figure 2.1.

As indicated by the plot in Figure 2.1, for increasing $q_s^{"}$ in the region $\Delta T_e \leq \Delta T_{e,A}$ (with $\Delta T_{e,A} \sim 5°C$), the heat transfer from the wire surface is purely by single-phase natural convection. In this region, superheated liquid rises to the surface of the water pool and evaporation takes place at this surface. As $q_s^{"}$ is increased beyond the value at 'A', bubbles begin to form on the surface of the wire, and then depart from its surface and rise through the liquid in a process that is referred to as nucleate boiling. Nucleate boiling in two different regimes exists in the range $\Delta T_{e,A} \leq \Delta T_e \leq \Delta T_{e,C}$, where $\Delta T_{e,C} \sim 30\ °C$. In the region 'A' to 'B', isolated bubbles form at nucleation sites on the surface of the wire, then separate from it and create considerable fluid mixing adjacent to it, substantially increasing $q_s^{"}$ and the boiling heat transfer coefficient, $h \triangleq q_s^{"} / \Delta T_e$. Most of the heat exchange in this regime is through direct transfer from the wire surface to the liquid in motion over it, and not through the vapor bubbles rising through the water pool. As ΔT_e is increased beyond $\Delta T_{e,B}$, more nucleation sites are created on the surface of the wire, and the increased rate of formation of the bubbles causes them to interfere and coalesce. In the region 'B' to 'C', the coalescing vapor bubbles rise through the water pool as jets or columns, which subsequently merge into slugs of the vapor. In this region, the heat transfer coefficient decreases but $q_s^{"} = h\,\Delta T_e$ continues to increase.

The maximum heat flux on the surface of the wire, $q_{max}^{"}$, is usually referred to as the 'critical' heat flux. It exceeds 1 MW/m^2 for water at atmospheric pressure. At the point 'C', where the maximum heat flux occurs, the rate of vapor formation is so significant that it is difficult for the liquid water to continuously wet the wire surface; and the rate of decrease of h matches the rate of increase of ΔT_e, so the *rate of change* of $q_s^{"} = h\,\Delta T_e$ goes to zero. The region between point 'C' to point 'D', is termed transition boiling (or unstable film boiling; or partial film boiling). In this region, the rate of bubble formation is so rapid that a vapor film or blanket begins to form on the wire surface, and the conditions oscillate between film and nucleate boiling; however, the fraction of the total wire surface covered by the vapor film increases with increasing ΔT_e beyond the point 'C', so h and $q_s^{"} = h\,\Delta T_e$ decrease, as the thermal conductivity of the vapor is much less than that of the liquid. Beyond point 'D', vapor film boiling exists.

The point 'D' of the Nukiyama boiling curve is referred to as the Leidenfrost point [Rohesnow (1973); Hewitt (1998)]. At this point, the heat flux reaches a local minimum, q''_{min}, and the surface of the wire is completely covered by a vapor blanket. Beyond point 'D', the heat transfer from the wire surface to the liquid water occurs by conduction and radiation through the intermediate vapor film.

The power-controlled arrangement used by Nukiyama (1966) is similar to that which occurs in many electrical resistance heating devices and also in nuclear reactors. Thus, in these devices and in Nukiyama's experiment, as q''_s is increased beyond q''_{max}, the conditions jump suddenly from the nucleate regime to the vapor-film boiling regime, causing an effectively stepwise and significant increase in ΔT_e and T_s; and this increase in T_s often exceeds the melting temperature of the solid and causes destruction or failure of the heating or power system. It is for this reason that the point 'C' is often referred to as the burnout or boiling-crisis point.

It is desirable to operate GHPs in the nucleate boiling regime, because of the high values of the surface heat flux and the heat transfer coefficient (q''_s and $h \triangleq q''_s / \Delta T_e$, respectively) and the stable (steady) operating conditions that characterize this regime. As was mentioned in Chapter 1, in gravity heat pipes (GHPs) operating at low power inputs (inadequate for sustaining nucleate boiling in the liquid pool inside the evaporator), geyser boiling phenomena (GBP) could occur [Jafari et al. (2016); Pabon et al. (2019)]. The GBP could lead to repeated impact loads on the cap of the condenser section, large cyclical variations in the wall temperatures (hence, cyclical thermal stresses and the associated risks of fatigue-induced brittleness and cracks), and vibrations of the GHP. The overall goal of the work presented in this thesis was to propose and assess techniques to mitigate GBP in a GHP. Details of these proposed techniques and related topics are presented and discussed in Chapter 3. The results are presented and discussed in Chapter 4.

2.2 Correlation of Rohsenow for Nucleate Pool Boiling and Some Extensions

The first correlation for nucleate pool boiling was proposed by Roshenow (1951) and it is still widely used. This correlation is usually expressed as follows [Rohsenow(1951); Hewitt (1998)]:

$$q''_s = \mu_l h_{fg} \left[\frac{g(\rho_l - \rho_v)}{\sigma} \right]^{1/2} \left(\frac{c_{p,l} \Delta T_e}{C_{s,f} h_{fg} \, \mathrm{Pr}_l^n} \right)^3 \tag{2.1}$$

In Equation (2.1), all properties pertain to the saturated liquid, except ρ_v which is the density of the saturated vapor [kg/m^3]; $q_s^{"}$ is the heat flux at the surface [W/m^2]; the latent heat of evaporation is indicated by h_{fg} [J/kg]; μ_l is the dynamic viscosity of the liquid [kg/m.s]; g is the acceleration due to gravity [m/s^2]; ρ_l is the density of the liquid [kg/m^3]; σ is the surface tension at the liquid-vapor interface [N/m]; $c_{p,l}$ is the liquid specific heat at constant pressure [J/kg.K]; $C_{s,f}$ is the boiling coefficient for surface-liquid combination; and Pr_l is the Prandtl number of the liquid. The surface tension has a significant effect on the vapor bubble formation and development on the heated surface; its departure diameter, or diameter when it leaves the heated surface; the pressure inside it; and its rate of growth as it rises through the liquid pool. The solid–fluid combination influences the value of the coefficient, $C_{s,f}$, and the exponent of the Prandtl number, *n*. Representative experimentally determined values of $C_{s,f}$ and *n* are available in the published literature [Rohsenow (1973); Hewitt (1998)].

The Rohsenow (1951) correlation was obtained using experimental data for boiling at atmospheric pressures and it applies only for clean surfaces. When it is used to estimate the heat flux, $q_s^{"}$, the errors can be as high as ± 100 %. However, since ΔT_e is proportional to $(q_s^{"})^{1/3}$, this error is reduced considerably when the correlation is used to estimate the excess temperature from a knowledge of the surface heat flux [Rohsenow (1973); Hewitt (1998)].

Many different correlations have been proposed for modelling nucleate pool boiling, some formulated specifically for two-phase closed thermosyphons (with geometry akin to that of the GHP investigated in this work). They have been summarized and discussed in the work of Guichet et al. (2019). A correlation that is highly recommended for GHPs is that proposed by Imura et al. (1979). It can be expressed in the following form [Noie (2005); Jouhara and Robinson (2010); and Lataoui and Jemni (2017)]:

$$h = 0.32Z\left[\frac{P_{sat}}{P_{atm}}\right]^{0.3}\left(q^{"}_{s}\right)^{0.4} \text{ where } Z = \left[\frac{\rho_l^{0.65} k_l^{0.3} c_{p,l}^{\ 0.7} g^{0.2}}{\rho_v^{0.25} h_{fg}^{\ 0.4} \mu_l^{0.1}}\right] \tag{2.2}$$

In equation (2.2) h is the heat transfer coefficient [W/m^2.K]; P_{sat} , P_{atm} are the saturation and atmospheric pressure, respectively [Pa]; k_l is the thermal conductivity of the liquid [W/m.K]. All other notations used in Equation (2.2) are the same as those described for Equation (2.1). The accuracy of this correlation has been discussed in the works of Park et al. (2002), Noie (2005), and Guo and Nutter (2009). This correlation is not recommended for GHPs with 'small' inner diameter, for which a correlation proposed by Stephan and Abdelsalam (1980) is recommended. Their correlation was developed by applying a regression analysis to over 5000 experimental data points, and it can be used for several working fluids including water. It is widely used and highly recommended by Táboas et al. (2007). The correlation of Stephan and Abdelsalam (1980) cast in a form that is specialized for water (as the working fluid) is given below:

$$h = \left(0.246 \frac{k_l}{D_d} \times 10^7 \right) X_1^{0.673} X_2^{-1.58} X_3^{1.26} X_4^{5.22}$$

where (2.3)

$$X_1 = \frac{q_s'' D_d}{k_l T_{sat,abs}};\ X_2 = \frac{h_{fg} D_d^2}{\alpha_l^2};\ X_3 = \frac{c_{p,l} T_{sat,abs} D_d^2}{\alpha_l^2};\ \text{and}\ X_4 = \frac{(\rho_l - \rho_v)}{\rho_l}$$

In Equation (2.3) D_d is the bubble departure diameter [m]; α_l is the thermal diffusivity of the liquid [m^2/s]; $T_{sat,abs}$ is the saturation temperature [K]. All other notations used in Equation (2.3) are the same as those described for Equation (2.1) and (2.2). The bubble departure diameter, D_d , in Equation (2.3) is calculated using an equation proposed by Fritz (1935) which is presented in Section 2.4. A correlation developed by Casarosa et al. (1983) and recommended by Lin et al. (1995) for the heat transfer coefficient in the geyser boiling regime for an *annular* two-phase closed thermosyphon is the following:

$$h = 2.925 P_v^{0.18} q_s''^{2/3} \qquad (2.4)$$

Where P_v is the absolute vapor pressure [bar], and all other notations are the same as those described earlier for Equations (2.1), (2.2), and (2.3)

In conclusion, the following comments are worth noting: 1) correlations for q''_{max} , q''_{min} , and h in the vapor film boiling regime are available in the work of Hewitt (1998); 2) despite the numerous publications on correlations for boiling heat transfer [Guichet et al. (2019)], there is considerable scatter in the predictions obtained with the available correlations, which is not surprising considering the large number of parameters that influence boiling heat transfer, including the preparation and condition of the heated surface [Mikic and Rohsenow (1969)]; 3) most of the available correlations apply to boiling on horizontal and flat heated surfaces, and only very few apply to vertical curved surfaces; 4) most of the available correlations apply to atmospheric or higher values of pressure, though there are few that apply to boiling under sub-atmospheric pressures [Gao et al. (2019)]; and 5) very few (if any) of the available correlations have been *specifically* developed for surfaces with roughness (defined or otherwise).

2.3 Laminar Film Condensation Theory of Nusselt and Some Extensions

A theoretical analysis of *laminar* film condensation of a vapor on a smooth, vertical, *flat*, and isothermal surface, with the liquid condensate flowing down this surface under the action of gravity, was first proposed by Nusselt (1916). Nevertheless, it provides useful *physical insights* into condensation on the inside surface of tubes (and other *curved* surfaces) and also turbulent film condensation. The assumptions invoked in the laminar film condensation theory of Nusselt (1916) are summarized in the following list: 1) the vapor is at the saturation condition and it is stationary (far from the cooled surface); 2) constant thermophysical properties of the condensate (at the arithmetic mean of the temperatures of the saturated vapor and the cooled isothermal surface) and vapor (at its saturation temperature); 3) viscous shear stress at the interface between the vapor and the condensate flowing down the vertical surface is zero (negligibly small); 4) the rates of viscous and conduction transport in the vertically downward direction inside the condensate layer are negligible compared to those in the direction normal to it; 5) the rates of advection transport of momentum and enthalpy in the vertically downward direction inside the condensate layer is negligible compared to the conduction transport across it; and 6) the variation of static pressure across the vertically downward flow of the condensate layer is negligible.

Nusselt (1916) solved his mathematical model analytically. His solution provides expressions for the velocity and temperature distributions; the variations with distance of the thickness of the condensate layer and the mass flow rate in it; and the local and average values of the rate of heat transfer. Full details of this solution are available in the works of Rohsenow (1985), Marto (1998), and Incropera and DeWitt (2002). The local (at a distance *x* downwards from the upper edge of the vertical flat plate) and average heat transfer coefficients, h_x and h_{av}, respectively, are given by the following equations [Incropera and DeWitt (2002)]:

$$h_x = \left[\frac{g\rho_l(\rho_l - \rho_v)h_{fg}k_l^3}{4\mu_l(T_{sat} - T_s)x} \right]^{1/4} \tag{2.5}$$

$$h_{av} = 0.943\left[\frac{g\rho_l(\rho_l - \rho_v)h_{fg}k_l^3}{4\mu_l(T_{sat} - T_s)L} \right]^{1/4} \tag{2.6}$$

In Equation (2.6), L is the total length of the plate; and the other notations are similar to those described for Equations (2.1) and (2.2).

Equation (2.6) underpredicts most experimental results for laminar film condensation by around 20%. It is therefore customary to use the following adjusted version of this equation [Marto (1998)]:

$$h_{av} = 1.13\left[\frac{g\rho_l(\rho_l - \rho_v)h_{fg}k_l^3}{4\mu_l(T_{sat} - T_s)L} \right]^{1/4} \tag{2.7}$$

In another improvement, Rohsenow (1985) showed that thermal advection effects can be incorporated in the theory of Nusselt (1916) by using a modified latent heat of vaporization, $h_{fg}^{'}$, in place of h_{fg} in Equations (2.5) to (2.7):

$$h_{fg}^{'} = h_{fg} + 0.68c_{p,l}(T_{sat} - T_s) \tag{2.8}$$

Empirical correlations for turbulent film condensation are available in the works of Marto (1998) and Incropera and DeWitt (2002). Models and correlations for condensation in horizontal, vertical, and inclined tubes, and related discussions, are also available in the published literature, for example, in the works of Seban and Hodgson (1982), Seban and Faghri (1984), Rohsenow (1985), Dobson and Chato (1998), Marto (1998), Thumm et al. (2001), and El Hajal et al. (2003). However, despite the tremendous interest and numerous works on wicked heat pipes [Faghri (1995, 2012, 2014); Dunn and Reay (2012); Reay et al. (2013)], there are very few works (if any) on condensation heat transfer and related correlations developed *specifically* for surfaces with roughness (defined or otherwise).

2.4 Notes on Bubble Dynamics

The work of Guichet et al. (2019) provides an extensive review of many published works that discuss the underlying physics of nucleate boiling and provide correlations for the corresponding heat transfer coefficients, the rate of growth of bubbles that form on the surfaces of heated walls, and the departure diameter, D_d, of these bubbles (diameter of an effectively spherical bubble when it leaves the surface of the heated wall). Several of these papers were discussed in the literature review presented in Chapter 1. A few of the main equations and related matters taken from some pertinent works are provided and discussed in this section.

A correlation proposed by Fritz (1935) continues to be regarded as one of the most reliable for predictions of the bubble departure diameter in nucleate pool boiling of pure liquids and is heavily used. His model is based on a balance of the gravitational buoyancy (lift) force on the vapor bubble, created by the difference between density of the liquid and the considerably lower density of the vapor immersed in it, and the surface tension force that keeps it attached to the surface on which it originated. This balance of forces can be characterized by a Bond number based on the bubble departure diameter and defined as follows [Guichet et al. (2019)]:

$$Bo_{D_d} = g\,(\rho_l - \rho_v)\,D_d^2 / \sigma \tag{2.9}$$

In the model proposed by Fritz (1935), the drag and agitation forces on the vapor bubble and the inertia effects caused by the addition of mass into bubble (by the evaporation at its interface with the surrounding liquid) are neglected. Using this model, Fritz (1935) obtained a correlation for the bubble departure diameter at atmospheric pressure. It can be cast in the following form [Dhir et al. (2007); Guichet et al. (2019)]:

$$D_d = 0.0208 \times \theta_B \times \left[\frac{\sigma}{g(\rho_l - \rho_v)} \right]^{1/2} \tag{2.10}$$

In this equation, θ_B is the contact angle in degrees; and as reported by Guichet et al. (2019), Fritz (1935) used a value of $\theta_B = 45^{\circ}$ for water. Notwithstanding the comments given above, significant differences have been noted between the predictions obtained with the correlation of Fritz (1935) and corresponding experimental observations, especially at high pressures [Dhir et al. (2007)].

Many modifications of the correlation of Fritz (1935) have been proposed in efforts to overcome some of its shortcoming, and they have been reviewed by Guichet et al. (2019).

The published works on the departure diameter of vapor bubbles show that it is proportional to an intrinsic length in nucleate pool boiling, which is sometimes referred to as the capillary length, λ_c, as is done in the work of Elkholy and Kempers (2020):

$$D_d \sim \lambda_c = \{[\sigma / (\rho_l - \rho_v)\, g\,]\}^{1/2} \tag{2.11}$$

In GHPs and loop thermosyphons, the length scale defined by Equation (2.11) can be normalized by the inner diameter of the containing tube to obtain a 'confinement number', as described in the works of Smith et al. (2018a, 2018b) and Elkholy and Kempers (2020):

$$Co = \lambda_c / D_i \tag{2.12}$$

The rate of bubble growth is often used in models to predict their departure diameter [Guichet et al. (2019)]. The seminal contributions on bubble growth include the works of Rayleigh (1917), Plesset and Zwick (1954), and Mikic et al. (1970); and some of the later contributions include the works of Zeng et al. (1993) and Dhir et al. (2007), for example. There are many published works in this area; an extensive review is available in the work of Guichet et al. (2019).

In summary, it is worth noting again that there is considerable scatter (uncertainties) in the predictions obtained using the available correlations mentioned above in this section. Furthermore, and most of them pertain to nucleate pool boiling on surfaces of *horizontal* heated walls or the outer surfaces of *horizontal* heated cylinders in *large* enclosures, with a very small bubble confinement number = {(bubble departure-diameter) / (horizontal dimension of enclosure)} << 1, which is a modified view of the 'confinement number' based on the works of Smith et al. (2018a, 2018b) and defined in Equation (2.12). Furthermore, none of the available correlations are designed to apply to either the *vertical or inclined curved* inner surface of the evaporator section of GHPs or to surfaces (horizontal or vertical; curved or flat) with roughness (defined or otherwise). Thus, in this work, a rudimentary approach based on assumptions similar to those used by Fritz (1935) was employed to estimate the bubble departure diameter expected with the techniques that were proposed for mitigating geyser boiling in a GHP originally designed, implemented, and investigated by Boopathy (2017). Full details of this rudimentary approach and the proposed techniques for mitigating geyser boiling are presented and discussed in Chapter 3.

2.5 Some Dimensionless Parameters that Govern GHPs

The discussions presented in the earlier sections of this chapter and the literature review presented in Chapter 1 show that the boiling, condensation, and related thermofluid phenomena that occur inside GHPs can be quite complex. Thus, there are no generally applicable fundamental mathematical models of these phenomena (that is, well defined governing equations, boundary conditions, and initial conditions that are free of empirical inputs) in the published literature. In the absence of such models, the governing dimensionless geometrical and thermofluid parameters can be identified using the Buckingham pi theorem [Fox and McDonald (1985); Tritton (1988); White (2015)], as was done by Boopathy (2017) and in this work too. The dimensionless parameters and their values pertaining to the GHP used in this work are presented in the remainder of this section, with reference to the notation given below in Figure 2.2.

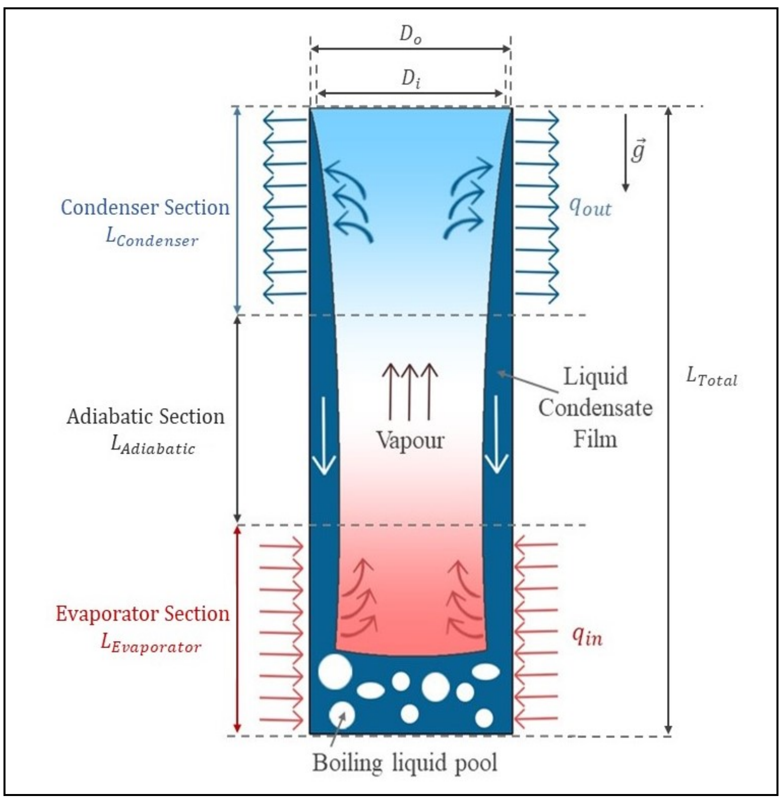

Figure 2.2 Schematic illustration of the GHP in the vertical orientation ($\theta = 0^o$) and some of the notation used in this work.

The ranges of expected values of the dimensionless thermofluid parameters were estimated by assuming that suitably averaged thermophysical properties of the liquid and vapor phases of water (the working fluid used in this work) remain effectively constant. These thermophysical properties were obtained from the published literature [Moran and Shapiro (1998); Incropera and DeWitt (2002); Lemmon et al. (2013)] for the expected ranges of the temperature and pressure in the evaporator and condenser sections of the GHP, initially based on the work of Boopathy (2017). Their final values were calculated using the actual ranges of the temperature and pressure encountered in the experiments conducted in this work (the details are given in Chapters 3 and 4).

2.5.1 Geometrical parameters

The dimensionless geometric parameters pertaining to the GHP that is schematically illustrated in Figure 2.2 are the following:

$L_{Evapoartor} / L_{Total}$; $L_{Condenser} / L_{Total}$

Aspect ratio, $L_{Evaporator} / D_i$; $(D_o - D_i) / D_i$ (2.13)

Angle of tilt of the GHP from the vertical: θ

2.5.2 Some thermofluid parameters

Some of the dimensionless thermofluid parameters that govern the operation of the GHP shown in Figure 2.2 are given in this subsection.

The ratios of the values of thermal conductivity, specific heat at constant pressure, and density of the solid wall (of the core tubes of the evaporator, adiabatic, and condenser sections of the GHP) to those of the liquid phase of the working fluid:

$$(k_s / k_l)_{Evap;\,Cond} \;;\; (c_{p,s} / c_{p,l})_{Evap;\,Cond} \;;\text{ and } (\rho_s / \rho_l)_{Evap;\,Cond} \quad (2.14)$$

The fill ratio, *FR*, for the GHP. It is the ratio of the volume of the liquid pool to the total volume between solid components within the evaporator section of the GHP, up to the top of its active-heating portion:

$$FR = (Vol)_{liquid\ pool} / (Vol)_{between\ solid\ components\ in\ Evap} \quad (2.15)$$

Galileo number, Ga, or modified Grashof number, Gr_M, in the evaporator and the condenser (this number represents the ratio of buoyancy force, due to the difference in the densities of the liquid and vapor phases of the working fluid, to the viscous force):

$$\{Ga\}_{Evap;\,Cond} = \{Gr_M\}_{Evap;\,Cond} = \{\rho_l g(\rho_l - \rho_v) D_i^3 / \mu_l^2\}_{Evap;\,Cond} \quad (2.16)$$

Jakob number, Ja, in the evaporator and the condenser (it represents the ratio of the maximum sensible heat, absorbed by the liquid during condensation and boiling, to the latent heat of vaporization):

$$\left\{Ja\right\}_{Evap;\,Cond} = \left\{\frac{c_{p,l}(T_{wall} - T_{sat})}{h_{fg}}\right\}_{Evap;\,Cond}^{Abs} \tag{2.17}$$

Prandtl number, $\Pr$, in the evaporator and the condenser (it represents the ratio of the rate of diffusion of momentum by viscous action to the rate of diffusion of thermal energy by conduction):

$$\left\{\Pr\right\}_{Evap;\,Cond} = \left\{\mu_l c_{p,l} / k_l\right\}_{Evap;Cond} \tag{2.18}$$

Bond number, Bo, in the evaporator based on the inside diameter of its core tube (it represents the ratio of the buoyancy force to the surface tension force):

$$\left\{Bo\right\}_{Evap} = \{g(\rho_l - \rho_v)D_i^2 / \sigma\}_{Evap} \tag{2.19}$$

The Reynolds number of the condensate film, Re_{film}, in the condenser. It represents the ratio of the inertia force to viscous force in the condensate film; it is based on the mass flow rate of the condensate per unit perimeter of the inside surface of the core tube of the condenser; and it is used to characterize transitions from smooth-laminar to laminar-wavy to turbulent flow regimes [Incropera and DeWitt (2002)]. It is defined as follows:

$$\mathrm{Re}_{film} = 4\Gamma / \mu_l \text{ ; with } \Gamma = (q_{input} / h_{fg}) / (\pi D_i) \tag{2.20}$$

2.5.3 Values of the dimensionless geometrical and thermofluid parameters

The details of the GHP that was refurbished and used in this work are given in Chapter 3. The inputs and results for each of the experimental runs are given in Chapter 4. The properties of water (working fluid) and stainless steel (SS 316; tube-wall material) were obtained from the published literature [Moran and Shapiro (1998); Incropera and DeWitt (2002); Lemmon et al. (2013)]. For this GHP and the experimental runs undertaken with it, the dimensionless parameters described in Subsections 2.5.1 and 2.5.2 had the following values or lay in the following ranges:

$$L_{Evapoartor} / L_{Total} = 0.347 \ ; \ L_{Condenser} / L_{Total} = 0.365$$
$$\text{Aspect ratio, } L_{Evaporator} / D_i = 10.294 \ ; \ (D_o - D_i) / D_i = 0.0695 \tag{2.21}$$
$$\text{Angle of tilt of the GHP from the vertical: } \theta = 0^{\mathrm{o}}$$

$$(k_s / k_l)_{Evap;\,Cond} = (20.83 \text{ to } 21.50) \ ; \ (21.23 \text{ to } 22.06)$$
$$(c_{p,s} / c_{p,l})_{Evap;\,Cond} = 0.112 \ ; \ 0.112 \tag{2.22}$$
$$(\rho_s / \rho_l)_{Evap;\,Cond} = (8.285 \text{ to } 8.339) \ ; \ (8.256 \text{ to } 8.305)$$

$$FR = 100\ \%,\ 150\ \%,\ 175\ \% \tag{2.23}$$

$$\begin{aligned} \{Ga\}_{Evap;\,Cond} &= \{Gr_M\}_{Evap;\,Cond} = (2.37 \text{ to } 4.30)\times 10^8 \ ; \ (1.48 \text{ to } 2.97)\times 10^8 \\ \{Ja\}_{Evap;\,Cond} &= (0.00815 \text{ to } 0.0184) \ ; \ (0.00234 \text{ to } 0.0240) \\ \{\Pr\}_{Evap;\,Cond} &= (3.55 \text{ to } 4.97) \ ; \ (4.37 \text{ to } 6.47) \\ \{Bo\}_{Evap} &= (77.96 \text{ to } 80.62) \ ; \ \mathrm{Re}_{film} = (1.152 \text{ to } 8.367) \end{aligned} \tag{2.24}$$

2.6 Concluding Remarks

In conclusion, it is noted again that the theoretical considerations presented in the earlier sections of this chapter were used to develop a basic understanding of the various thermofluid phenomena that occur within GHPs. They build on related discussions presented in Chapter 1.

There are numerous papers on GHPs in the published literature which were used in this work to develop a basic understanding of the physical mechanisms and the modes of operation of GHPs. However, with respect to designs of GHPs for particular applications, only qualitative guidance can be obtained, at best, from the aforementioned papers and theoretical considerations, due to the relatively large number of governing geometric and thermofluid parameters, several different choices of working fluids, several different boiling regimes and condensation phenomena, and unsteady and steady-state operating conditions.

It should also be noted again that none of the available correlations in the published literature on boiling, condensation, and bubble departure diameter and its rate of growth are directly applicable to either the *vertical* or *inclined curved* inner surface of the evaporator section of GHPs or to surfaces (horizontal or vertical; curved or flat) with roughness (defined or otherwise). Similarly, it is difficult to use the information in the published literature to make specific or general conclusions about the ways to mitigate the geyser boiling phenomena (GBP) in GHPs suitable for use in HVAC and geothermally assisted heating or cooling applications.

It is in the context of the observations given above that the objectives of this work were chosen (repeated here for emphasis): 1) refurbish and improve a GHP and experimental facilities setup by Boopathy (2017); 2) get familiar with its operation; 3) get data on the GBP in the GHP by running benchmark cases; 4) propose and implement techniques for mitigating the GBP; and 5) runs experiments to assess these techniques. Descriptions of the experimental apparatus and procedures used in this work are provided in the next chapter (Chapter 3), along with the details of four different techniques that were proposed to mitigate the GBP in the GHP.

Chapter 3: Experimental Apparatus and Procedures

The gravity heat pipe (GHP), most of the other experimental apparatus, and some of the procedures used in this work were previously designed, set up, and employed by Boopathy (2017). In this work, the GHP and experimental setup were first fully refurbished and tested; and after that, some essential improvements to the experimental setup were implemented. In addition, four different techniques with potential for mitigating the geyser boiling phenomenon (GBP) that occurs in the GHP at relatively low power inputs were proposed, implemented, and assessed in this work.

Detailed descriptions of the GHP and much of the experimental setup used in this work are available in the work of Boopathy (2017). Nevertheless, the details of this GHP and the experimental setup are first presented concisely in this chapter (in Sections 3.1 and 3.2), to make this thesis self-contained and set the stage for the descriptions of the essential improvements that were undertaken in this work. Following that, the rationale for the choice of the working fluid and tube materials, the details of the vacuum circuit and gauges, and the details of the filling circuit are given in Sections 3.3, 3.4, and 3.5, respectively. The details of the four different techniques proposed in this work for mitigating the GBP in the GHP are presented and discussed in Section 3.6. Then, some of the supporting instrumentation and equipment are described in Section 3.7. Finally, the main experimental procedures used in this work are elaborated in Section 3.8.

In this chapter, the lengths of the various parts of the GHP are presented inches (inch) *and feet* (ft), *as these units were used to facilitate fabrication of these parts at machine shops in Montreal and Laval, Quebec, Canada. The following conversion factors could be used to obtain the corresponding lengths in SI units: 1* ft = *0.3048* m; *and 1* inch = *0.0254* m.

3.1 Details of the Gravity Heat Pipe

The top and side views, a section drawing, and an assembly drawing of the GHP used in this work are given in Figure 3.1. This GHP was made up of three main parts: 1) an evaporator section; 2) an adiabatic section (which also incorporated a flow visualization section); and 3) a condenser section. A photograph of some parts of this GHP are given in Figure 3.2. Concise descriptions of the main parts of the GHP are given in the following three subsections. In the subsection after that, some additional details of the assembled GHP are provided.

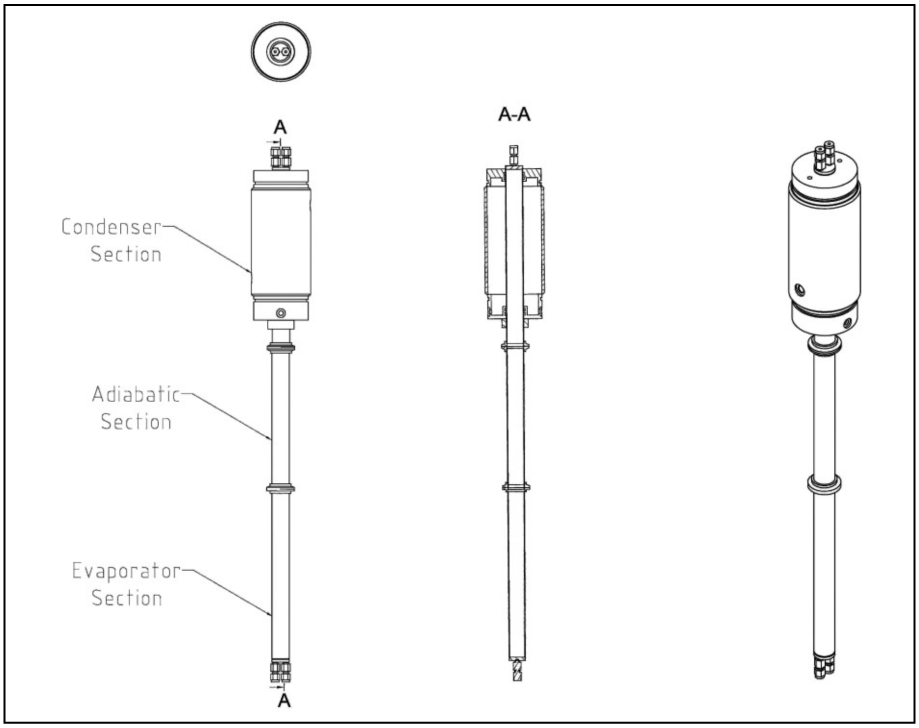

Figure 3.1 Schematic illustrations of the GHP.


Figure 3.2 Photograph of some parts of the GHP prior to assembly [taken from Boopathy (2017)]. The adiabatic section is the tube with a central portion of borosilicate glass (it was used for flow visualization). A spool of Teflon-covered nichrome heating wire, which was wrapped around the core tube of the evaporator section, is shown in the left-hand side of this photograph.

3.1.1 Evaporator section

A view of the assembled core of the evaporator section of the GHP is given in Figure 3.3. It was made of a straight stainless steel (SS 316) tube with 0.935-inch and 1-inch inside and outside diameters, respectively, and a total inner length of 9.625 inches. The upper end of this tube had a KF 25 vacuum flange welded to it. An endplate was welded to the other (bottom) side of this tube. This bottom endplate had two 1/8-inch *Swagelok* bore-through fittings welded to it: one of these was used to insert and hold a calibrated sheathed (SS 304) thermocouple, with its tip 1-inch inside the evaporator section (it was used to measure the liquid-pool temperature inside the evaporator section); and the other fitting was connected to the filling circuit (described in Section 3.5), which was used to fill the GHP with the working fluid (and also drain it), when required.

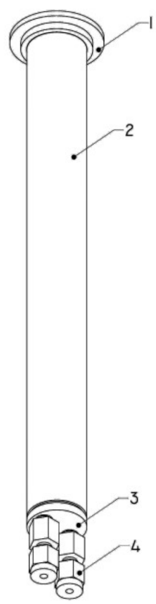

Assembled View of the Evaporator Section		
Item No.	Part & Description	Quantity
1	KF25 Flange (Welded at the upped end of tube)	1
2	Evaporator Tube	1
3	Endplate (Welded at the lower end)	1
4	1/8" Swagelock Fitting welded to Endplate	2

Figure 3.3 A view of the assembled core of the evaporator section of the GHP.

A total of 10 calibrated Type-E (chromel-constantan) thermocouples were attached to the outer surface of the core tube of the evaporator section. The beads of these thermocouples, each coated with a high-thermal-conductivity glue (*Omegabond 101*), were positioned in a helical pattern at regular intervals along the length of the tube (with a 1-inch interval between successive thermocouples). Details of the fabrication and calibration of these and other thermocouples used in this work are discussed later in this chapter (Subsection 3.7.1).

The evaporator section had a 7-inch active-heating length. A Teflon-coated nichrome heating wire (27 AWG wire; with 0.3 mm thickness of Teflon coating) was wound tightly and closely (contiguously, without overlapping) around the outer surface of the core stainless steel tube (in the active-heating portion) and on top of the coated thermocouple beads. Prior to the placing of the thermocouple beads and the winding of the Teflon-coated nichrome wire, a thin layer of high-thermal-conductivity paste (*Omegatherm 201*) was applied to the outer surface of the core stainless-steel tube. Details of a special jig and the procedure that were used for winding the heating wire on the core stainless-steel tube of the evaporator section are described in Boopathy (2017). The outer surface of the assembled evaporator section was wrapped with thin Teflon sheets, to contain any excess high-thermal-conductivity paste and to provide a clean outer surface that could be conveniently handled during the final assembly of the GHP. Electrical busbar terminals were attached to specially designed Teflon blocks that were used to attach the GHP to a support structure; and the extremities of the nichrome wire (stripped off the Teflon coating) were attached to these terminals. Insulated copper wires (of larger gauge than the nichrome heating wire) were used to connect these terminals to an electrical DC power supply. This arrangement provided an essentially uniform heat flux on the outer surface of the core tube over its active-heating segment. A photograph of the assembled evaporator section is given in Figure 3.4.

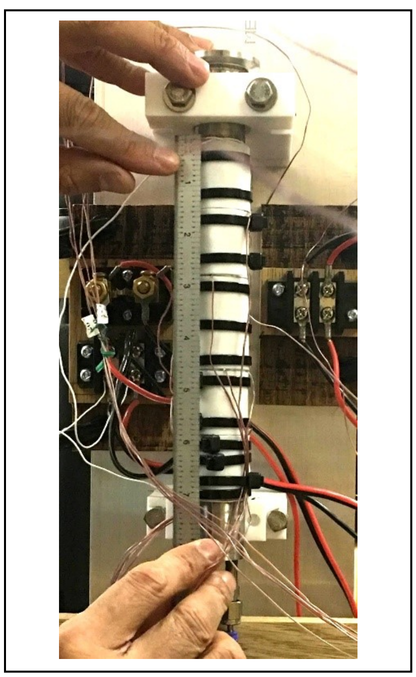

Figure 3.4 Photograph of the assembled evaporator section of the GHP.

The fully assembled evaporator section of the GHP was insulated with a layer of *Armaflex* pipe insulation (having a thermal conductivity of approximately 0.04 W/m°C). The outer diameter of this insulation was approximately equal to 2 inches.

3.1.2 Adiabatic section

The central adiabatic section of the GHP is shown in Figure 3.1 and in the photograph given in Figure 3.2. It was made of a composite tube with 0.935-inch and 1-inch inside and outside diameters, respectively, and a total length of 8 inches. The central portion of this adiabatic section was a 6.0-inch-long tube made of borosilicate glass (it was used for flow visualization during the operation of the GHP). The upper and bottom portions of the adiabatic section were made of 1-inch-long tubes, each welded to a KF 25 vacuum flange at one end, and all made of Kovar; the other end of the Kovar tubes were fused to the ends of the central borosilicate-glass tube. Kovar is an iron-nickel-cobalt alloy that has a coefficient of linear thermal expansion that is almost identical to that of borosilicate glass, which enables vacuum-tight fused joints between parts made of these materials. This adiabatic section (fully assembled) was purchased (prefabricated) from *Larson Electronic Glass* (Redwood City, California, U.S.A.).

3.1.3 Condenser section

A view of the assembled condenser section of the GHP is given in Figure 3.1 and its various parts are shown in the photograph given in Figure 3.2. It spanned a 10.125-inch-long segment of the top (upper) portion of the GHP. The core of this section was made of a straight stainless steel (SS 316) tube with 0.935-inch and 1-inch inside and outside diameters, respectively, and a 9-inch active-cooling length. The bottom end of this core inner tube had a KF 25 vacuum flange (made of SS 316) welded to it; and a stainless steel (SS 316) endplate was welded to its other (top) end. This top endplate had two 1/8-inch *Swagelok* bore-through fittings welded to it: one of these was used to insert and hold a 6-inch-long calibrated sheathed (SS 304) thermocouple, with its tip 4 inches inside the evaporator section (this thermocouple was used to measure the temperature of the saturated water vapor inside the condenser section during the operation of the GHP); and the other fitting was used to connect the GHP to a vacuum circuit (described in Section 3.4). A concentric annular cooling-water jacket was used on the outside surface of the core stainless steel tube over its active-cooling region. The outer tube of this concentric annular jacket was made of a

9-inch-long stainless-steel (SS 316 L) tube with a 3.4-inch outer diameter. Two 3/8-inch *Swagelok* compression fittings were welded into holes drilled on the curved surface of this outer tube. This annular cooling-water jacket was mounted on the GHP using suitable stainless steel (SS 316 L) endplates and four O-rings.

The condenser-section assembly and an exploded view of some of its various components are presented in Figures 3.5 and 3.6, respectively. Cooling water from a constant-temperature bath (*Neslab* RTE 211) was supplied (at a nominal temperature of 20 ºC) to the annular region of the jacket at its lower end and taken out at its upper end, using the two above-mentioned ports, each fitted with a 3/8-inch *Swagelok* compression fitting. Calibrated thermocouples, inserted via perpendicular legs of T-junctions, were to measure the inlet and outlet bulk temperatures of the cooling water. The volume and mass flow rates of the cooling water were maintained at approximately 63.6 ml/s and 0.0635 kg/s, respectively; and these rates were high enough to make the difference between the outlet and inlet bulk temperatures of the cooling water negligibly small (≤ 0.1 ºC) in all experimental runs undertaken in this work (details are provided in Chapter 4).

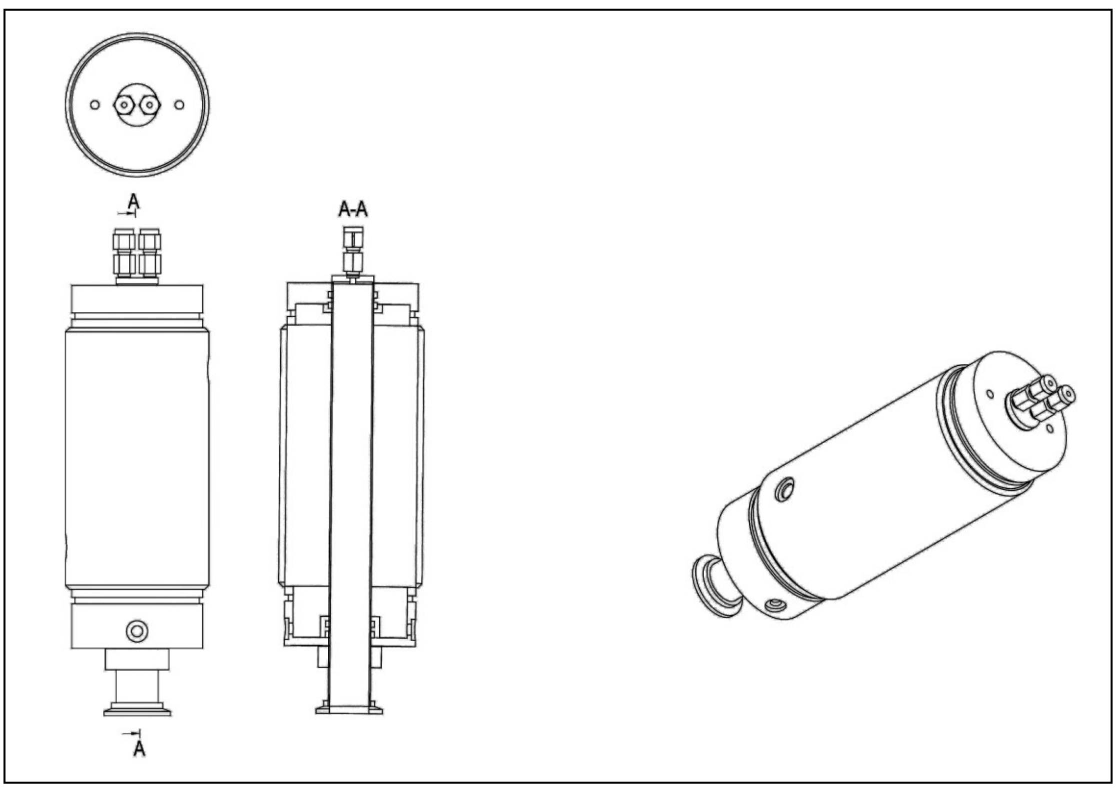

Figure 3.5 Schematic illustrations of the assembled condenser section of the GHP.

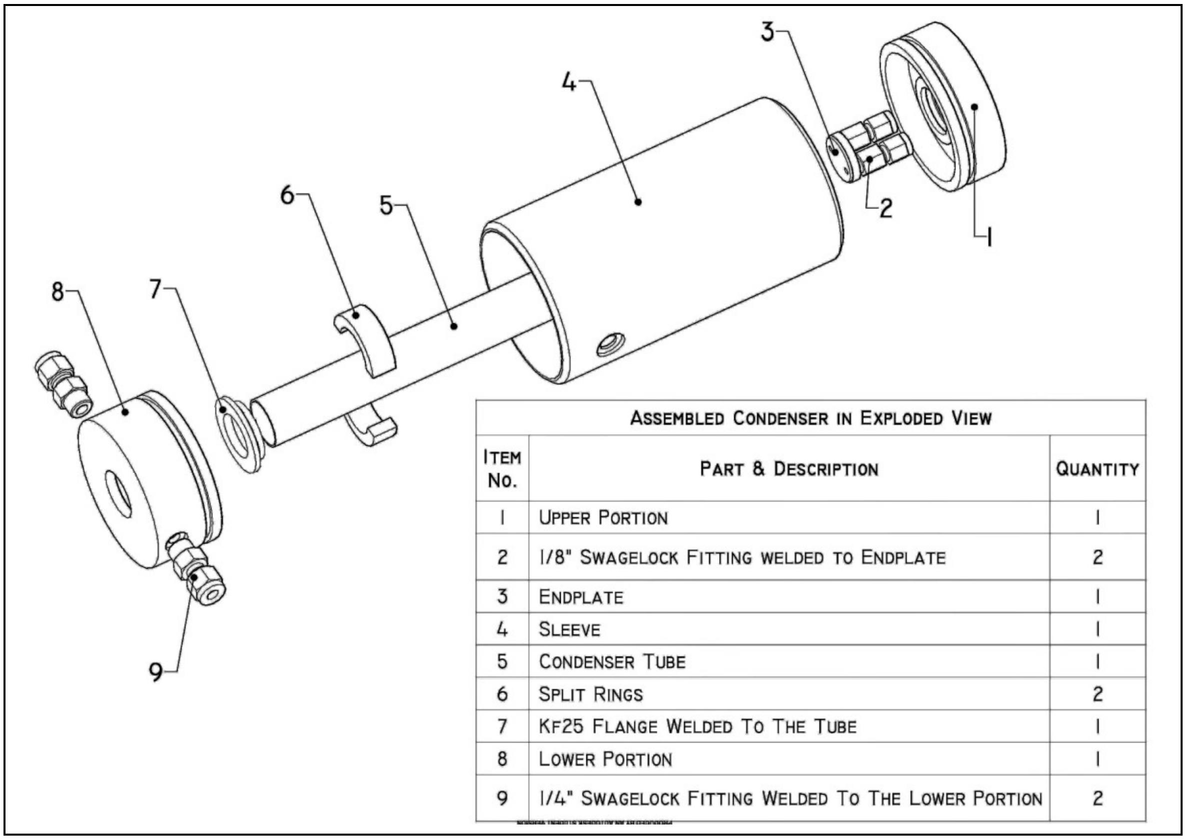

ASSEMBLED CONDENSER IN EXPLODED VIEW		
ITEM NO.	PART & DESCRIPTION	QUANTITY
1	UPPER PORTION	1
2	1/8" SWAGELOCK FITTING WELDED TO ENDPLATE	2
3	ENDPLATE	1
4	SLEEVE	1
5	CONDENSER TUBE	1
6	SPLIT RINGS	2
7	KF25 FLANGE WELDED TO THE TUBE	1
8	LOWER PORTION	1
9	1/4" SWAGELOCK FITTING WELDED TO THE LOWER PORTION	2

Figure 3.6 Exploded view of the condenser section of the GHP.

Two 1/4-inch *Swagelok* fittings inserted and welded to ports in the lower endplate of the annular cooling-water jacket of the condenser section were used for inserting 10 calibrated thermocouples. These thermocouples were attached to the outer wall of the stainless steel (SS 316) core tube of the condenser section, in a helical arrangement with 1-inch intervals between the lengthwise locations of adjacent thermocouples, to measure its temperature

The outer surfaces of the entire condenser section, including its active cooling portion, were insulated with a 1/2-inch layer of *Armaflex* pipe insulation. The outer diameter of this insulation on the cooling-water jacket was approximately 4.5 inches. The cooling water was supplied from constant-temperature bath (*Neslab* RTE 211) to the annular jacket of the condenser section using two flexible *Neoprene* tubes with 3/8-inch and 5/8-inch inner and outer diameters, respectively; and each of these flexible *Neoprene* tubes was enclosed in 1/2-inch thick *Armaflex* pipe insulation.

3.1.4 Some additional details of the assembled GHP

The core tubes of the evaporator, adiabatic, and condensers sections of the GHP were assembled using the KF 25 vacuum flanges (welded to the ends of the core tubes), matching centering rings, fluroelastomer O-rings, and aluminum clamps (specially designed for the KF 25 vacuum flanges). Schematic views of the assembled GHP are provided in Figure 3.1. The KF 25 vacuum flanges allowed easy connection and disconnection of the three main sections of the GHP; they have a vacuum rating of 1×10^{-8} Torr, and the centering rings and O-rings used with them are reusable. The total length of the assembled GHP was 27.75 inches.

The dimensions of the three main sections of the GHP were determined on the basis of following considerations, as elaborated by Boopathy (2017): 1) the workspace available in the Heat Transfer Laboratory of the Department of Mechanical Engineering at McGill University; 2) the machining facilities, instrumentation, and materials that were available for this work; 3) assessments of the investigations and results available in the published literature; 4) results of computer simulations done with a rudimentary quasi-one-dimensional model of the GHP; and 5) the overall budget available for this work.

With the evaporator section discussed in Subsection 3.1.1, 89 ml of distilled water were required to achieve an initial fill ratio (volume of the liquid pool to the total volume between solid components within the evaporator section up to the top of its active-heating portion) of 100 %.

3.2 Overview of the Experimental Setup and Synopsis of the Related Improvements

A schematic illustration and photographs of the overall experimental setup are given in Figures 3.7 and 3.8, respectively. It consisted of the following main components: the GHP; a vacuum circuit (consisting of a vacuum pump, electronic and mechanical vacuum gauges, plug valves, and suitable connecting tubes and hoses); a hot-air blower in a soundproof box (connected via a suitable hose to a wooden cabinet that housed some key parts of the vacuum circuit; this arrangement prevented condensation of the water vapor in the portions of the vacuum circuit that were connected to the vacuum gauges); a filling circuit (made up of a graduated glass burette, needle and plug valves, and appropriate connecting tubes and hoses); a constant-temperature bath (connected to the cooling-water jacket of the condenser-section of the GHP via suitable hoses); DC power supplies; a data acquisition and control system; and a PC with a USB-GPIB interface.

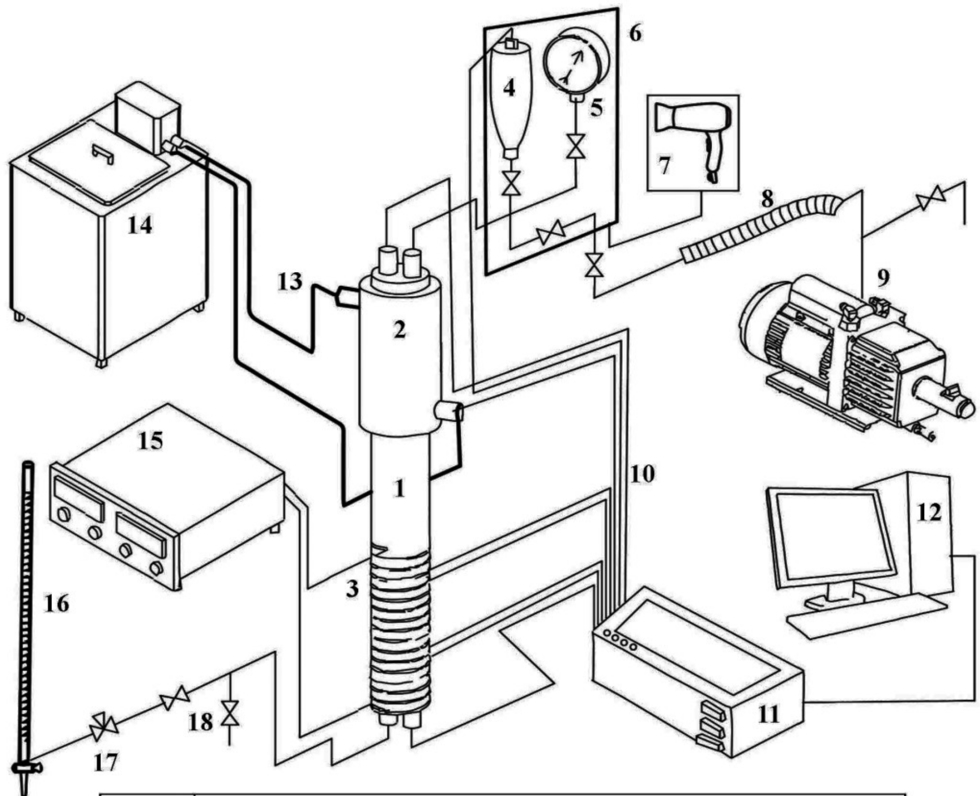

PART No.	DESCRIPTION
1	GRAVITY HEAT PIPE (GHP)
2	COOLING-WATER JACKET OF THE GHP
3	TEFLON-COATED NICHROME HEATING WIRE
4	ELECTRONIC VACUUM GAUGE
5	MECHANICAL VACUUM GAUGE
6	WOODEN CABINET
7	HOT-AIR BLOWER IN A SOUNDPROOF BOX
8	FLEXIBLE METAL VACUUM HOSE (SS 316)
9	VACUUM PUMP
10	TYPE-E THERMOCOUPLES
11	DATA ACQUISITION AND CONTROL SYSTEM
12	PC WITH USB-GPIB INTERFACE
13	COOLING-WATER SUPPLY LINE
14	CONSTANT-TEMPERATURE BATH
15	DC POWER SUPPLY
16	GRADUATED GLASS BURETTE
17	NEEDLE VALVE
18	PLUG VALVES

Figure 3.7 Schematic illustration of the overall experimental setup.

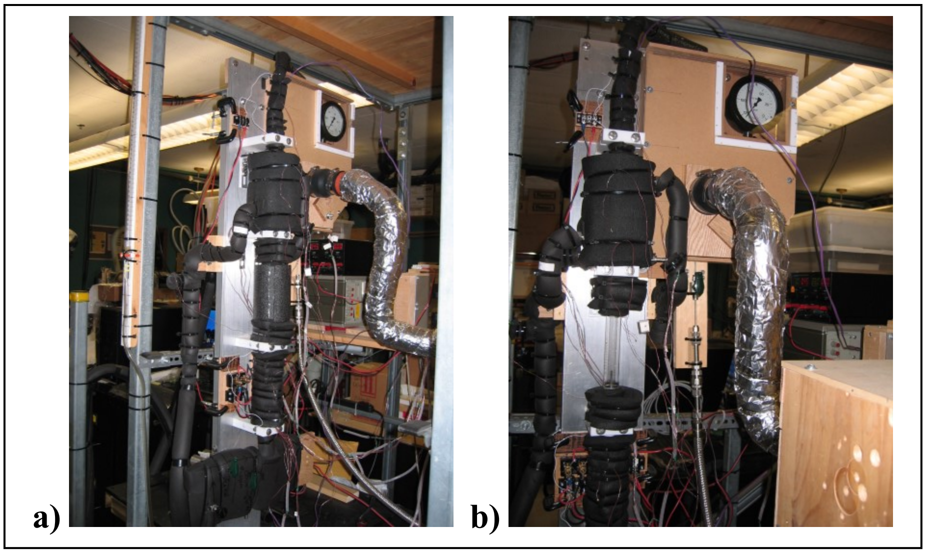

Figure 3.8 Photographs of the overall experimental setup with a) fully insulated GHP and b) GHP with insulation removed from the flow visualization segment of the adiabatic section.

As was mentioned earlier, the complete original experimental setup (including the GHP) of Boopathy (2017) was first fully refurbished and tested, and then some essential improvements to it were implemented. The improvements were needed to allow the experiments to be conducted over extended periods of time with minimal disturbance to other persons working in the Heat Transfer Laboratory and for reliable assessments of four different techniques proposed for mitigating the GBP that occurs in the GHP at relatively low power inputs. A synopsis of these improvements (along with some related details to provide the proper context) is presented in the remainder of this section. Descriptions of the four different techniques proposed for mitigating the GBP are presented and discussed later in this chapter (in Section 3.6).

Two of the improvements implemented in this work were the design and implementation of a soundproof box and the incorporation of a new hot-air blower (with improved controls of the air temperature and flow rate). The soundproof box reduced the level of noise emanating from the hot-air blower into the Heat Transfer Laboratory significantly below that without it (the dB levels were not measured, but the noise reduction was significant). The new blower allowed the hot air to be delivered via a well-insulated flexible hose to a wooden cabinet at flow rates and temperatures that were suitable for reliably preventing condensation of the water vapor in the portions of the vacuum circuit connected to the vacuum gauges (water in the lines connected to the vacuum gauges would corrupt their readings and could also damage them irretrievably).

The GHP used in this work was designed for operating temperatures in the range of 20 ºC to 80 ºC (to be relevant to some HVAC, geothermal, and other applications mentioned in Chapter 1) and distilled water as the working fluid (the rationale for this choice of the working fluid is presented in Section 3.3). Thus, this GHP (which is a closed two-phase thermosyphon with boiling in the evaporator section, condensation in the condenser section, and return of the condensate to the evaporator under the action of gravity, as was elaborated in Chapters 1 and 2) had to be run at mean pressures below atmospheric pressure and it was crucial to exclude (or minimize to the extent possible) the ingestion of air during its operation (as the presence of air, a "non-condensable" gas at the operating temperatures of this GHP, even in amounts as low as 2% by volume, could severely compromise the rate of condensation of the water vapor [Rohsenow et al. (1961); Carey (1992)] and degrade its heat-transfer performance). Leakage tests conducted on the GHP and its vacuum circuit after refurbishing the experimental setup implemented by Boopathy (2017) had showed that the level of vacuum retention in it was not adequate. This problem was successfully overcome by implementing the following improvement: the installation of an additional (and new) plug valve in the vacuum circuit of the GHP outside the wooden cabinet. The photograph given in Figure 3.8 b) shows the GHP (without the insulation around the flow-visualization segment of the adiabatic section), the wooden cabinet in the top-right quadrant (housing some key parts of the vacuum circuit), the circular dial of the mechanical vacuum gauge (visible in the top-right side of the wooden cabinet), the new plug valve (with its dark-green handle just below the wooden cabinet), a portion of the soundproof box in the bottom-right quadrant, and the insulated duct (with a shiny aluminum-foil outer layer) that conveyed hot air from the blower (located inside the soundproof box) to the wooden cabinet.

During the refurbishing and testing of the experimental setup implemented by Boopathy (2017), the temperature distributions on the outer surface of the vertical core tube of the evaporator section of the GHP were found to be non-axisymmetric. The cause of this asymmetry was determined to be the off-center insertion of the sheathed thermocouple of the evaporator section (through an off-center *Swagelok* fitting in the bottom endplate) to a 4-inch height within the liquid pool in it; and the sheath of this thermocouple was also found to be slightly bent. To correct this problem, the following improvements were implemented: the sheathed thermocouple was straightened; and it was then reinserted to only a 1-inch height within the liquid pool in the evaporator section (which ensured that its tip was just beneath the cross-sectional plane at the start of the active-heating segment of the evaporator section). This improvement ensured that the sheathed thermocouple did not interfere with the liquid circulation within the active-heating segment and axisymmetric temperature distributions were obtained on the outer surface of the vertical core tube of the evaporator section (to within the ± 0.1 ºC uncertainty of the temperature measurements yielded by the calibrated thermocouples; the related details are elaborated in Subsection 3.7.1). After this improvement, 89 ml of distilled water were required to achieve an initial fill ratio of 100 %, as opposed to 88 ml that were needed in the work of Boopathy (2017).

As was mentioned in Section 3.1, 10 thermocouples were used for measuring temperatures at selected locations on the outer surface of the core tube in the active-heating portion of the evaporator section; another 10 thermocouples were used for measuring temperatures at selected locations on the outer surface of the core tube in the active-cooling portion of the condenser section; two sheathed thermocouples (SS 304 sheath material) were inserted inside the GHP, one each through the endplates of the condenser and evaporator sections; and two thermocouples were used to measure the cooling-water bulk temperature at the inlet and exit ports of the annular jacket of the condenser section. In addition, five thermocouples were used to record temperatures at selected locations of the vacuum circuit; and three thermocouples (each covered with aluminum foil to minimize radiation effects) were used to measure the ambient air temperature at locations adjacent to the evaporator, adiabatic, and condenser sections of the GHP. All these thermocouples were of Type-E (chromel-constantan) and they were calibrated in-house to an accuracy of ± 0.05 ºC over the temperature range 2 ºC to 60 ºC [Boopathy (2017)]. Another improvement implemented in this work was the extension of this calibration temperature range to go from 2 ºC to 100 ºC, to obtain increased flexibility and range in the experiments that were undertaken. As most of the thermocouples were already installed in the GHP by Boopathy (2017), it was not possible to remove and recalibrate them. Thus, in the temperature range of 60 ºC to 100 ºC, the calibration data provided in the work of Boopathy (2017) were supplemented by data provided by the National Institute of Standards and Technology (NIST) for Type-E high-accuracy thermocouples [Burns and Scroger (1989)]. With this approach, however, the accuracy of the measured temperatures in the range 60 ºC to 100 ºC was only ± 0.10 ºC.

The final improvement of the overall experimental setup pertained to the software used for data acquisition and control. A new LabVIEW code was written, tested, and implemented. It allowed the restriction (when desired) of the data acquisition to only the 10 thermocouples installed on the outer surface of the core tube in the evaporator section, which, in turn, permitted faster scanning and recording of the related temperatures (by a factor of more than 10 over those achieved using the previous code). This improvement was necessary for reliably conducting the Fast Fourier Transform (FFT) analyses that were used for quantitative investigations of the GBP in the GHP and the effectiveness of the techniques that were proposed for mitigating it. These techniques and related details (the options, choices, and rationale) are presented and discussed in Section 3.6.

The rationale for the choice of the working fluid and the tube material are discussed in the next section. Additional details of the vacuum circuit, the working-fluid filling circuit, techniques to mitigate the GBP, and some of the supporting instrumentation and equipment are discussed in Sections 3.4, 3.5, 3.6, and 3.7, respectively. Finally, the main procedures that were designed and used to run the experiments are summarized in Section 3.8.

3.3 Rationale for the Choice of the Working Fluid and the Tube Material

In the design of heat pipes for specified operating temperature and pressure ranges, the considerations used for the selection of the working fluid include the following [Reay et al. (2013)]: 1) good stability of the fluid properties on repeated thermal cycling; 2) good wetting of and chemical compatibility with the tube-wall material; 3) moderate vapor pressure; 4) nontoxicity to humans and other relevant safety requirements; 5) high thermal conductivity; 6) high latent heat of vaporization; 7) low dynamic viscosity of both the liquid and the vapor phases; and 8) acceptable freezing and boiling temperatures.

Ammonia, acetone, methanol, ethanol, and distilled water were initially considered for use as the working fluid in this work. However, using the selection considerations given above, and additional considerations such as cost, availability, and the objective of carrying forward the work of Boopathy (2017), double-distilled water was selected as the working fluid for the GHP used in this work. Before using this double-distilled water in the GHP experiments, it was vigorously boiled in a clean vessel (a glass electric kettle was used in this work) for at least 30 minutes (this level of boiling is sufficient to adequately expel the dissolved gases from the water); and then this water was filled (fully) and stored in a clean glass bottle fitted with an air-tight lid.

The core tubes of the GHP must be leak-proof, maintain the inside-to-outside pressure differential across its walls, and enable a good rate of heat transfer to and from the working fluid.

Other considerations that go into the selection of the tube material include following for the chosen operating temperature and pressure ranges [Reay et al. (2013)]: 1) compatibility and wettability with respect to the working fluid; 2) good strength-to-weight characteristic; 3) high thermal conductivity; 4) good machinability and weldability; 5) ready availability and low cost; and 6) maintenance of non-brittleness and strength with repeated thermal cycling.

Aluminum, stainless steel, copper, brass, and titanium are some commonly considered tube materials for heat pipes [Reay et al. (2013)]. Boopathy (2017) selected stainless steel SS 316 as the core-tube material for the evaporator and condenser sections of the GHP, mainly because of its ready availability, excellent strength, resistance to corrosion and brittleness, good machinability, and excellent weldability; and he used Kovar and borosilicate glass for the core tube in the adiabatic section (which incorporated the flow visualization segment), for the reasons provided in Subsection 3.1.2. The GHP designed and constructed by Boopathy (2017) was adopted for use in this work. The combination of water as the working fluid and SS 316 as the tube material, although commonly used, has an issue related to the generation and accumulation of hydrogen (over time) which usually collects as a non-condensable gas in the condenser section of the heat pipe [Reay et al. (2013)]. However, this issue becomes significant only at the elevated operating temperatures (~250 ºC or higher) in the presence of metal oxides. As the temperatures in experiments undertaken in this work ranged from 20 ºC to 90 ºC (maximum temperature reached only in a few cases), the water-stainless-steel (SS 316) combination was considered acceptable.

3.4 Vacuum Circuit and Vacuum Gauges

A vacuum circuit was designed and incorporated in the overall setup to enable the following important steps in the experimental procedures: 1) leak testing of the GHP prior to filling it with the working fluid; 2) degassing of all inner surfaces of the GHP; 3) degassing of the working fluid; 4) removal of non-condensable gases from within the GHP and the tubes in the vacuum and filling circuits; and 5) assisting with the filling and metering of the working fluid.

A schematic illustration of the vacuum circuit (including the vacuum gauges, vacuum pump, and connecting tubes) used in this work is given in Figure 3.9. A two-stage oil-sealed rotary-vane vacuum pump (*Edwards* RV8) was used. A photograph of this vacuum pump and its operating characteristics are given in Figure 3.10.

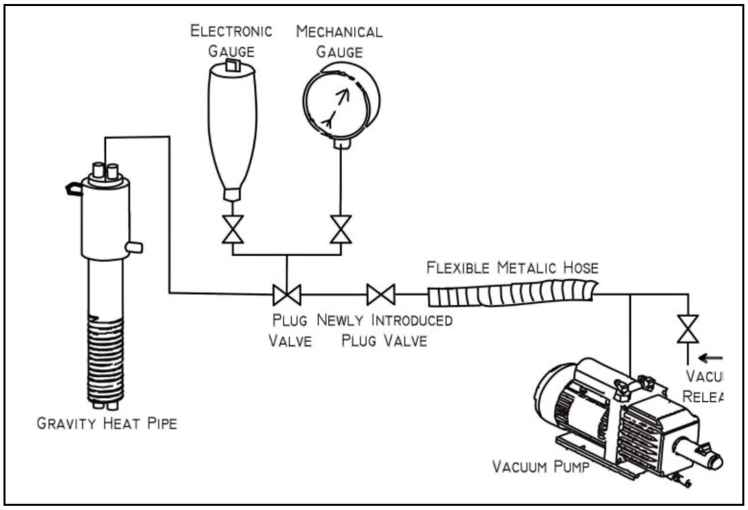

Figure 3.9 Schematic illustration of the GHP connected to the vacuum circuit.

Edwards RV8 Vacuum Pump	
Ultimate Pressure	2×10^{-3} mbar
Ultimate Pressure (Gas Ballast Mode)	3×10^{-2} mbar
Maximum Allowed Inlet Pressure	1500 mbar

Figure 3.10 The vacuum pump used in this work and its main characteristics.

The selected vacuum pump (see details in Figure 3.10) offers features that were adequate for the experiments undertaken in this work, with and without the gas-ballast mode. The gas-ballast mode ensures that any water vapor that enters the vacuum pump stays and exits in the vapor state; and thus, it keeps the vacuum-pump oil unadulterated and helps in sustaining the service life and performance of the pump. The vacuum pump was connected to the vacuum circuit using a K 25 vacuum flange assembly, a short length of 3/8-inch *Swagelok* SS 316 tubing, and a 3/8-inch *Swagelok* SS 316 T-junction (see Figure 3.9). One end of the straight portion of this T-junction was connected to a plug valve (which was used to allow air into the circuit and release the vacuum when desired) and its other end was connected via a 3/8-inch *Swagelok* SS 316 quick-connect fitting to one end of a 6-ft long flexible vacuum hose (made of SS 316; and manufactured by *Swagelok*); and the other end of this flexible hose was connected via another 3/8-inch *Swagelok* SS 316 quick-connect fitting to a *Swagelok* plug valve (newly introduced in this work) which allowed isolation of the vacuum pump after the creation of the desired vacuum conditions inside the GHP. It should be noted that the newly-added *Swagelok* plug valve (PTFE seated) was located outside the wooden cabinet (which housed other parts of the vacuum circuit, including the vacuum gauges) to avoid exposing it to the hot air from the blower and compromising its sealing capacity. A photograph of the wooden cabinet and the parts of the vacuum circuit housed within it is provided in Figure 3.11.

Two vacuum gauges were connected in parallel to the vacuum circuit (as shown in Figures 3.7 and 3.9). These two vacuum gauges, one a mechanical Bourdon-tube gauge (*Edwards* CG16K) and the other an electronic capacitance-type diaphragm gauge (*Inficon* CDG020D), and their characteristics are shown in Figure 3.12. The mechanical gauge allowed a quick and convenient visual check of the vacuum conditions inside the GHP; and the electronic gauge provided the desired accuracy in measurements of the absolute pressure in the GHP and allowed computer-based acquisition of this data.

Figure 3.11 Photograph of the wooden cabinet housing parts of the vacuum circuit, including a mechanical vacuum gauge and an electronic vacuum gauge.

Edwards CG16K Dial Gauge **Inficon CDG020D Gauge**

Gauge	Range	Accuracy	Resolution	End Connection
Edwards CG16K	0 - 125 mbar	±2 % of FS	0.5 mbar	KF 16
Inficon CDG020D	0 – 1000 Torr	±0.5 % of Reading	0.05 % FS	KF 16

Figure 3.12 Photographs of the mechanical (left) and electronic (right) vacuum gauges and a listing of their characteristics.

The average temperature of the water vapor inside the condenser section varied between 20 ºC to 40 ºC during the experimental runs, and the average temperature of the water (and vapor) in the evaporator section ranged between 33 ºC to 50 ºC. To ensure that the water vapor did not condense inside the vacuum gauges and the tubes and fittings that connected them to the GHP, they were unclosed in a wooden cabinet (see Figures 3.7 and 3.11) and hot air was supplied to this cabinet from a blower to maintain their temperatures between 55ºC to 70 ºC. The vacuum gauges selected for this work could operate reliably at temperatures up to 75ºC (based on the specification provided by their manufactures). The hot-air blower was a high-quality hair dryer that had several different heating and flow-rate settings. This blower was housed in a special soundproof box that had specially designed adjustable ventilation slots. In addition to this hot-air arrangement, the vacuum line coming directly out of the top endplate of the GHP condenser section was also heated by passing electrical current through a Teflon-coated nichrome wire wound tightly and closely around it. The temperatures of the above-mentioned components of the vacuum circuit were continuously monitored during the experiments with the GHP and maintained in the desired range (55 ºC to 70 ºC) by adjusting the heating arrangements discussed above.

3.5 Working-Fluid Filling Circuit

The working-fluid filling circuit is schematically illustrated in Figure 3.13. It consisted of the following components: a graduated 100-ml glass (borosilicate) burette with a stopcock; a *Swagelok* needle valve (SS 316 body and 1/8-inch compression fittings at each end; PTFE seat for the stem); two *Swagelok* plug valves (SS 316 body and 1/8-inch compression fitting at each end; PTFE seals); 1/8-inch diameter SS 316 tubing; and a *Swagelok* 1/8-inch T-junction with compression fittings at each of its three ends. The filling circuit was connected to the glass burette at one end using a *Swagelok* 1/4-inch-hose-barb-1/8-inch-tube reducer (attached to one end of the needle valve) and a flexible Tygon tube (1/4-inch ID; 7/16-inch OD); and at the other end, it was connected to the GHP via 1/8-inch SS 316 tube and a *Swagelok* 1/8-inch bore-through compression fitting welded to the bottom endplate of the evaporator section.

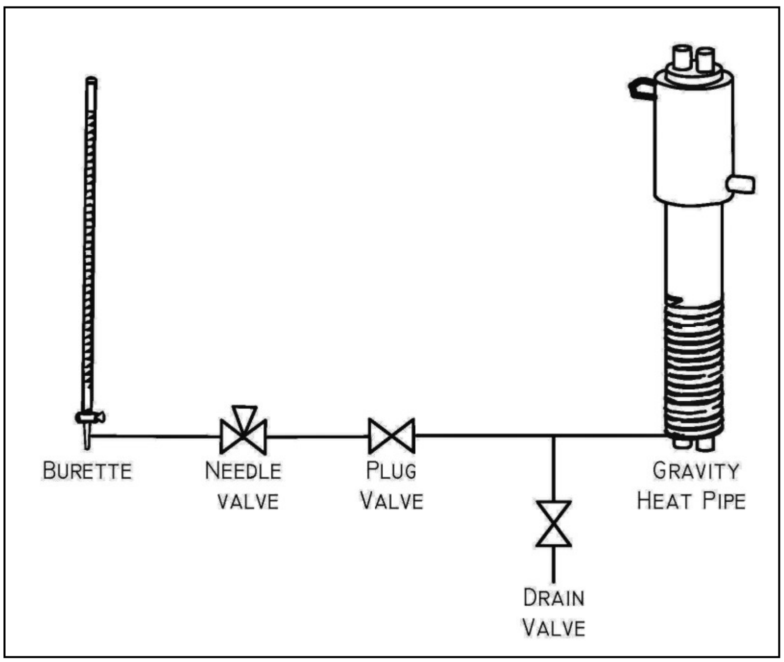

Figure 3.13 Schematic illustration of the working-fluid filling circuit connected to a graduated glass burette at one end and the GHP at the other end.

The glass burette was used to hold the degassed working fluid and to administer a desired amount of it into the GHP in a controlled manner using the needle valve. After the completion of the filling operation, the plug valve was used to isolate the GHP from the rest of filling circuit; the drain valve (also a plug valve) was kept closed during the filling procedure and opened when draining the working fluid from the GHP.

3.6 Techniques to Mitigate Geyser Boiling

Discussions of the geyser boiling phenomenon (GBP) in GHPs and a review of some key publications on it were presented in Chapter 1, so they are not repeated here. In general, the GBP in GHPs occurs at relatively low power inputs (inadequate for sustaining nucleate boiling in the liquid pool in the evaporator) [Jafari et al. (2016); Pabon et al. (2019)]. This was the finding in this work too, in which the GHP (described in Section 3.1) was operated in a vertical orientation (zero angle of inclination) and fill ratios (FR) of 100 %, 150 %, and 175 % (volume of the liquid pool to the total volume between solid components up to the end of the active-heating portion of the evaporator section) in all experimental runs.

3.6.1 Background, selected approaches, and rationale

Several options for mitigating the GBP in GHPs have been reported in the published literature. They include the following: 1) reducing the fill ratio (to values significantly below 100%) [Noie et al. (2007) ; Emami et al. (2008); Smith et al. (2016); Jafari et al. (2017); Alammar et al. (2018a, 2018b)]; 2) increasing the inclination angle of the entire GHP or only the evaporator section for a bent GHP (to values significantly beyond the vertical, towards the horizontal) [Emami et al. (2008); Smith et al. (2016); Jafari et al. (2016, 2017); Alammar et al. (2018a, 2018b)]; 3) reducing the aspect ratio (length/inner diameter) of the core tube of the evaporator section (to around one or lower) [Jouhara and Robinson (2010); Smith et al. (2018a, 2018b); Elkholy and Kempers (2020)]; 4) using suitable combinations of the base fluid, a chemical stabilizer, and nanoparticles (such combinations are often referred to as nanofluids) as the working fluid (to create a “nano-porous” layer on the inner surface of the evaporator and a “bubble surface” at the liquid-vapor interface) [Shanbedi et al. (2012, 2014); Heris et al. (2016); Kujawska et a. (2019)]; 5) adding surfactants to the working fluid (to reduce the liquid-vapor surface tension and increase wettability, and thereby reduce the departure-diameter of the vapor bubbles) [Kuncoro et al. (1995); Zhao et al. (2019)]; and 6) increasing the roughness of the inner surface of the core tube in the evaporator section (to increase the number of nucleation sites, increase the wettability, and reduce the departure-diameter of the bubbles compared to their values for a smooth surface) [Solomon et al. (2017); Zhao et al. (2019); Vieira et al. (2020)].

The above-mentioned Options 1 to 4 were considered unsuitable for HVAC and vertical-bore-hole geothermal applications, in which it is desirable to have relatively inexpensive GHPs with simple construction (suitable for high-volume manufacturing), vertical orientation, large values of aspect ratio (of the order of 10 or higher in the HVAC and around 1000 in the geothermal applications), 100 % static fill ratio (which allows good harvesting of the heating potential of the active portion of the evaporator section), long service life (about 10 to 20 years), and safe working fluid (see discussion in Section 3.3). Furthermore, at fill ratios less than 100 % and inclination angles of about 30º and higher, dry-out (interruptions or dry spots in the liquid film returning the condensate along the inner surface of the core tube of the GHP to the liquid pool in the evaporator section) could occur [Jafari et al. (2016, 2017); Boopathy (2017)]; and inclination angles higher than 30º are usually needed to avoid or mitigate GBP [Emami et al. (2008); Smith et al. (2016); Jafari et al. (2016, 2017); Alammar et al. (2018a, 2018b)]. The above-mentioned Option 5 was considered unsuitable for the experiments undertaken in this work, as that would require multiple disconnections and reconnections of the GHP from the vacuum and working-fluid filling circuits (to allow disassembly, cleaning, and reassembly of the GHP, for trials of various combinations surfactants and water), and the experimental setup was not designed for it; and time and budgetary limitations did not allow the required level of modifications of the overall setup within this scope of this work. However, Option 5 is promising and suggested as a possible extension of this work.

In the context of the discussions in previous paragraph, it was decided to explore the possibility of mitigating GBP by using the following three approaches: 1) introducing artificial structured roughness on the inner surface of the core tube of the evaporator section (this approach allows roughness control and optimization, so it is more effective than using natural statistical roughness); 2) breaking large bubbles (when or if they occur) in the evaporator section into smaller ones using a suitable passive 'bubble-breaker' (this approach is a novel one for GHPs, but it has been used earlier for breaking large bubbles of air into smaller ones in forced isothermal upward flow of water in vertical tubes, for enhancing mixing in bubble-column reactors used in biochemical industries, wastewater treatment plants, and absorption refrigeration systems [Gadallah and Siddiqui (2015); Kalbfleisch and Siddiqui (2017)]); and 3) combining inner-surface roughness and a passive bubble-breaker.

3.6.2 Some ways to create inner-surface roughness, selected option, and related details

Solomon et al. (2017) used an electrochemical deposition process to obtain a thin, porous copper coating on the inner surface of a copper tube; Zhao et al. (2019) used a special chemical etching and coating process to create very thin porous layers on the inner surface of copper tubes to modify their wettability; and in a recent work (published after the experiments in this work were completed), Vieira et al. (2020) used five layers of 60 x 60 copper-wire mesh that were first spot-welded and then diffusion-bonded (using high pressure and temperature) to the copper plates in a *flat* evaporator of a *closed-loop* thermosyphon to obtain the desired inner-surface roughness. The design and construction of several different new evaporator sections with different inner-surface roughness, using one or more of the three procedures mentioned above in this paragraph, was not viable within the scope of this M.Sc. thesis work (due to time and budgetary constraints). As was mentioned earlier, the GHP designed and constructed by Boopathy (2017), and described in Section 3.1, was used in this work to study the GBP and propose and assess ways to mitigate it.

Thus, it was decided to use a stainless steel (SS 316) wire mesh to create the artificial structured roughness on the inner surface of the SS 316 core tube of the evaporator section, using the following procedure: 1) cut the SS 316 wire mesh to the right dimensions (width and height); 2) roll (wrap) it tightly around a cylindrical mandrel of diameter smaller than the 0.935-inch inner diameter of the core tube of the evaporator section (a hard-wood dowel rod of 3/8-inch diameter, *Home Depot* part # 02538-R0048C-SW, was used as this mandrel); 3) insert the mandrel with rolled wire mesh on it into the core tube; 4) release the wire mesh to allow it to spring outwards (using its intrinsic elasticity) and push tightly against the inner surface of the core tube; and 5) retract the mandrel. SS 316 was chosen as the material for the wire mesh to ensure perfect chemical compatibility with the SS 316 core tube of the evaporator section, and thereby avoid the creation of a galvanic cell in the presence of water (the working fluid) and related corrosion issues.

Five different SS 316 woven wire meshes manufactured by *McMaster-Carr* were considered for creating the roughness on the inner surface of the core tube of the evaporator section of the GHP: 10×10 (model 9319T142); 20×20 (model 9319T156); 40×40 (model 9319T173); 60×60 (model 9319T176); and 100×100 (model 9319T183). The notation (## × ##) indicates number of modular square cells per inch along each side of a rectangular piece of the mesh. The final choice of the mesh was dictated by five important requirements related to the five-step procedure described in the previous paragraph: 1) ease in the cutting of the mesh to precise dimensions using a sturdy knife (fitted with a HSS blade) and a jig specially fabricated in-house for this purpose; 2) no significant unravelling of the wires in the mesh after the cutting operation; 3) ease in rolling (wrapping) the cut piece of the mesh tightly around the cylindrical mandrel; 4) easy insertion of the mandrel and the wire mesh inside the core tube of the evaporator section; and 5) adequate intrinsic elasticity of the mesh, which had to be sufficient to push it tightly against the inner surface of the core tube after insertion. After many trials, it was found that these requirements were met by only the 60 × 60 mesh, so it was the only one used in the final experiments.

The chosen 60 × 60 woven wire mesh (SS 316; *McMaster-Carr* model 9319T176) is made of wires of 0.0075-inch diameter with a 0.009-inch × 0.009-inch square opening in between the wires. A photograph of some pieces of this mesh and the special jig that was designed, constructed, and used for cutting this mesh into rectangular pieces of the required precise dimensions is given in Figure 3.14. The precise dimensions were required to ensure that the longer edges of a single layer of the cut rectangular piece of the mesh met as perfectly as possible within the core tube of the evaporator section (after its insertion and springing out to tightly press against the inner surface of the tube). The base of the special jig was a large wooden plank clamped to the wooden top of a sturdy lab stool. To prevent the woven wires of the mesh from coming loose and getting caught in the edge of the HSS blade of the knife during the cutting process, the mesh was clamped in place on the wooden support plank with a thick straight wooden piece on top (this upper wooden piece also served as a guide for the desired straight cuts). Clean and accurate cuts of the 60 × 60 woven wire mesh were obtained by using 5 to 8 passes of the edge of the HSS knife blade.

Figure 3.14 Photograph of some pieces of the SS 316 60 × 60 wire mesh and the jig that was used to precisely cut this mesh into rectangular pieces of the desired dimensions.

3.6.3 Some passive bubble-breaker designs, selected option, and related details

In the works of Gadalah and Siddiqui (2015) and Kalbfleisch and Siddiqui (2017), honeycomb-type (400 cells per inch) and mesh-type (with square-cross-section pores of side 1 mm to 4 mm) “monolith” (a single upright structure) bubble-breakers were used (with length-to-diameter ratio of the monolith close to one). These honeycomb- and mesh-type monolith bubble-breakers were held in place using a rubber gasket between their outer surface and the inner surface of the glass tubes (of 15 mm and 16 mm inner diameter, respectively) in which they were used. Such bubble-breakers were not a viable option in this work, as heat transfer from the inner surface of the active-heating portion of the core tube in the evaporator section had to be enhanced and not hindered (so rubber gaskets could not be used); and a monolith structure with a honeycomb or wire-mesh cross-section and length-to-diameter ratio of close to one could lead to the creation of a vapor layer adjacent to the inner surface of the core tube and cause hot spots akin to those that occur under dry-out conditions. Furthermore, after the breaking up of a big bubble into smaller ones using the bubble-breaker, it is important to ensure that the smaller bubbles do not interact and coalesce into larger bubbles inside the evaporator section (this requirement could not be met with the monolith bubble-breakers mentioned above). Thus, a novel bubble-breaker was designed, constructed, and used. It is described in the next paragraph.

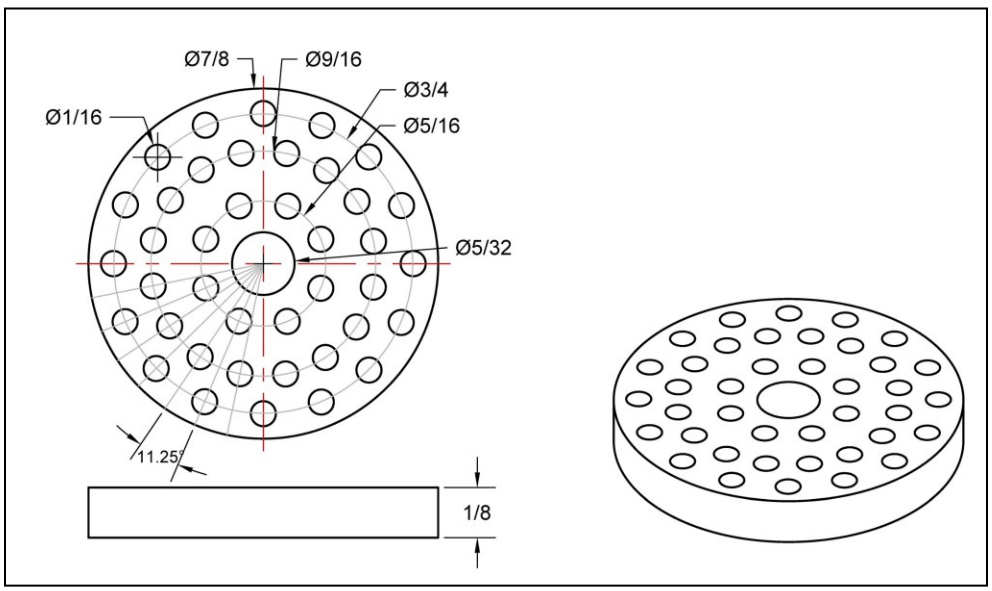

Figure 3.15 CAD drawings of a perforated disk (the length dimensions are in inches).

The novel bubble-breaker used in this work was made of identical perforated disks positioned at regular intervals along a threaded rod. These disks were designed so that they could be fabricated using either manual or numerically controlled conventional machines (simple or turret lathe; radial drill press; milling machine). They were cut from a 1-ft long precision 7/8-inch diameter stainless steel (SS 316) rod purchased from *McMaster-Carr* (model 8936K19). CAD drawings of one such perforated disk are given in Figure 3.15. Each disk had a 1/8-inch thickness (H_{disk}); a central hole of 5/23-inch diameter (for insertion of the threaded rod on which the disks were assembled); and 40 perforations with 1/16-inch diameter (D_{perf}) and centers located uniformly around three concentric circles (the centers of eight, 16, and 16 perforations were placed uniform around concentric circles of 5/16-inch, 9/16-inch, and 3/4-inch diameters, respectively; and the centers of the perforations around these three concentric circles were staggered with respect to each other, to maximize their center-to-center spacing).

The perforated disks were assembled, with a 1-inch interval between the circular surfaces of adjacent disks, on a “super corrosion resistant” SS 316 fully threaded 1-ft long rod (right-hand 5-40 thread; *McMaster-Carr* model 93250A215); and each disk was firmly held in place on the threaded rod using two standard-profile SS 18-8 hex nuts (right-hand 5-40 thread; 5/6-inch width; 7/64-inch height; *McMaster-Carr* model 91841A006), with one nut each on its top and bottom surfaces. Twelve such perforated disks were fabricated. A photograph of these 12 disks is provided in Figure 3.16 (only 10 were used); and a photograph of a part of an assembly of these perforated disks on the threaded rod is given in Figure 3.17. It should be noted here that the option of ordering made-to-specifications prefabricated perforated disks, with smaller thickness and perforations of smaller diameter than those indicated in Figure 3.15, from specialized manufacturers was considered. However, after due consideration, this option was rejected because of time and budgetary limitations (this option is recommended as a possible extension of this work).

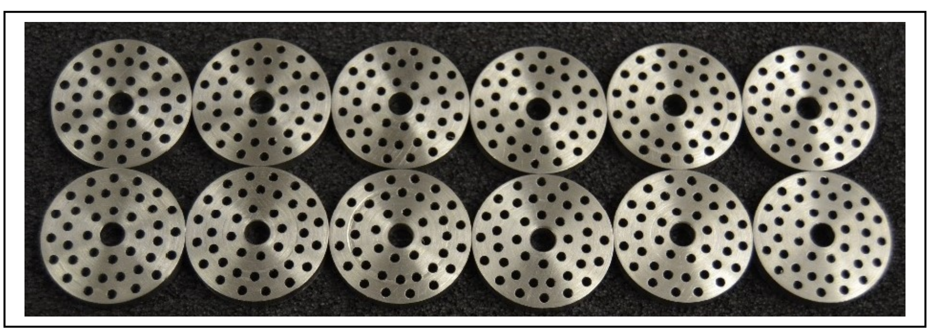

Figure 3.16 Photograph of 12 machined perforated disks.

The layout and dimensions of the perforated disk depicted in Figure 3.15 were adopted after considering several other designs, for the following reasons: the SS 316 disks of 1/8-inch thickness could be machined without any significant challenges; the 1/16-inch diameter perforations could be drilled through the 1/8-inch thick disk in a reliable manner using a carbidetipped HSS drill bit; and the 40 perforations (a relatively large number) could be accommodated on the circular disk in a well-distributed manner with adequate center-to-center spacing and without getting too close to the outer circumference of the disk.

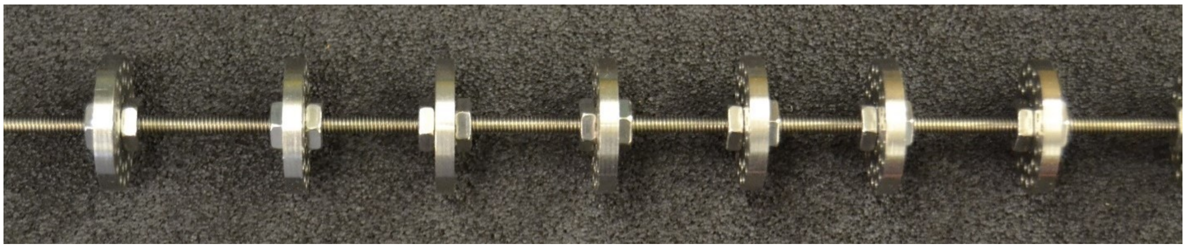

Figure 3.17 Photograph of a part of an assembly of perforated disks on a threaded rod, with the nuts used to maintain a 1-inch gap between the surfaces of adjacent disks.

3.6.4 Estimation of the departure-diameter of vapor bubbles obtained with the woven- wire-mesh inner-surface roughness and related details

The work of Guichet et al. (2019) provides a detailed review of many published works that discuss the underlying physics of nucleate boiling and provide correlations for the corresponding heat transfer coefficients, the rate of growth of bubbles that form on the surfaces of heated walls, and the departure-diameter of these bubbles (diameter of an effectively spherical bubble when it leaves the surface of the heated wall). Several of these papers were discussed in the literature review presented in Chapter 1; and a few of the correlations and their underlying physics were presented and discussed in Chapter 2. In summary, there is considerable scatter (uncertainties) in the predictions obtained using the available correlations and most of them pertain to nucleate pool boiling on surfaces of *horizontal* heated walls or the outer surfaces of *horizontal* heated cylinders in *large* enclosures, in which the so-called confinement number = {(bubble departure-diameter) / (horizontal dimension of enclosure)} << 1 [Smith et al. (2018a, 2018b)]. Furthermore, none of the available correlations apply to either the smooth *vertical curved* inner surface of the active-heating portion of the evaporator section of the GHP used in this work or to surfaces (horizontal or vertical; curved or flat) with roughness created by an adjacent wire mesh.

Thus, a very rudimentary approach was adopted to obtain a rough estimate of the *maximum* effective diameter of a non-spherical bubble (diameter of a spherical bubble of the same volume) just as (or just after) it departs from the surface of the 60 × 60 woven wire mesh. In this approach, ignoring the effects associated with the agitation of the surrounding liquid, inertia, and liquid-vapor phase-change, it was assumed that at the instant of departure, the surface tension force that keeps the bubble attached to the perimeter of the open area of a modular square cell of the mesh is equal to the vertical buoyancy force on the volume of the bubble:

$$Peri_{\substack{sq.\,open\\ area\ mesh}}\ \sigma = \{Vol_{\substack{max\ departure\\ bubble\ mesh}}\}\, g\,(\rho_l - \rho_v) = \{(4/3)\pi(D_{\substack{max\ departure\\ bubble\ mesh}}/2)^3\}\, g\,(\rho_l - \rho_v) \qquad (3.1)$$

In this equation, σ is the surface tension; g is the acceleration due to gravity (9.81 m/s^2); and ρ_l and ρ_v are the densities of the liquid surrounding the bubble and the saturated vapor inside it, respectively.

In the experiments undertaken in this work, the range of the average temperature of the liquid pool in the evaporator section ranged from 33.75 ºC to 50.01 ºC. Using this range of temperature, the property data for water (liquid and vapor) in Incropera and DeWitt (2002) and Moran and Shapiro (1998), and Equation (3.1), the range of values of the *maximum* departure-diameter for the bubbles leaving the 60 × 60 mesh was estimated as 2.30 mm to 2.33 mm; and this range of bubble diameters leads to a bubble confinement number ($D_{max\,departure\,bubble\ mesh} / D_i$) < 0.10. Thus, the 60 × 60 wire mesh was considered satisfactory for producing conditions favorable for nucleate pool boiling [Smith et al. (2018a, 2018b)]. It should also be noted here that the inclusion of the effects of liquid agitation, inertia, and liquid-vapor phase-change during the growth of the bubble on the open area of the 60 × 60 wire mesh would reduce the *maximum* departure-diameter of the bubble to values well below those yielded by Eq. (3.1).

3.6.5 Estimation of the diameter of vapor bubbles obtained with the bubble-breaker and related details

CAD drawings and a photograph of the perforated disks of the bubble-breaker are given in Figures 3.15 and 3.16, respectively, and a photograph of a portion of the assembled unit is presented in Figure 3.17. With the 1/16-inch diameter of the perforations in the disk (D_{perf}), the 0.935-inch inner diameter (D_i) of the core tube of the evaporator section of the GHP, and the uniform 1-inch vertical interval between the circular surfaces of adjacent disks ($H_{vert\,interval,disks}$), the vapor bubbles with effective diameter smaller than or equal to D_{perf} had containment numbers in the horizontal and vertical directions (D_{perf} / D_i and $D_{perf} / H_{vert\,interval,disks}$, respectively) of less than 0.067. These conditions are favorable for nucleate pool boiling [Smith et al. (2018a, 2018b)].

The average temperature of the liquid water in the evaporator section was in the range 33.75 ºC to 50.01 ºC. For these conditions, using the water properties in Incropera and DeWitt (2002) and Moran and Shapiro (1998), the following conclusions could be made: a 1-inch vertical column of liquid water creates a hydrostatic pressure difference of about 250 Pa; and a decrease of 250 Pa in the pressure of the vapor in a bubble at temperatures of 33.75 ºC and 50.01 ºC increases its volume by 5% and 1.34 %, respectively; and using a conservative safety factor of two to account for liquid-vapor phase change during the passage of a bubble between the circular surfaces of adjacent disks, these volume changes would be 10% and 2.68%, which imply changes in bubble diameter of roughly 3.25 % and 1.6 %. Thus, with the design depicted in Figures 3.15 – 3.17, it was unlikely that the vapor bubbles with (effective diameter) ≤ D_{perf} interacted with each other and coalesced in the 1-inch vertical interval between the circular surfaces of adjacent disks.

Vapor bubbles with effective diameter a *bit* larger than D_{perf} may squeeze through the perforations in the disks of the bubble-breaker without breaking up (and emerge on the other side of the disks with roughly the same diameter); however, those with effective diameter significantly larger than D_{perf} would be broken up into bubbles of smaller effective diameter. For the larger bubbles that were broken up by the bubble-breaker, the *maximum* effective departure-diameter of the smaller bubbles created at the exit plane of the perforations in the disks was estimated using a very rudimentary approach akin to that described above in Subsection 3.6.4 for estimating $D_{departure\,bubble\,mesh}$ using Eq. (3.1). Thus, ignoring the effects associated with the agitation of the surrounding liquid, inertia, and liquid-vapor phase-change, it was assumed that at the instant of departure, the surface tension force that keeps the bubble attached to the perimeter of the exit plane of the perforation is equal to the vertical buoyancy force on the volume of the bubble:

$$(\pi D_{perf})\sigma = \{Vol_{\substack{max\ departure \\ bubble\ perf}}\}\, g\,(\rho_l - \rho_v) = \{(4/3)\pi(D_{\substack{max\,departure \\ bubble\ perf}}/2)^3\}\, g\,(\rho_l - \rho_v) \tag{3.2}$$

In this equation, σ is the surface tension; g is the acceleration due to gravity (9.81 m/s^2); and ρ_l and ρ_v are the densities of the liquid surrounding the bubble and the saturated vapor inside it, respectively.

For the range of the average temperature of the liquid pool in the evaporator section in the experiments (33.75 ºC to 50.01 ºC), using Equation (3.2) and the property data for water (liquid and vapor) in Incropera and DeWitt (2002) and Moran and Shapiro (1998), the range of $D_{max\,departure\,bubble\;perf}$ was estimated as 4.00 mm to 4.10 mm. Thus, ($D_{max\,departure\,bubble\;perf} / D_i$) < 0.173, an upper bound of this bubble confinement number that is a bit high for ensuring nucleate pool boiling [Smith et al. (2018a, 2018b)]. However, again, it should be noted here that the inclusion of the effects of liquid agitation, inertia, and liquid-vapor phase-change during the growth of the bubble on the exit plane of the perforation would most likely reduce the $D_{max\,departure\,bubble\;perf}$ to values well below those yielded by Eq. (3.2). Another important point to note is that the interface between the vapor within bubbles and the heavier liquid water above it is prone to the Rayleigh-Taylor instability [Tritton (1988)]. So, once the vapor starts to flow through any particular perforation on the bubble-breaker disk, it will keep flowing through that one perforation, rather than flow through multiple adjacent perforations. Thus, the coalescence of the smaller bubbles (with $D_{max\,departure\,bubble\;perf}$ between 4.00 mm to 4.10 mm) as they travel the 1-inch vertical interval between the upper circular surface of one perforated disk of the bubble-breaker to the bottom circular surface of the adjacent one was considered highly unlikely.

3.6.6 Proposed techniques

The introduction of inner-surface roughness (as described in Subsection 3.6.2), the bubble-breaker (described in Subsection 3.6.3), and combinations of these approaches were used to propose four different techniques to mitigate the GBP in the GHP use in this work. These four techniques and then some concluding remarks are presented in the next five subsections.

3.6.6.1 Single-layer-wire-mesh (SLWM) technique

In this technique, a single layer of the 60 × 60 SS 316 woven wire mesh was inserted into the evaporator section of the GHP. The cut rectangular piece of the wire mesh had a 10-inch height and a 2-25/32-inch width. Photographs of this single layer of the cut woven wire mesh inserted into the evaporator section are presented in Figure 3.18. After insertion, a 0.375-inch-long portion of the mesh protruded above the 9.625-inch total inner length of the evaporator section (and facilitated the extraction of the mesh after the completion of the related experiments); and the width of the mesh (chosen after several preliminary trials) ensured that its 10-inch-long edges met one-another almost perfectly after it sprung back against the inner surface of core tube of the evaporator section. The cut piece of the woven wire mesh used in this technique had a mass of 16.976 g (average value of 10 measurements obtained with an electronic balance, *Acculab* VI-350), which was used to determine its volume. With this mesh inserted into the evaporator section, 87 ml of water were needed to obtain an initial (static) fill ratio (FR) of 100 %.

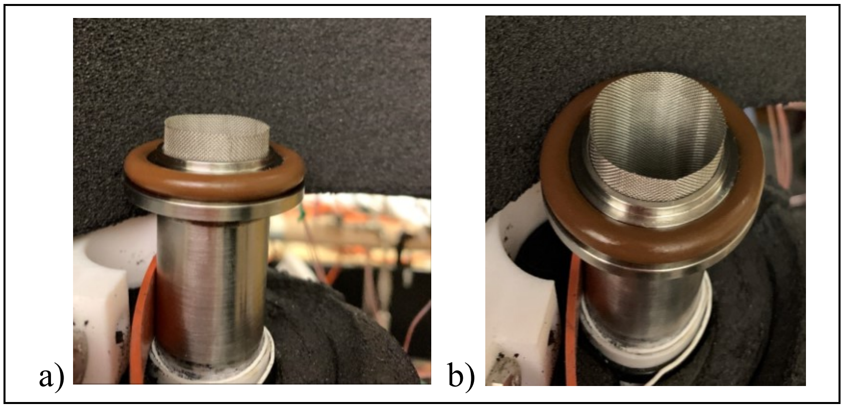

a) b)

Figure 3.18 Photographs of the upper portion of a single layer of 60 × 60 wire mesh inserted inside the core tube of the evaporator section of the GHP: a) side view; and b) top view.

3.6.6.2 Triple-layer-wire-mesh (TLWM) technique

In this technique, three layers of the 60 × 60 SS 316 woven wire mesh were inserted into the evaporator section of the GHP, using a cut rectangular piece of 8-inch height and 8-inch width. It was expected that compared to a single layer, the three layers would decrease the effective open area and increase the spring-back force that pushes the mesh against the inner surface of the core tube of the evaporator. After insertion, the triple-layer wire mesh extended from the upper surface of the bottom endplate of the evaporator up to end of its active heating portion. The 8-inch width of the wire mesh (chosen after several preliminary trials) creates approximately three layers of it on the inner surface of the evaporator. The cut piece of the woven wire mesh used in this technique had a mass of 41.736 g (average value of 10 measurements obtained with an electronic balance, *Acculab* VI-350), which was used to determine its volume. With this mesh inserted into the evaporator section, 83.8 ml water were needed to obtain an initial (static) fill ratio (FR) of 100 %.

3.6.6.3 Eight-disks-single-layer-wire-mesh (8DSLWM) technique

In this technique, the SLWM technique was combined with the bubble-breaker assembled with eight perforated disks. The first disk was located with its bottom surface 1-inch from the bottom end of the central threaded rod (which corresponding to the start of the active heating section); the other seven disks were located on the rod with 1-inch intervals between the circular surfaces of adjacent disks; and the eighth disk was located with its bottom circular surface located at the upper end of the active heating portion of the evaporator section. A photograph of the upper portion of this 8DSLWM arrangement is given Figure 3.19. With this 8DSLWM technique, 78 ml of water were needed to achieve a fill ratio (FR) of 100 %.

Figure 3.19 Photograph of the upper portion of the eight-disk-single-layer-wire-mesh combination before full insertion into the evaporator section of the GHP.

3.6.6.4 Ten-disks (10D) technique

In this technique, only the bubble-breaker assembled with 10 perforated disks was used inside the evaporator section of the GHP. The first disk was located with its bottom circular surface 1-inch above the end of the threaded rod (which corresponding to the start of the active heating section); the other nine disks were located on the rod with 1-inch intervals between the circular surfaces of adjacent disks (in this arrangement, the eighth disk was located with its bottom circular surface located at the upper end of the active heating portion of the evaporator section); and the bottom circular surface of the tenth disk was located 0.375 inches above the upper end 9.625-inch total inner-length of the evaporator section. The total volume of the assembled 1-disk bubble-breaker was determine by immersing it in water fill in a graduated cylinder, as shown in Figure 3.20. With this 10D technique, 78 ml of water were needed to achieve a fill ratio (FR) of 100 %.

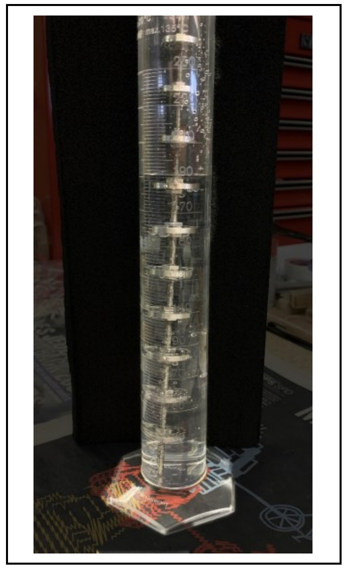

Figure 3.20 Photograph of the 10-disk bubble-breaker immersed in water contained inside a graduated cylinder (for determining the volume of this bubble-breaker).

3.6.6.5 Concluding remarks

The discussions presented in the above subsections show that the GBP in GHPs is influenced by many parameters and it could be controlled or mitigated using many different approaches and options. Even in the limited context of the two approaches considered in this work, namely, introduction of roughness on the inner surface of the core tube of the evaporator and the deployment of a bubble-breaker within the evaporator, there are many possibilities for mitigating the GBP. An investigation of all these possibilities and the identification of an optimal technique for mitigating the GBP in GHPs, or even techniques that fall within a reasonable radius of the optimal one, would require an extensive program of experiments, put together using guidance from the theory of design of experiments (DOE) [Anderson and Whitcomb (2000); Antony (2014)]. Such a program is well outside the scope of this work. The intention in this work was to only investigate the four techniques mentioned above (in Subsections 3.6.1 to 3.6.4), do some comparative assessments, and provide some guidance, if possible, along the lines of a few proof-of-concept remarks.

3.7 Supporting Instrumentation and Equipment

The thermocouples, DC power supplies, data acquisition system, an overheat-safeguard system, and constant temperature water baths used in this work are described in this section.

3.7.1 Thermocouples and their calibration

In the GHP used in this work, 10 thermocouples were used for measuring temperatures at selected locations on the outer surface of the core tube in the active-heating portion of the evaporator section; another 10 thermocouples were used for measuring temperatures at selected locations on the outer surface of the core tube in the active-cooling portion of the condenser section; two thermocouples were used to measure the cooling-water bulk temperature at the inlet and exit ports of the annular jacket of the condenser section; five thermocouples were used to record temperatures at selected locations of the vacuum circuit; and two sheathed thermocouples were inserted inside the GHP, one each through the endplates of the condenser and evaporator sections. In addition, three thermocouples (each covered with aluminum foil to minimize radiation effects) were used to measure the ambient air temperature at locations adjacent to the evaporator, adiabatic, and condenser sections. The two sheathed thermocouples were bought from *Omega* (model E-MQ-SS-125-U-6): 6-inch long, 1/8-inch diameter, SS 304 sheath, Type-E (chromel-constantan), and ungrounded. The other 31 thermocouples were fabricated in the Heat Transfer Laboratory: each was made from a 6-ft length of Teflon-coated 30-AWG Type-E wire (*Omega* TT-E-30), by spark-welding the exposed ends of the chromel and constantan wires; then the bead was coated with a high-thermal-conductivity glue (*Omegabond* 101); and the other end of the wire was attached to a miniature male connector (*Omega* SMPW-E-M).

Each of the two sheathed thermocouples was connected to a 6-ft long 24-AWG Type-E extension wire (*Omega* EXTT-E-24), attached to miniature female and male connectors at its end (*Omega* SMPW-E-F and SMPW-E-W, respectively). The far-end miniature male connectors of the 32 thermocouples were plugged into Type-E female connectors mounted in 19-inch panels (*Omega* 19MJP-2-40E) fitted on specially fabricated relay boxes; each of these female connectors was attached to a 3-ft long 24-AWG Type-E extension wire (*Omega* EXTT-E-24); and the other end of each of these extension wires was connected to the socket-pair of a selected input channel of three twenty-channel hardware-compensated relay multiplexer temperature cards (*Hewlett-Packard* Option 020) installed in a computer-controlled data acquisition/control unit (*Hewlett-Packard* 3497A).

All the thermocouples mentioned above were calibrated in-house by Boopathy (2017) using a quartz thermometer as a secondary standard (*Hewlett-Packard* 2804A; it was previously precision calibrated to an accuracy of ± 0.005 ºC over the temperature range 0 ºC to 95 ºC, using a platinum resistance thermometer, at the Physics Division of the National Research Council in Ottawa) to an accuracy of ± 0.05 ºC over the temperature range 2 ºC to 60 ºC. The procedure used for this calibration is described in Boopathy (2017), so it is not repeated here. In this work, the calibration temperature range of the 32 thermocouples was extended to go from 2 ºC to 100 ºC, to obtain increased flexibility and range in the experiments. As was mentioned earlier, 29 of these thermocouples were already installed in the GHP by Boopathy (2017), so it was not possible to remove and recalibrate them. Thus, in the temperature range of 60 ºC to 100 ºC, the calibration data provided in the work of Boopathy (2017) were supplemented by data provided by the National Institute of Standards and Technology (NIST) for Type-E high-accuracy thermocouples [Burns and Scroger (1989)]. With this approach, however, the accuracy of the measured temperatures in the range 60 ºC to 100 ºC was only ± 0.10 ºC.

3.7.2 Power supplies and related electrical circuits

In this work, four different DC power supplies were used: 1) two *Kepco* ATE 100-10M power supplies (each 0-100 V, 0-10 A) connected in series (with a suitable partitioning of their load) to power the Teflon-coated nichrome wire wrapped around the active-heating portion of the core tube of the GHP evaporator-section; 2) a single-channel *Hewlett Packard* E3612A power supply (0-60 V, 0-0.5 A; or 0-120 V, 0-0.25 A), to provide DC power to the electronic vacuum gauge; 3) a dual-channel *Xantrex* LXQ 30-2 power supply (each channel 0-30 V, 0-2 A), with one channel powering a Teflon-coated nichrome wire wrapped around a portion of the vacuum circuit adjacent to the top end-plate of the GHP condenser section, and the other channel powering a relay that was used in an overheat-protection circuit (described later in this chapter). These four DC power supplies are shown in the photographs presented in Figure 3.21.

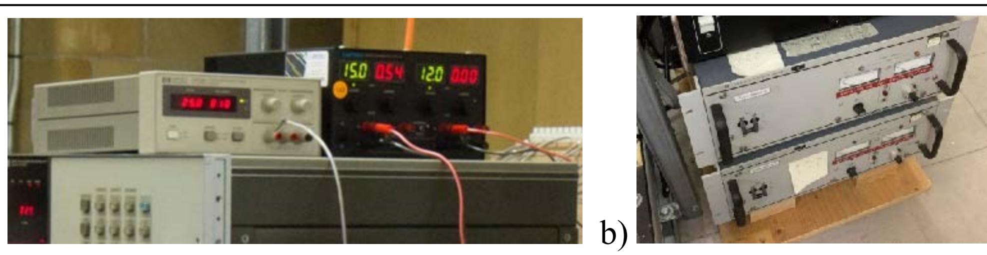

Figure 3.21 Photographs showing four DC power supplies used in this work: a) *Hewlett Packard* E3612A (left) and *Xantrex* LXQ 30-2 (right); and b) the two *Kepco* ATE 100-10M.

Some of the electrical circuits used in the overall experimental set-up are illustrated in Figure 3.22. The electrical current supplied to the nichrome wire wrapped around the active-heating portion of the core tube of the evaporator section was determined using the measured voltage drop across the terminals of a high-accuracy shunt (a 0.01Ω manganin resistor, connected in series with the nichrome wire). The resistance of this shunt remained effectively unchanged in all experiments undertaken in this work.

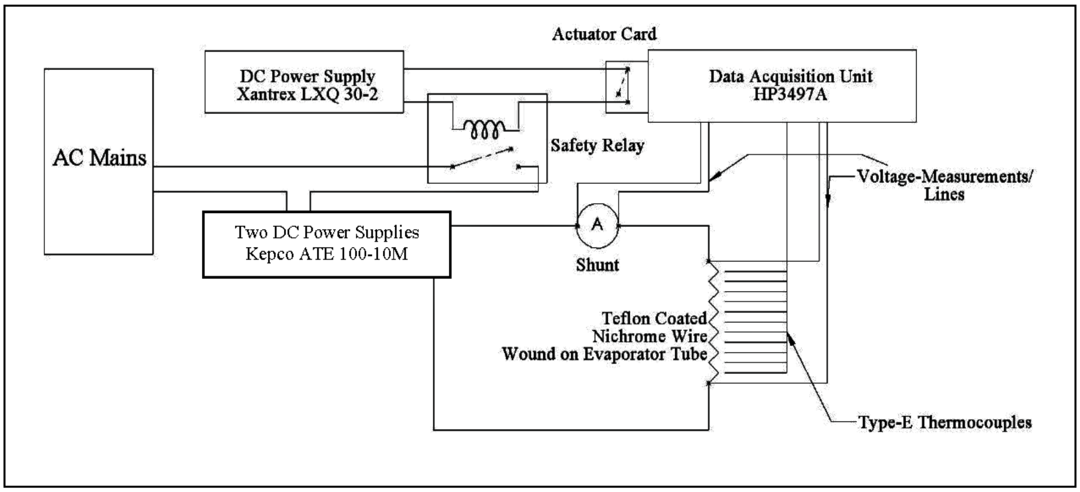

Figure 3.22 Schematic illustration of some electrical circuits used in the experimental setup [adapted from Boopathy (2017)].

3.7.3 Data acquisition and control unit

A data acquisition and control unit (*Hewlett Packard* HP3497A), fitted with three temperature-measurement multiplexer cards (20 channels each; with internal hardware compensation for Type-E thermocouples; Option 020), was used to sequentially read and store data from the 32 thermocouples employed in this work. A 20-channel voltage-measurement multiplexer card (Option 010) and a 16-channel actuator card (Option 110) were also installed in the data acquisition unit. The 20-channel voltage-measurement multiplexor card was used for the following measurements: voltage drop across the Teflon-coated nichrome wire wrapped around the active-heating portion of the core tube of the evaporator section; voltage drop across the shunt shown in Figure 3.22; and the voltage output of the electronic vacuum gauge (shown in Figures 3.9, 3.11, and 3.12). The 16-channel actuator card was used for triggering a safety relay used in an overheat-protection circuit (shown in Figure 3.22). All voltages (including those from the thermocouples) were read using a 5½-digit electronic voltmeter (DVM) integrated in the data acquisition unit (with a resolution of 1 μV and an accuracy of ±3 μV). The digitized voltage readings were transmitted to a personal computer (PC), using a GPIB interface on the data acquisition unit and a USB-GPIB interface attached to the PC, and then stored in ASCII format in specially designated files on a hard-disk in the PC, when required.

The data acquisition and control tasks were managed by a program that was run on a PC. This program was written using the National Instruments LabVIEW software and specially designed to present the data and input instructions on a virtual control panel displayed on the PC monitor screen. The output from the electronic pressure gauge was converted to mbar and presented in a window on the virtual control panel, in digital form and a dial-type icon. During the benchmarking (original) experiments (done without employing the proposed techniques for mitigating the GBP), a complete set of the data was acquired every 4.2 seconds (approximately); after these data were processed by the LabVIEW computer program, they were stored (appended) to an ASCII file, along with the corresponding time and date stamps; and thus, about 11.5 seconds were required for acquiring, processing, and storing each set of data. In addition to data and monitoring graphics, the virtual control panel also displayed indicator-lights that warned the user if some selected measured temperatures exceeded user-defined limits. A screen-capture picture of this virtual control panel displayed on the PC monitor screen is shown in Figure 3.23.

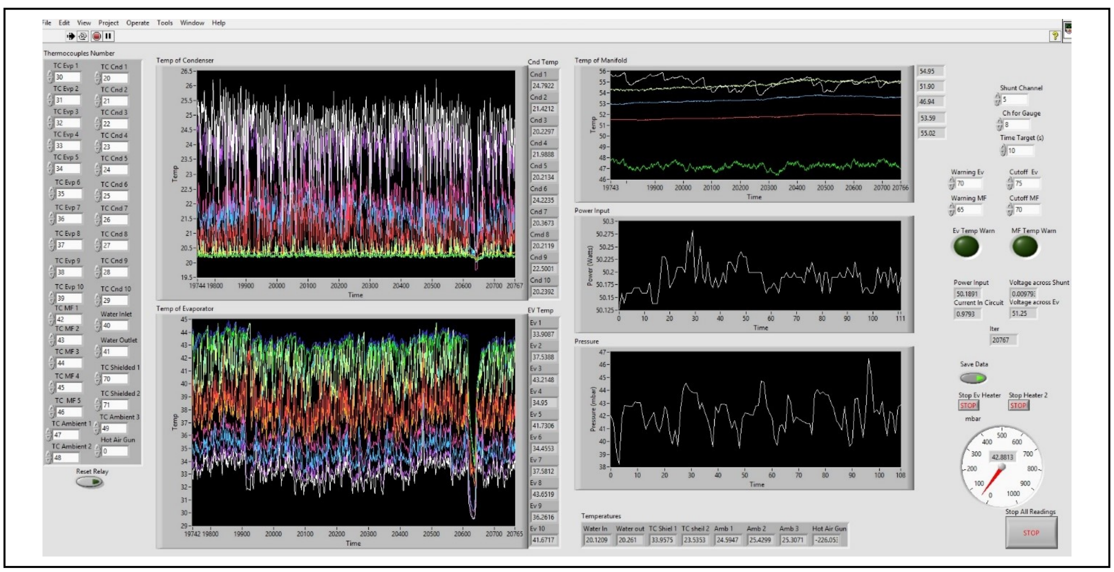

Figure 3.23 Screen-capture picture of the virtual control panel displayed by the data acquisition and control program written using the National Instruments LabVIEW software for the benchmarking (original) GHP experiments.

As was mentioned in Section 3.2, a new LabVIEW program was written and used in the experiments undertaken to assess the four techniques proposed for mitigating the GBP. With this new LabVIEW program, the data from only the 10 thermocouples attached to the outer surface of the active-heating portion of the core tube of the evaporator section were acquired, processed, and stored (some other data were acquired and displayed on the virtual control panel, but not processed and stored); and the total time needed for these tasks was only about 1 second per data set. Thus, a speed-up factor of over 10 was achieved with the new LabVIEW program, relative to the time needed for acquiring and storing each data set with the previous (old) LabVIEW program. This faster acquisition, processing, and storage of data was crucially important for reliable FFT analyses of the temperature data obtained in the experiments undertaken to assess the proposed GBP mitigation techniques. A screen-capture picture of the virtual control panel displayed on the PC monitor screen by the new LabVIEW program is shown in Figure 3.24.

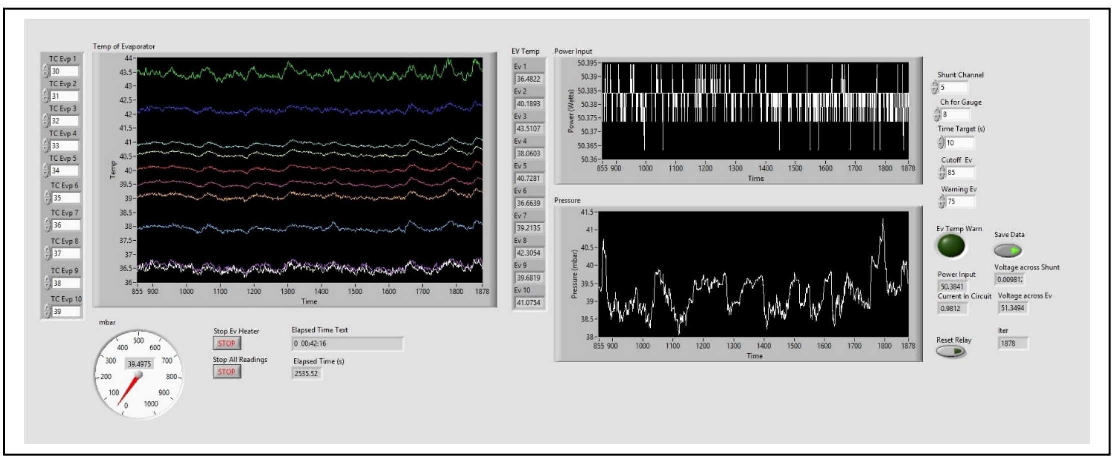

Figure 3.24 Screen-capture picture of the virtual control panel displayed by a new data acquisition and control program written using the National Instruments LabVIEW software for the GHP experiments undertaken to assess the four proposed techniques for mitigating the GBP.

3.7.4 Overheat protection

During the GHP experiments, there was the possibility that the temperatures in the evaporator section could rise to unacceptably high levels (> 80 ºC), due to dry-out conditions (or other operational limits of GHPs discussed in Chapter 1) or malfunctioning (or incorrect settings) of the main DC power supply. To prevent damage to the GHP, the 16-channel actuator card fitted inside the data acquisition/control unit (Subsection 3.7.3) and the LabVIEW computer programs were setup to activate an electro-mechanical safety relay (shown in Figure 3.22) if any of the measured temperatures exceeded the set limit. This relay was powered using one of the two channels of the *Xantrex* LXQ 30-2 DC power supply (set to 12V), and it was used to control (maintain or cut off) the power input to one of the two *Kepco* ATE 100-10M DC power supplies connected to the nichrome heating wire. The second channel of the dual-channel *Xantrex* LXQ 30-2 DC power supply was used to power the Teflon-coated nichrome wire wrapped around a portion of the vacuum circuit adjacent to the top endplate of the GHP condenser section: its voltage was adjusted to ensure that the temperatures of the related elements did not exceed 70 ºC. An indicator light (icon) was activated on the virtual control panel if any of these temperatures exceeded 70 ºC, prompting corrective action from the person conducting the GHP experiment.

3.7.5 Constant-temperature baths

In the GHP experiments, a *Neslab* RTE-211 constant-temperature bath was used to supply the cooling water to the annular jacket around the active-cooling portion of the condenser section: temperature stability of ± 0.01 ºC; maximum cooling capacity of 500 W at the 20 ºC setting; bath volume of 12.30 L; and a maximum pumping capacity of 15.20 litres per minute. The inlet and outlet ports of this bath were connected to those of the annular jacket via two 40-ft long *Neoprene* tubes (3/8-inch ID and 5/8-inch OD) each enclosed in *Armaflex* pipe insulation of 1/2-inch thickness. The bath was set to obtain cooling-water volume- and mass-flow rates through the annular jacket at effectively constant values of 63.6 ml/s and 0.0635 kg/s, respectively, at a nominal temperature of 20 ºC. Boopathy (2017) used a *Neslab* RTE-221 constant-temperature bath for calibrating the thermocouples used in this work: temperature stability of ± 0.01 °C; maximum cooling capacity of 500 W at the 20 ºC setting; bath volume of 20.5 L; and a maximum pumping capacity of 15 litres per minute. Photographs of the *Neslab* RTE 211 and RTE 221 constant-temperature baths are given in Figure 3.25.

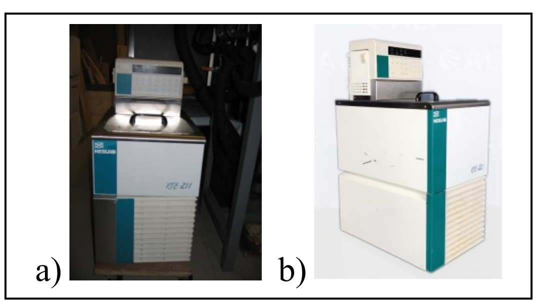

Figure 3.25 Photographs of the constant-temperature baths used in this work: a) Neslab RTE 211; and b) Neslab RTE-220.

3.8 Experimental Procedures

The procedures that were used for the following tasks are presented in this section: determination of an overall heat-loss conductance for the GHP; running the GHP experiments; and assessments of the four proposed techniques for mitigating the GBP. Details of the procedures used for conducting leak tests on the GHP and the vacuum circuit, filling the GHP, and draining the GHP were similar to those described in Boopathy (2017), so they are not repeated here.

3.8.1 Determination of an overall heat-loss conductance of the GHP

An overall heat-loss conductance, $C_{loss} [W / °C]$, was first determined by undertaking auxiliary experiments and then used to estimate the rate of heat loss, $q_{loss} \triangleq C_{loss} (\overline{T}_{evap}^{wall} - \overline{T}_{\infty})$, from the GHP to the ambient environment in each of the final experiments. The procedure that was used to determine this overall heat-loss conductance of the GHP is presented in pointwise form below:

1. Switch on the power supplies, the data acquisition system, the electronic vacuum gauge, the personal computer, and the monitor. Start the LabVIEW program written for data acquisition and control for the benchmarking experiments. Turn on the cooling-water flow to the condenser section of the GHP. Leave all these systems turned on and running for at least two hours (to allow them to stabilize and achieve reliable operating conditions).
2. Drain any remaining working fluid in the GHP. Close the shutoff valves in the filling circuit. Evacuate the GHP to a vacuum level of 0.1 mbar or less, close the plug valves between the vacuum pump and the vacuum circuit, and then shut off the vacuum pump.
3. Turn on the power supply to the active-heating portion of the evaporator section of the GHP; and then adjust its output voltage to get the desired average wall temperature in the evaporator section (start with 40 ºC, nominal).
4. Maintain the condition described in previous step for at least six hours, so that the temperatures in the evaporator section reach a steady value. Then record all data (power input; all temperatures; and readings from the electronic vacuum gauge). Record the data for approximately 30 mins (to acquire, process, and store at least 100 sets of data points). The LabVIEW program saves this data in a specially created ASCII file. Copy the data from this ASCII file into another appropriately labelled data file, for further processing later, and clear the original ASCII file for accepting data from the next run.

5. Increase the power input to achieve the next desired average wall temperature in the evaporator section. Then repeat steps 3 and 4. Continue this procedure until the runs for average wall temperatures of 40 ºC, 50 ºC, and 60 ºC (nominal) have all been covered.
6. Shut off the power input to the active-heating portion of the evaporator section and allow all wall temperatures in this section to cool down to below 40 ºC. Then repeat steps 3 – 5, to obtain data that would serve as repeatability checks.

In these experiments, as there is no working fluid in the GHP, all power supplied to the active portion of the evaporator section is essentially lost to the ambient air. The recorded data for each of the chosen values of the power input can be used to obtain the corresponding values of the total rate of heat input, $q_{in,total,vacuum\ conditions\ in\ GHP}$, the spatial- and time-averaged evaporator-tube wall temperature, $\overline{T}_{evap}^{wall}$, and the spatial- and time-averaged ambient temperature, $\overline{T}_{\infty}$. These data were used to calculate the overall heat loss conductance, C_{loss}, as follows:

$$C_{loss} \triangleq (q_{in,total,vacuum\_conditions\_in\_GHP}) / (\overline{T}_{evap}^{wall} - \overline{T}_{\infty}) \tag{3.3}$$

The corresponding experimental data and results are summarized in Table 3.1. The arithmetic-mean and (± standard deviation × 2) of these values were used to obtain the following expression [Taylor and Kuyatt (1994); ASME Standard PTC (2005)]: C_{loss} = 0.0804 ± 0.0021 W/ºC.

Table 3.1 Data and results obtained from the auxiliary experiments that were conducted to determine an overall heat-loss conductance of the GHP.

$q_{in,total,vacuum\_conditions\_in\_GHP}$ $[W]$	$\overline{T}_{evap}^{wall}$ $[°C]$	$\overline{T}_{\infty}$ $[°C]$	C_{loss} $[W/°C]$
1.42	42.63	24.57	0.0788
1.42	41.79	23.78	0.0790
1.42	41.63	24.10	0.0811
1.80	46.98	24.36	0.0794
1.80	45.92	23.59	0.0804
1.80	46.12	23.81	0.0805
2.22	51.33	24.26	0.0820
2.22	51.30	24.12	0.0816
2.22	50.44	23.07	0.0810
		Arithmetic-mean value of C_{loss}	**0.0804**

3.8.2 GHP experiments

The following procedure was used to run the GHP experiments (including those undertaken to assess the GBP mitigation techniques), acquire the related data, and store it appropriately:

1. With the GHP prepared for the experiment with the chosen fill ratio, switch on the power supplies, the data acquisition system, and the electronic vacuum gauge. Switch on the personal computer and monitor; and start the LabVIEW program written for data acquisition and control. Turn on the cooling-water flow to the condenser section of the GHP and set the corresponding water-bath temperature to 20 ºC. Also ensure that the blower and the rest of the arrangement for heating the vacuum circuit and the vacuum gauges (Figure 3.9) are turned on and appropriately adjusted in accordance with the discussions given in Section 3.4. Leave all these systems turned on and running for at least two hours (to allow them to stabilize and achieve reliable operating conditions).
2. Slowly increase power input to the active-heating portion of the evaporator section to the desired level (start with 50 W, nominal), by increasing the voltage applied by the DC power supply across the Teflon-coated nichrome wire wrapped around the core tube of this section. Then wait (≥ two hours) until all monitored temperatures show effectively steady-state values or display essentially cyclical behavior (characteristic of the GBP).
3. Click the "Save Data" button on the virtual control panel displayed on the computer monitor. Record the data for approximately 30 mins (to obtain at least 100 sets of data). The LabVIEW program saves this data in a specially created ASCII file. After this task has been fully completed, copy the data from this ASCII file into another appropriately labelled data file, for further processing later. Then clear the original ASCII file to prepare it for accepting data from the next experimental run
4. Remove the insulation from the flow-visualization segment of the adiabatic section of the GHP (the insulation over this flow-visualization segment was designed to allow easy removal and reinstallation) and film the fluid-flow phenomena (in this work, a high-definition (HD) video camera was used; it was supported on a sturdy tripod located at a fixed spot, to ensure stability of the camera and repeatability of the filmed region).
5. Repeat steps 3 to 4 with the next desired level of power input to the active heating section. Do this for power inputs of 50 W, 100 W, 150 W, 200 W, 250 W, and 300 W (nominal).

6. Once the runs are completed for all desired power levels, change the fill ratio to the next desired value (100 %, 150 %, or 175 %) and repeat the steps 2-5. Repeat steps 1-6 for all repeatability runs.
7. Drain the GHP and allow it to dry fully by keeping the vacuum pump switched on (in the gas ballast mode) for at least 12 hours.
8. In the experimental runs with the techniques for mitigating the GBP, disconnect the adiabatic section from the GHP to allow the insertion in the evaporator section of either the woven wire mesh, the bubble-breaker, or a combination of these elements, as needed. Do this task gently and with special care to ensure that there is no damage to the adiabatic section and the rest of the GHP.
9. Once Step 8 is completed, insert the appropriate elements of the GBP mitigation technique in the evaporator section and then reconnect the adiabatic section to the GHP. Do these tasks gently and with special care to ensure that there is no damage to the adiabatic section, the elements of the mitigation technique, and the rest of the GHP.
10. Repeat steps 1-9 until the experimental runs with all four GBP mitigation techniques have been fully completed. Use the new LabVIEW computer program in all experimental runs done with the GBP mitigation techniques and in the corresponding benchmarking runs.

3.8.3 Assessment of the four proposed techniques for mitigating geyser boiling

The experiments that were undertaken for assessing the four proposed techniques for mitigating the GBP in the GHP were done with three fill ratios (FR = 100 %, 150 %, and 175 %,) and six total power inputs ($q_{in,total}$ = 50 W, 100 W, 150 W, 200 W, 250 W, and 300 W), whenever possible (that is, when all 10 thermocouples attached to the outer surface of the core tube of the evaporator section satisfied the prescribed safety requirement: $T_{evap}^{wall} \leq 80$ ºC).

Graphical presentations of the measured (T_{evap}^{wall} vs t) data and the video recordings of the fluid-flow phenomena in the flow-visualization segment of the adiabatic section of the GHP were used to obtain a good qualitative feel for the nature of the GBP. In addition, in this work, to obtain a quantitative assessment of the four proposed techniques to mitigate the GBP, the Fast-Fourier-Transform (FFT) technique [Ramirez (1985)] was adopted for analyses of the (T_{evap}^{wall} vs t) data. This appears to be the first use of the FFT technique for analyses of data related to the GBP in a single-tube GHP; however, in a recent work [Elkholy and Kemper (2020)], the FFT technique was used to analyze the pressure signal corresponding to the GBP in a two-phase *loop* thermosyphon.

Preliminary experiments showed that the (T_{evap}^{wall} vs t) data obtained from the eighth of the 10 thermocouples deployed on the core tube of the evaporator section displayed either the highest or close to the highest values of the amplitude of the time-oscillations ($|(T-T_{av})_{evap}^{wall}|$; where $T_{av,evap}^{wall}$ is the time-average value of T_{evap}^{wall}) during conditions corresponding to the GBP. This eighth thermocouple (denoted as Ev8 in this thesis) was located 2-inch above the start of the active-heating portion of the evaporator section. Thus, the $(T-T_{av})_{Ev8}$ vs t data were chosen for the FFT analyses. They were done using a special computer program (written using MATLAB R2018a) for FFT analyses of digital data in which the sampling times are not uniform [Ramirez (1985)].

The data used in the FFT analyses were obtained using the previously mentioned new LabVIEW data acquisition program. With it, each set of 10 T_{evap}^{wall} values could be acquired and recorded in an average timespan of 1 second, so the sampling rate was 1 Hz. In contrast, the previous (old) data-acquisition program provided an average sampling of 0.087 Hz. The faster sampling rate provided by the new program allowed the FFT analyses to reveal more events/peaks in the acquired data. A comparison of the FFT analyses of the data obtained with the new and old data acquisition programs for an experiment done with the 8DSLMW technique (described in Subsection 3.6.6.3) is provided below in Figure 3.26 (*all* results are presented in Chapter 4).

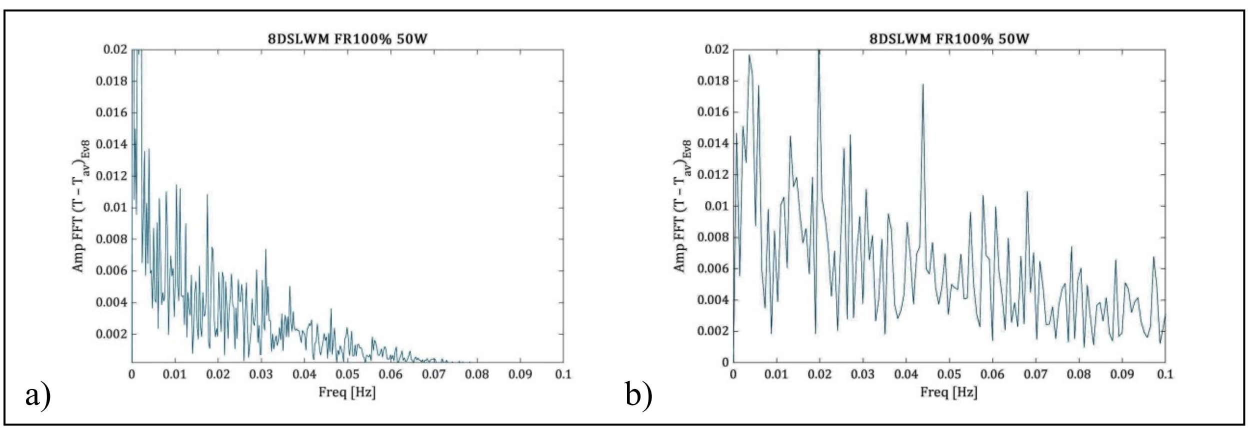

Figure 3.26 Plots of the FFT analyses for an experiment with 8DSLWM (FR 100 %, and 50 W) using data obtained with a) the old LabVIEW program; and b) the new LabVIEW program.

Chapter 4: Results and Discussion

The results obtained with the GHP, the supporting setup, and the procedures discussed in Chapter 3 are presented and discussed in the following sections of this chapter: 1) preliminary experiments, repeatability runs, and results; 2) benchmarking experiments and results; and 3) experiments with the proposed techniques for mitigating geyser boiling in the GHP, results, and assessment.

4.1 Preliminary Experiments, Repeatability Runs, and Results

After the refurbishment and improvements of a GHP and the supporting experimental setup designed and implemented by Boopathy (2017), as was described in Chapter 3, many tests of the overall experiment setup were conducted to ensure that it was functioning properly. After these tests, 15 preliminary runs were undertaken to gain further familiarity with the overall experimental setup and procedures. Then, 15 additional runs were done to establish the repeatability of the preliminary runs. These 15 additional runs are referred to in this thesis as 'repeatability' runs.

4.1.1 Overview

The experimental settings, conditions, and results for the 15 preliminary runs, labelled as Runs # 1 to 15, are summarized in Table 4.1 (given on the next page) and discussed in Subsections 4.1.2 to 4.1.6. It is worth noting here that Runs # 1 to 10 were similar to those done originally by Boopathy (2017), and his results and those obtained in this work compared well. The experimental settings, conditions, and results of the 15 repeatability runs, labelled as Runs # 1R to 15R, are summarized and compared with those of the preliminary runs in Tables 4.2 and 4.3: Runs # 1 to 8 and 1R to 8R in Tables 4.2 (given on 74); and Runs # 9 to 15 and 9R to 15R in Table 4.3 (75).

With reference to the discussions in Chapter 3, the maximum uncertainties in the experimental measurements were as follows: ± 0.05 ºC and ± 0.10 ºC in the temperature measurements in the ranges 2 ºC to 60 ºC and 60 ºC to 100 ºC, respectively; ± 0.5 % of reading or 0.50 mbar in the vapor-pressure measurements in the condenser section; ± 3.0 μV in the voltage measurements; ± 1.0 mA in the current measurements; ± 0.115 W in the total rate of heat input; and 0.0021 W/ºC in the value of the overall heat-loss conductance (C_{loss} = 0.0804 ± 0.0021 W/ºC). The repeatability of some the results that are based on many of these measurements is discussed Subsection 4.1.7.

Table 4.1 Experimental settings, conditions, and results for preliminary runs 1 to 15.

Settings and Conditions									Results								
Run #	FR [%]	$q_{in,tot}$ [W]	Current [A]	Voltage [V]	T_{WB} [°C]	$T_{\infty,evap}$ [°C]	$T_{\infty,adiab}$ [°C]	$T_{\infty,cond}$ [°C]	q_{loss} [W]	q_{in} [W]	$\overline{T}^{wall}_{evap}$ [°C]	$\overline{T}^{water}_{evap}$ [°C]	$\overline{T}^{wall}_{cond}$ [°C]	$\overline{T}^{vapor}_{cond}$ [°C]	$\overline{P}^{vapor}_{cond}$ [mbar]	C_{GHP} [W/°C]	Boiling in evap
1		50.46	0.982	51.386	20.14	24.77	25.34	24.88	1.082	49.37	38.45	33.75	21.43	22.80	42.69	2.901	Geyser
2		100.70	1.387	72.600	20.13	25.49	24.62	24.44	1.509	99.19	43.62	37.09	22.59	27.24	55.35	4.717	Geyser
3	100	150.37	1.695	88.719	20.12	25.14	24.52	25.32	1.794	148.57	47.31	39.25	23.44	32.79	63.63	6.224	Nucleate
4		200.73	1.958	102.51	20.10	25.03	25.28	25.98	2.077	198.66	51.26	41.19	24.36	36.81	70.36	7.385	Nucleate
5		250.40	2.187	114.49	20.84	25.94	25.88	26.03	2.346	248.05	55.13	42.99	25.78	39.57	76.57	8.452	Nucleate
6		49.77	0.975	51.035	20.14	24.51	24.74	25.16	1.655	48.11	45.39	40.93	21.40	22.52	57.35	2.006	Geyser
7		100.36	1.385	72.475	20.14	25.40	24.63	24.73	1.733	98.62	46.47	40.25	22.56	28.49	57.87	4.125	Geyser
8	150	150.67	1.697	88.808	20.13	26.19	24.82	25.13	1.971	148.70	49.90	42.16	23.37	32.44	66.01	5.605	Nucleate
9		200.47	1.957	102.44	20.11	26.27	24.83	25.12	2.345	198.12	54.57	44.95	24.20	35.67	77.30	6.524	Nucleate
10		250.49	2.187	114.52	20.69	27.33	25.80	25.91	2.682	247.81	59.71	47.88	25.48	38.40	91.36	7.239	Nucleate
11		50.31	0.981	51.313	20.13	25.55	24.94	25.25	1.829	48.48	48.00	43.27	21.43	22.36	57.72	1.825	Geyser
12		100.41	1.385	72.496	20.14	25.84	24.48	24.58	2.049	98.36	50.45	44.08	22.84	27.37	67.49	3.563	Geyser
13	175	150.16	1.694	88.656	20.13	25.21	24.22	24.62	2.246	147.91	52.62	44.93	23.66	33.55	73.13	5.107	Nucleate
14		200.06	1.955	102.34	20.14	25.17	24.34	25.02	2.737	197.32	58.88	49.30	24.70	37.55	95.58	5.773	Nucleate
15		220.04	2.050	107.33	20.14	26.50	25.27	26.38	2.768	217.28	60.48	50.01	24.97	38.33	98.54	6.119	Nucleate

Table 4.2 Experimental settings, conditions, and results for repeatability runs 1R to 8R.

Settings and Conditions									Results							
Run #	FR [%]	$q_{in,tot}$ [W]	Current [A]	Voltage [V]	T_{WB} [ºC]	$T_{\infty,evap}$ [ºC]	$T_{\infty,adiab}$ [ºC]	$T_{\infty,cond}$ [ºC]	q_{loss} [W]	q_{in} [W]	$\overline{T}_{evap}^{wall}$ [ºC]	$\overline{T}_{evap}^{water}$ [ºC]	$\overline{T}_{cond}^{wall}$ [ºC]	$\overline{T}_{cond}^{vapor}$ [ºC]	$\overline{P}_{cond}^{vapor}$ [mbar]	C_{GHP} [W/ºC]
1	100	50.46	0.982	51.386	20.14	24.77	25.34	24.88	1.082	49.37	38.45	33.75	21.43	22.80	42.69	2.901
1R		50.16	0.979	51.234	20.14	25.17	24.64	24.41	1.067	49.09	38.01	33.42	21.45	22.98	42.35	2.964
Mean values									1.0745	49.23	38.23	33.59	21.44	22.89	42.52	2.933
Absolute differences about mean									0.0075	0.14	0.22	0.16	0.01	0.09	0.17	0.031
Absolute % differences about mean									**0.70**	**0.28**	**0.58**	**0.49**	**0.05**	**0.39**	**0.40**	**1.07**
2	100	100.70	1.387	72.600	20.13	25.49	24.62	24.44	1.509	99.19	43.62	37.09	22.59	27.24	55.35	4.717
2R		100.95	1.389	72.689	20.12	25.34	24.66	24.37	1.502	99.45	43.47	36.76	22.55	27.07	54.54	4.754
Mean values									1.5055	99.32	43.55	36.93	22.57	27.16	54.95	4.736
Absolute differences about mean									0.0035	0.13	0.07	0.17	0.02	0.08	0.41	0.019
Absolute % differences about mean									**0.23**	**0.13**	**0.17**	**0.45**	**0.09**	**0.31**	**0.74**	**0.39**
3	100	150.37	1.695	88.719	20.12	25.14	24.52	25.32	1.794	148.57	47.31	39.25	23.44	32.79	63.63	6.224
3R		150.03	1.693	88.619	20.12	25.50	24.59	24.71	1.799	148.23	47.31	39.08	23.51	33.07	62.97	6.228
Mean values									1.7965	148.40	47.31	39.17	23.48	32.93	63.30	6.226
Absolute differences about mean									0.0025	0.17	0.00	0.09	0.04	0.14	0.33	0.002
Absolute % differences about mean									**0.14**	**0.11**	**0.00**	**0.22**	**0.15**	**0.43**	**0.52**	**0.03**
4	100	200.73	1.958	102.51	20.10	25.03	25.28	25.98	2.077	198.66	51.26	41.19	24.36	36.81	70.36	7.385
4R		200.49	1.957	102.45	20.12	25.23	24.93	24.82	2.136	198.35	51.56	41.60	24.41	37.16	71.73	7.306
Mean values									2.1065	198.51	51.41	41.40	24.39	36.99	71.05	7.346
Absolute differences about mean									0.0295	0.16	0.15	0.20	0.02	0.17	0.69	0.040
Absolute % differences about mean									**1.40**	**0.08**	**0.29**	**0.50**	**0.10**	**0.47**	**0.96**	**0.54**
5	100	250.40	2.187	114.49	20.84	25.94	25.88	26.03	2.346	248.05	55.13	42.99	25.78	39.57	76.57	8.452
5R		250.17	2.186	114.44	20.60	25.99	25.79	25.80	2.328	247.84	54.81	42.84	25.48	38.89	75.9	8.45
Mean values									2.3370	247.95	54.97	42.92	25.63	39.23	76.24	8.451
Absolute differences about mean									0.0090	0.11	0.16	0.07	0.15	0.34	0.33	0.001
Absolute % differences about mean									**0.39**	**0.04**	**0.29**	**0.17**	**0.59**	**0.87**	**0.44**	**0.01**
6	150	49.77	0.975	51.035	20.14	24.51	24.74	25.16	1.655	48.11	45.39	40.93	21.4	22.52	57.35	2.006
6R		50.55	0.983	51.433	20.14	24.80	24.66	24.80	1.693	48.86	45.81	41.12	21.58	23.31	57.48	2.016
Mean values									1.6740	48.49	45.60	41.03	21.49	22.92	57.42	2.011
Absolute differences about mean									0.0189	0.38	0.21	0.09	0.09	0.40	0.06	0.005
Absolute % differences about mean									**1.13**	**0.77**	**0.46**	**0.23**	**0.42**	**1.72**	**0.11**	**0.25**
7	150	100.36	1.385	72.475	20.14	25.40	24.63	24.73	1.733	98.62	46.47	40.25	22.56	28.49	57.87	4.125
7R		100.38	1.385	72.485	20.13	25.33	24.66	24.85	1.764	98.62	46.89	40.65	22.56	27.96	59.62	4.053
Mean values									1.7485	98.62	46.68	40.45	22.56	28.23	58.75	4.089
Absolute differences about mean									0.0155	0.00	0.21	0.20	0.00	0.26	0.88	0.036
Absolute % difference about mean									**0.89**	**0.00**	**0.45**	**0.49**	**0.00**	**0.94**	**1.49**	**0.88**
8	150	150.67	1.697	88.808	20.13	26.19	24.82	25.13	1.971	148.7	49.9	42.16	23.37	32.44	66.01	5.605
8R		150.65	1.697	88.802	20.14	25.91	24.85	24.77	1.977	148.68	49.77	42.11	23.39	32.49	65.8	5.636
Mean values									1.9740	148.69	49.84	42.14	23.38	32.47	65.91	5.621
Absolute differences about mean									0.0030	0.01	0.06	0.02	0.01	0.03	0.11	0.015
Absolute % differences about mean									**0.15**	**0.01**	**0.13**	**0.06**	**0.04**	**0.08**	**0.16**	**0.28**

Table 4.3 Experimental settings, conditions, and results for repeatability runs 9R to 15R.

Settings and Conditions									Results							
Run #	*FR* [%]	$q_{in,tot}$ [W]	Current [A]	Voltage [V]	T_{WB} [ºC]	$T_{\infty,evap}$ [ºC]	$T_{\infty,adiab}$ [ºC]	$T_{\infty,cond}$ [ºC]	q_{loss} [W]	q_{in} [W]	$\overline{T}_{evap}^{wall}$ [ºC]	$\overline{T}_{evap}^{water}$ [ºC]	$\overline{T}_{cond}^{wall}$ [ºC]	$\overline{T}_{cond}^{vapor}$ [ºC]	$\overline{P}_{cond}^{vapor}$ [mbar]	C_{GHP} [W/ºC]
9	150	200.47	1.957	102.44	20.11	26.27	24.83	25.12	2.345	198.12	54.57	44.95	24.2	35.67	77.3	6.524
9R		200.61	1.958	102.48	20.13	25.37	24.79	25.14	2.353	198.26	54.36	44.81	24.19	35.67	76.2	6.571
Mean values									2.3490	198.19	54.47	44.88	24.20	35.67	76.75	6.548
Absolute differences about mean									0.0040	0.07	0.10	0.07	0.00	0.00	0.55	0.023
Absolute % differences about mean									**0.17**	**0.04**	**0.19**	**0.16**	**0.02**	**0.00**	**0.72**	**0.36**
10	150	250.49	2.187	114.52	20.69	27.33	25.80	25.91	2.682	247.81	59.71	47.88	25.48	38.4	91.36	7.239
10R		250.35	2.187	114.49	20.40	27.33	25.78	25.85	2.684	247.67	59.7	47.88	25.2	38.15	91.49	7.179
Mean values									2.6830	247.74	59.71	47.88	25.34	38.28	91.43	7.209
Absolute differences about mean									0.0010	0.07	0.01	0.00	0.14	0.13	0.06	0.030
Absolute % difference about mean									**0.04**	**0.03**	**0.01**	**0.00**	**0.55**	**0.33**	**0.07**	**0.42**
11	175	50.31	0.981	51.313	20.13	25.55	24.94	25.25	1.829	48.48	48	43.27	21.43	22.36	57.72	1.825
11R		50.73	0.985	51.527	20.15	24.91	24.78	25.22	1.847	48.89	47.94	43.37	21.5	22.96	59.32	1.849
Mean values									1.8380	48.69	47.97	43.32	21.47	22.66	58.52	1.837
Absolute differences about mean									0.0090	0.21	0.03	0.05	0.04	0.30	0.80	0.012
Absolute % differences about mean									**0.49**	**0.42**	**0.06**	**0.12**	**0.16**	**1.32**	**1.37**	**0.65**
12	175	100.41	1.3851	72.496	20.14	25.84	24.48	24.58	2.049	98.36	50.45	44.08	22.84	27.37	67.49	3.563
12R		100.36	1.3847	72.475	20.14	24.67	24.33	24.74	2.094	98.26	50.62	44.13	22.66	25.53	67.84	3.514
Mean values									2.0715	98.31	50.54	44.11	22.75	26.45	67.67	3.539
Absolute differences about mean									0.0225	0.05	0.08	0.03	0.09	0.92	0.17	0.025
Absolute % difference about mean									**1.09**	**0.05**	**0.17**	**0.06**	**0.40**	**3.48**	**0.26**	**0.69**
13	175	150.16	1.694	88.656	20.13	25.21	24.22	24.62	2.246	147.91	52.62	44.93	23.66	33.55	73.13	5.107
13R		149.85	1.692	88.567	20.12	25.00	24.23	24.58	2.261	147.59	52.73	44.93	23.64	33.4	73.22	5.074
Mean values									2.2535	147.75	52.68	44.93	23.65	33.48	73.18	5.091
Absolute differences about mean									0.0075	0.16	0.05	0.00	0.01	0.08	0.05	0.016
Absolute % differences about mean									**0.33**	**0.11**	**0.10**	**0.00**	**0.04**	**0.22**	**0.06**	**0.32**
14	175	200.06	1.955	102.34	20.14	25.17	24.34	25.02	2.737	197.32	58.88	49.30	24.70	37.55	95.58	5.773
14R		200.67	1.958	102.49	20.13	25.87	24.290	24.88	2.708	197.96	58.69	49.04	24.63	37.38	94.61	5.812
Mean values									2.7225	197.64	58.79	49.17	24.67	37.47	95.10	5.793
Absolute differences about mean									0.0145	0.32	0.10	0.13	0.04	0.08	0.48	0.020
Absolute % differences about mean									**0.53**	**0.16**	**0.16**	**0.26**	**0.14**	**0.23**	**0.51**	**0.34**
15	175	220.04	2.050	107.33	20.14	26.50	25.27	26.38	2.768	217.28	60.48	50.01	24.97	38.33	98.54	6.119
15R		219.64	2.048	107.23	20.14	25.32	24.85	25.35	2.845	216.79	60.56	50.11	24.92	38.47	99.62	6.083
Mean values									2.8065	217.04	60.52	50.06	24.95	38.40	99.08	6.101
Absolute differences about mean									0.0385	0.25	0.04	0.05	0.02	0.07	0.54	0.018
Absolute % differences about mean									**1.37**	**0.11**	**0.07**	**0.10**	**0.10**	**0.18**	**0.55**	**0.30**

In the columns of Tables 4.1 to 4.3 pertaining to the experimental settings and conditions, $q_{in,tot}$ is the total rate of heat input to the evaporator section (= Voltage $\times$ Current); and the set-temperature of the constant-temperature refrigerated/recirculating water bath, T_{WB}, and the ambient temperatures adjacent to the evaporator, adiabatic, and condenser sections of the GHP, $T_{\infty,evap}$, $T_{\infty,adiab}$, and $T_{\infty,cond}$, respectively, all denote time-averaged values. In the columns of these tables pertaining to the results, $\overline{T}_{evap}^{wall}$ and $\overline{T}_{cond}^{wall}$ denote spatial- *and* time-averaged values of the wall temperatures in the evaporator and condenser sections, respectively; $\overline{T}_{evap}^{water}$ and $\overline{T}_{cond}^{vapor}$ denote time-averaged values of the water and vapor temperatures in the evaporator and condenser sections, respectively; $\overline{P}_{cond}^{vapor}$ denotes time-averaged values of the vapor pressure in the condenser section; q_{loss} is the rate of heat loss from the evaporator to the ambient air; $q_{in} = (q_{in,tot} - q_{loss})$ is the actual rate of heat input to the evaporator; $C_{GHP} \triangleq q_{in} / (\overline{T}_{evap}^{wall} - \overline{T}_{cond}^{wall})$ is the overall thermal conductance of the GHP; and 'Boiling in evap' indicates the boiling regime encountered in the evaporator for the corresponding settings and conditions. The entries in the results columns of these tables are discussed further in the subsections that follow the next paragraph.

With respect to the settings and conditions given in Tables 4.1 to 4.3, it should be noted that for fill-ratio values of *FR* = 100 % and 150 %, the reported *nominal* values of the total rate of heat input to the evaporator section, $q_{in,tot}$, are in the range 50 W $\leq q_{in,tot} \leq$ 250 W, as they could be used in the experiments without any difficulties. However, for *FR* = 175 %, the reported *nominal* values of $q_{in,tot}$, are in a range that is slightly smaller, 50 W $\leq q_{in,tot} \leq$ 220 W. This is because when values of $q_{in,tot} >$ 220 W were used in the experiments with *FR* = 175 %, the safety cut-off temperature (set at 75 ºC) was exceeded by one of the measured wall temperatures in the evaporator section, T_{evap}^{wall}. The reason for this limitation is that the overall conductance of the GHP, C_{GHP}, decreases with increasing values of *FR* (for *FR* = 100 %, 150 %, and 175 %); and for FR = 175 %, the relatively low value of C_{GHP} caused one of the T_{evap}^{wall} values to exceed the cut-off temperature of 75 ºC for values of $q_{in,tot} >$ 220 W. Additional discussions of these and other related points are provided in the subsequent subsections of this section.

4.1.2 Rates of heat loss from and heat input to the evaporator

In the results columns of Tables 4.1 to 4.3, the values of the rate of heat loss from the evaporator, q_{loss}, and the rate of heat input to it, q_{in}, were calculated for each experimental run using the values of $\bar{T}_{evap}^{wall}$, the average ambient temperature, $\bar{T}_{\infty} = (T_{\infty,evap} + T_{\infty,adiab} + T_{\infty,cond})/3$, the total rate of heat input to the evaporator, $q_{in,tot}$, and the mean value of the overall heat-loss conductance of the GHP, $C_{loss} = 0.0804$ W/ºC (discussed in Subsection 3.8.1), in the following equations: $q_{loss} = C_{loss}(\bar{T}_{evap}^{wall} - \bar{T}_{\infty})$; and $q_{in} = q_{in.tot} - q_{loss}$. The values of q_{loss} and q_{in} for the preliminary runs are presented in Table 4.1: for Runs # 1 to 5 (*FR* = 100 %), they range from 1.082 W to 2.346 W and 49.37 W to 248.05 W, respectively; for Runs # 6 to 10 (*FR* = 150 %), they range from 1.655 W to 2.682 W and 48.11 W to 247.81 W, respectively; and for Runs # 11 to 15 (*FR* = 175 %), they range from 1.829 W to 2.768 W and 48.48 W to 217.28 W, respectively. In all cases, q_{loss} was always less than 3.8 % of q_{in}. These results for the repeatability runs were very similar (runs 1R to 8R are presented in Table 4.2; and runs 9R to 15R are presented in Table 4.3).

4.1.3 Average tube-wall and water temperatures in the evaporator

The values of spatial- *and* time-averaged tube-wall temperature, $\bar{T}_{evap}^{wall}$, and time-averaged water temperature, $\bar{T}_{evap}^{water}$, in the evaporator section for the preliminary runs are presented in Table 4.1: for Runs # 1 to 5 (*FR* = 100 %), they range from 38.45 ºC to 55.13 ºC and 33.75 ºC to 42.99 ºC, respectively; for Runs # 6 to 10 (*FR* = 150 %), they range from 45.39 ºC to 59.71 ºC and 40.93 ºC to 47.88 ºC, respectively; and for Runs # 11 to 15 (*FR* = 175 %), they range from 48.00 ºC to 60.48 ºC and 43.27 ºC to 50.01 ºC, respectively. As was expected, for each value *FR*, the values of $\bar{T}_{evap}^{wall}$ are higher for higher values of $q_{in.tot}$. It should be noted that for similar values of $q_{in.tot}$, the values of $\bar{T}_{evap}^{wall}$ are higher for higher values of *FR*. These results were also expected, as the height of the liquid water pool inside the evaporator increases with increasing values of *FR*; thus, because of the related hydrostatic effect, the values of pressure at the bottom of the evaporator are higher for higher values of *FR*; and this, in turn, leads to higher values of $\bar{T}_{evap}^{water}$ (and $\bar{T}_{evap}^{wall}$) for higher values of *FR* for each value of $q_{in.tot}$. These results for the repeatability runs were very similar (runs 1R to 8R are presented in Table 4.2; and runs 9R to 15R are presented in Table 4.3).

4.1.4 Average tube-wall and vapor temperatures and pressure in the condenser

The values of the spatial- *and* time-averaged tube-wall temperature, $\overline{T}_{cond}^{wall}$, the time-averaged vapor temperature, $\overline{T}_{cond}^{vapor}$, and the time-averaged vapor pressure, $\overline{P}_{cond}^{vapor}$, in the condenser section for the preliminary runs are given in Table 4.1: for Runs # 1 to 5 (*FR* = 100 %), they range from 21.43 °C to 25.78 °C, 22.80 °C to 39.57 °C, and 42.69 mbar to 76.57 mbar, respectively; for Runs # 6 to 10 (*FR* = 150 %), they range from 21.40 °C to 25.48 °C, 22.52 °C to 38.40 °C, and 57.35 mbar to 91.36 mbar, respectively; and for Runs # 11 to 15 (*FR* = 175 %), they range from 21.43 °C to 24.97 °C, 22.36 °C to 38.33 °C, and 57.72 mbar to 98.54 mbar, respectively. These results for the repeatability runs were very similar (runs 1R to 8R are presented in Table 4.2; and runs 9R to 15R are presented in Table 4.3).

Again, as was expected, for each value of the fill ratio (*FR*), the values of $\overline{T}_{cond}^{wall}$, $\overline{T}_{cond}^{vapor}$, and $\overline{P}_{cond}^{vapor}$ are lowest at the lowest values of $q_{in,tot}$; and their highest values correspond to the highest values of $q_{in,tot}$.

4.1.5 Overall conductance of the GHP

The overall conductance (which is the inverse of the resistance) of the GHP, C_{GHP}, is defined in the equation below (it is the same definition as that given earlier in in the text on 76):

$$C_{GHP} \triangleq q_{in} / (\overline{T}_{evap}^{wall} - \overline{T}_{cond}^{wall}) \tag{4.1}$$

The values of C_{GHP} for the preliminary runs are presented in Table 4.1: for Runs # 1 to 5 (*FR* = 100 %), they range from 2.901 W/°C to 8.452 W/°C; for Runs # 6 to 10 (*FR* = 150 %), they range from 2.006 W/°C to 7.239 W/°C; and for Runs # 11 to 15 (*FR* = 175 %), they range from 1.825 W/°C to 6.119 W/°C. In contrast, the overall conductance of a solid copper rod (thermal conductivity $k_{copper} \approx 400$ W/m-K) of diameter and length equal to the inner diameter and total length of the GHP (0.935 inches = 0.023749 m and 27.75 inches = 0.70485 m, respectively) is 0.251 W/°C. Thus, the values of the overall conductance of the GHP for the experimental settings and conditions reported in Table 4.1 were 7.27 to 33.67 times higher than that of the aforementioned solid copper rod of corresponding dimensions, which is quite impressive. These results for the repeatability runs were very similar (runs 1R to 8R are presented in Table 4.2; and runs 9R to 15R are presented in Table 4.3). It should also be noted that the aforementioned increases in the overall conductance of the GHP would be even more impressive for longer lengths of its adiabatic section. This is because the overall conductance of the GHP would not be significantly affected by the length of its adiabatic section, provided its operational limits are not reached [Faghri (2012, 2014); Dunn and Reay (2012); Jafari et al. (2016)]; however, the overall conductance of a solid copper rod of constant cross-section is inversely proportional to its length [Incropera and Dewitt (2002)].

For the settings and conditions investigated in the preliminary and repeatability runs (see Tables 4.1 to 4.3), for fixed values of the fill ratio, *FR*, the value of C_{GHP} increased with increasing values of $q_{in,tot}$. This is because as $q_{in,tot}$ was increased from 50 W (nominal) to 250 W (nominal), the conditions in the evaporator went from the intermittent (and somewhat chaotic) geyser boiling regime to the vigorous (and effectively steady) nucleate pool boiling regime, with corresponding increases in the boiling heat transfer coefficient on the inner surface of the evaporator-tube wall.

It should also be noted that for similar values of $q_{in,tot}$, the highest values of C_{GHP} were obtained for *FR* = 100 %, and not 150 % or 175 %. This is because for similar rates of $q_{in.tot}$, the values of $\overline{T}_{evap}^{wall}$ are higher for higher values of *FR*, and $\overline{T}_{cond}^{wall}$ does not change as significantly, as was discussed in Subsection 4.1.2 and 4.1.3; thus, the values of C_{GHP} as defined in Equation (4.1) go down. These results for the repeatability runs were very similar (runs 1R to 8R are presented in Table 4.2; and runs 9R to 15R are presented in Table 4.3). Similar results were also obtained in the benchmarking runs (undertaken to obtain a baseline for assessing the GBP): the related discussions and a graphical presentation of the C_{GHP} results are given in Subsection 4.2.2.

4.1.6 Boiling regimes in the evaporator section

The boiling regimes in the evaporator section of the GHP are indicated in the last columns of Tables 4.1 to 4.3. The geyser boiling phenomenon (GBP) (see related description and discussions presented in Chapters 1, Subsection 1.2.4; Chapter 2, Section 2.2; and Chapter 3, Section 3.6) prevailed for values of $q_{in,tot}$ below 140 W (nominal); for values of $q_{in,tot}$ ≥ 150 W (nominal), nucleate boiling conditions prevailed; and the transition between these two boiling regimes occurred (intermittently or haphazardly) in the range 140 W (nominal) ≤ $q_{in,tot}$ ≤ 150 W (nominal). Similar results were reported by Boopathy (2017) and were also obtained in the benchmarking runs undertaken in this work. The latter (results of the benchmarking runs) are elaborated, with related discussions and flow-visualization pictures, in Subsection 4.2.3.

4.1.7 Results of the repeatability runs

All preliminary runs were repeated, some of them several times. The 15 preliminary and one set of the corresponding 15 repeatability runs are denoted as Runs # 1 to 15 and Runs # 1R to 15R, respectively. They are presented together for comparison purposes in Table 4.2 (for Runs # 1 to 8 and 1R to 8R) and Table 4.3 (for Runs # 9 to 15 and 9R to 15R), along with the mean values of corresponding results, the absolute differences about the mean, and the absolute percentage differences about the mean.

The results in Tables 4.2 and 4.3 show the following: the q_{loss} values were repeatable to within ± 1.40 %; the q_{in} values were repeatable to within ± 0.77 %; the $\overline{T}_{evap}^{wall}$ values are repeatable to within ± 0.58 %; the $\overline{T}_{evap}^{water}$ values were repeatable to within ± 0.50 %; the $\overline{T}_{cond}^{wall}$ values were repeatable to within ± 0.59 %; the $\overline{T}_{cond}^{vapor}$ values were repeatable to within ± 3.48 %; the $\overline{P}_{cond}^{vapor}$ values were repeatable to ± 1.49 %; and the C_{GHP} values were repeatable to within ± 1.07 %. When contrasting these repeatability bands with the lower experimental uncertainties (in the measured local instantaneous temperatures and instantaneous pressure) mentioned on p. 72, it should be kept in mind that $\overline{T}_{evap}^{wall}$ and $\overline{T}_{cond}^{wall}$ are spatial- *and* time-averaged values of over 1000 instantaneous measurements at 10 different locations on the evaporator and condenser tubes, respectively; each of $\overline{T}_{evap}^{water}$, $\overline{T}_{cond}^{vapor}$, and $\overline{P}_{cond}^{vapor}$ are time-averaged values of over 1000 instantaneous measurements; and q_{loss}, q_{in}, and C_{GHP} were computed using equations that involve the aforementioned spatial- and time-averaged values [Taylor and Kuyatt (1994); ASME Standard PTC (2005)].

4.1.8 Dynamic fill ratio

The flow visualizations done during the preliminary and repeatability runs (and in the benchmarking runs done later), showed a very interesting feature of the GHP when it was in operation: *during the experiments*, the *level* of the *boiling* water in the evaporator section of the GHP was significantly higher than the initial level of the non-boiling water in this section (corresponding to the initial fill ratio). In hindsight, this was not a surprising result: the boiling water in the evaporator section, in both the geyser boiling and nucleate boiling regimes, is a mixture of liquid water and vapor bubbles; the density of the vapor is considerably lower than that of the liquid water; thus, for the same mass, the volume of the (liquid water + vapor bubbles) mixture is higher than the initial volume of the liquid water (prior to the operation of the GHP).

Furthermore, the volume of the (liquid water + vapor bubbles) mixture in the evaporator changed with the total rate of heat input, $q_{in,tot}$, and the boiling regime (geyser or nucleate pool boiling); and it oscillated with time. These oscillations were quite significant and sporadic (but roughly cyclical) in the geyser boiling regime; and they were not as significant, but still present and cyclical, in the nucleate pool boiling regime. In this context, an operational or dynamic fill ratio of the GHP can be defined as follows: {volume occupied by the (liquid water + vapor bubbles) mixture in the evaporator section during GHP operation} / {total volume between the solid components within the evaporator section}.

In general, the dynamic fill ratio would be a function of the aspect ratio ($L_{Evaporator} / D_i$), the working fluid, the material of the containment tube and the roughness of its inner surface, and the total rate of heat input to the evaporator, $q_{in,tot}$. Furthermore, it could influence and be influenced by the boiling regime (geyser or nucleate pool boiling) that occurs in the evaporator. To date, none of the published works on GHPs have discussed this aspect of their operation (to the knowledge of the author). Thus, determining and discussing the existence of this dynamic fill ratio during the operation of GHPs is one of the novel (original) contributions of this work.

Unfortunately, in this work, the (liquid water + vapor bubble) mixture in the GHP did not always rise to levels within the flow-visualization portion of the adiabatic section of the GHP, with the experimental settings and conditions given in Table 4.1 to 4.3. Thus, it was not possible to obtain accurate quantitative data on the dynamic fill ratio. A modification of the GHP to allow the recording of such data is recommended as a worthwhile extension of this work.

4.2 Benchmarking Experiments and Results

During the preliminary and repeatability runs described in the previous section, it was noticed that the time-averaged local temperatures of the evaporator wall were not necessarily axisymmetric. This anomaly was caused by the off-set (non-axisymmetric) insertion of a shielded thermocouple that was used to measure T_{evap}^{water}. This difficulty was overcome by recessing this shielded thermocouple to a level that was below the start of the active heating portion of the evaporator section. Furthermore, the data acquisition and control program used in the preliminary and repeatability runs recorded and processed a lot of data, so the sampling rate of the T_{evap}^{wall} measurements was not high enough for a proper FFT analysis of them. This issue was resolved by designing and implementing a new data acquisition and control program, which allowed a much faster sampling rate of the T_{evap}^{wall} measurements (by a factor > 10; to exceed the Nyquist theorem requirements with respect to the expected oscillation frequencies). Additional details of these two key improvements of the overall experimental setup and procedures were provided in Chapter 3, so they are not repeated here.

After the implementation of the improvements mentioned above, a total of 12 experimental runs were undertaken to establish a baseline for the assessment of the four proposed techniques for the mitigation of the geyser boiling phenomenon (GBP) in the GHP. These 12 runs are referred to as 'benchmarking runs' in this thesis.

4.2.1 Overview

The experimental settings, conditions, and results for the 12 benchmarking runs, labelled as Runs # 1BM to 12BM, are summarized in Table 4.4 (given on the next page) and discussed in Subsections 4.2.2 to 4.2.3. The uncertainties in the experimental measurements in these runs were the same as those mentioned in Subsection 4.1.1, and the repeatability bands of the results were similar to those discussed in Subsection 4.1.7, so they are not repeated here. The notations used in Table 4.4 for the experimental settings and conditions, and the results, are the same as those used in Tables 4.1 to 4.3. However, the benchmarking runs were conducted for only two values of the fill ratio, *FR* = 100 % and 150 %, as the preliminary and repeatability runs showed that for *FR* = 175 %, some values of T_{evap}^{wall} exceeded the cut-off limit when $q_{in,tot}$ > 220 W. The benchmarking runs with *FR* = 100 % and 150 % allowed $q_{in,tot}$ values in the range 50 W to 300 W (nominal).

Table 4.4 Experimental settings, conditions, and results for benchmarking runs 1BM to 12BM.

Settings and Conditions									Results								
Run #	**FR [%]**	$q_{in,tot}$ **[W]**	**Current [A]**	**Voltage [V]**	T_{WB} **[ºC]**	$T_{\infty,evap}$ **[ºC]**	$T_{\infty,adiab}$ **[ºC]**	$T_{\infty,cond}$ **[ºC]**	q_{loss} **[W]**	q_{in} **[W]**	$\overline{T}^{wall}_{evap}$ **[ºC]**	$\overline{T}^{water}_{evap}$ **[ºC]**	$\overline{T}^{wall}_{cond}$ **[ºC]**	$\overline{T}^{vapor}_{cond}$ **[ºC]**	$\overline{P}^{vapor}_{cond}$ **[mbar]**	C_{GHP} **[W/ºC]**	**Boiling in evap**
1BM	100	50.25	0.980	51.281	19.90	26.39	25.43	25.89	1.244	49.01	41.38	34.44	20.69	22.21	39.44	2.369	Geyser
2BM		100.75	1.387	72.616	19.90	27.86	25.33	25.72	1.303	99.44	42.51	36.92	21.54	25.04	47.63	4.742	Geyser
3BM		150.14	1.694	88.651	19.89	31.17	25.87	26.23	1.399	148.74	45.74	39.03	22.34	28.37	56.04	6.518	Nucleate
4BM		200.38	1.957	102.42	19.90	32.73	25.90	26.21	1.642	198.74	48.70	40.42	23.01	31.45	61.37	7.736	Nucleate
5BM		250.60	2.188	114.54	19.89	30.60	26.94	27.22	2.015	248.59	53.32	42.89	23.75	34.41	70.14	8.407	Nucleate
6BM		300.74	2.397	125.48	19.87	33.89	27.23	27.87	2.290	298.45	58.15	45.45	24.50	38.03	80.34	8.869	Nucleate
7BM	150	50.27	0.980	51.292	19.87	27.84	26.97	27.78	1.339	48.93	44.18	37.66	20.73	22.36	48.49	2.087	Geyser
8BM		100.56	1.386	72.548	19.87	29.04	27.50	28.21	1.335	99.22	44.85	40.09	21.47	25.92	51.04	4.244	Geyser
9BM		150.24	1.694	88.682	19.86	31.33	27.96	28.42	1.436	148.81	47.10	40.99	22.20	29.14	55.13	5.976	Nucleate
10BM		200.24	1.956	102.38	19.84	34.28	29.53	29.54	1.602	198.64	51.04	42.76	22.87	31.94	62.86	7.051	Nucleate
11BM		250.67	2.188	114.56	19.83	33.62	28.86	28.97	2.022	248.65	55.63	45.15	23.55	34.08	72.36	7.751	Nucleate
12BM		300.06	2.394	125.34	19.86	37.66	28.91	28.86	2.280	297.78	60.17	47.52	24.31	36.62	82.72	8.304	Nucleate

4.2.2 Variations of GHP overall conductance with fill ratio and total rate of heat input

The values of C_{GHP} for the benchmarking runs are presented in Table 4.4: for Runs # 1BM to 6BM (*FR* = 100 %), they range from 2.369 W/ºC to 8.869 W/ºC; and for Runs # 7BM to 12BM (*FR* = 150 %), they range from 2.087 W/ºC to 8.304 W/ºC. These values of C_{GHP} are 8.31 to 35.33 time higher than the 0.251 W/ºC overall conductance of a solid copper rod of diameter and length equal to the inner diameter and total length of the GHP.

For the settings and conditions investigated in the benchmarking runs (see Table 4.4), the variations of C_{GHP} with $q_{in,tot}$ for *FR* = 100 % and 150 % are shown graphically in Figure 4.1. For a fixed value of *FR*, the value of C_{GHP} increases with increasing values of $q_{in,tot}$; and for a fixed value of $q_{in,tot}$, the value of C_{GHP} decreases when *FR* is increased from 100 % to 150 %. The reasons for these trends are the same as those discussed in Subsection 4.1.5, so they are not repeated here.

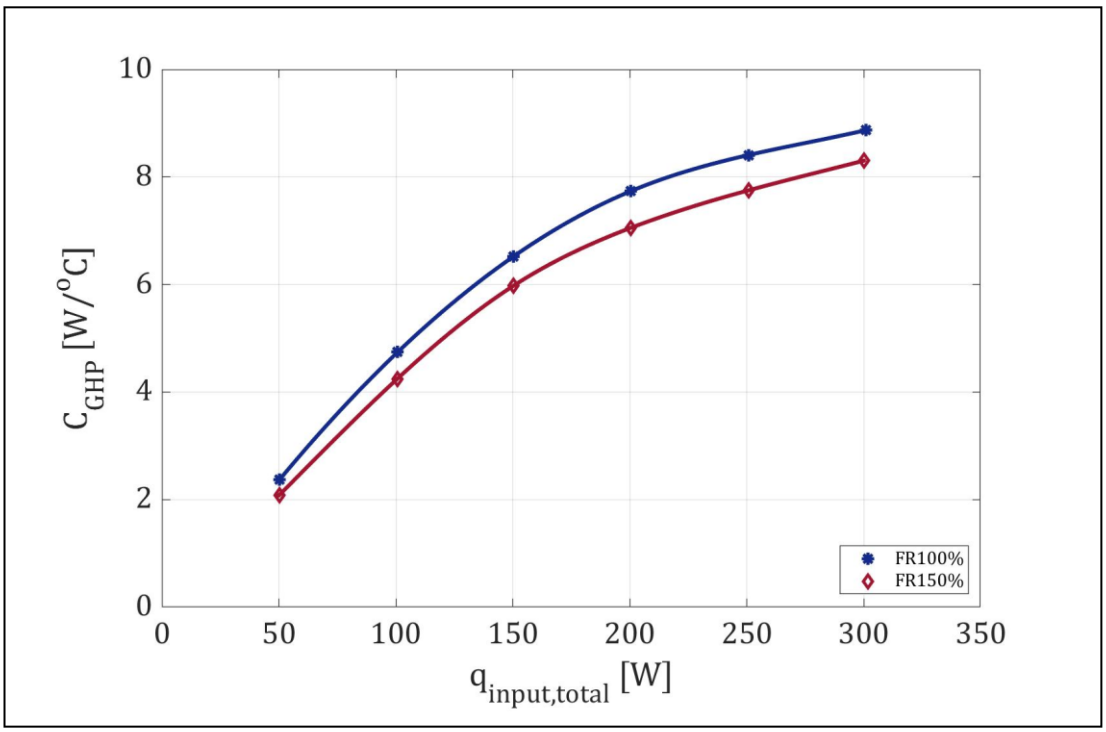

Figure 4.1 Variations of the overall conductance of the GHP with total rate of heat input for fill ratios of *FR* = 100 % and 150 % in the benchmarking runs.

4.2.3 Boiling regimes in the evaporator section

For the benchmarking runs, the boiling regimes in the evaporator section of the GHP are indicated in the last column of Table 4.4. These results are similar to those obtained in the preliminary and repeatability runs, and the discussions given in Subsection 4.1.6 also apply here. The geyser boiling phenomenon (GBP) prevailed for values of $q_{in,tot}$ below 140 W (nominal); for values of $q_{in,tot}$ ≥ 150 W (nominal), nucleate boiling conditions prevailed; and the transition between these two boiling regimes occurred (intermittently or haphazardly) for values of $q_{in,tot}$ in the range 140 W (nominal) to 150 W (nominal).

Flow visualization photographs for *FR* = 150 % and the experimental setting and conditions corresponding to Runs # 7BM ($q_{in,tot}$ = 50.27 W; geyser boiling) and 11BM ($q_{in,tot}$ = 250.67 W; nucleate boiling) are presented in Figures 4.2 and 4.3, respectively. These pictures were obtained by using frame-capturing on video recordings (Nikon Camera *D3500 DSLR,* via *video editor*) through the transparent borosilicate glass portion of the adiabatic section of the GHP.

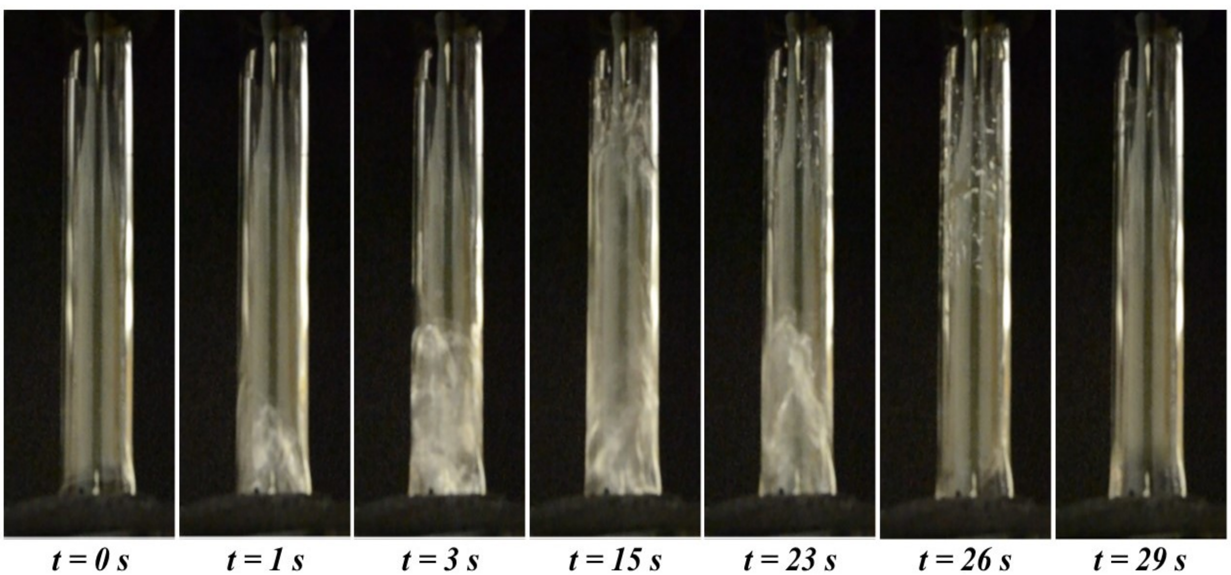

Figure 4.2 Flow visualization photographs at selected times during one full cycle of geyser boiling for Run # 7BM: *FR* = 150 % and $q_{in,tot} =$ 50.27 W.

For the geyser boiling conditions portrayed in Figure 4.2 (Run # 7BM), a quiescent liquid-vapor interface is seen close to the bottom of the left-most photograph at time t = 0 s; then, chaotic eruptions of the liquid can be seen in the photographs corresponding to 1 s $\le t \le$ 26 s; and the final photograph shows a return to a quiescent liquid-vapor interface at time t = 29 s. These pictures are somewhat similar to the schematic illustrations of the geyser boiling phenomenon depicted schematically in Figure 1.3.

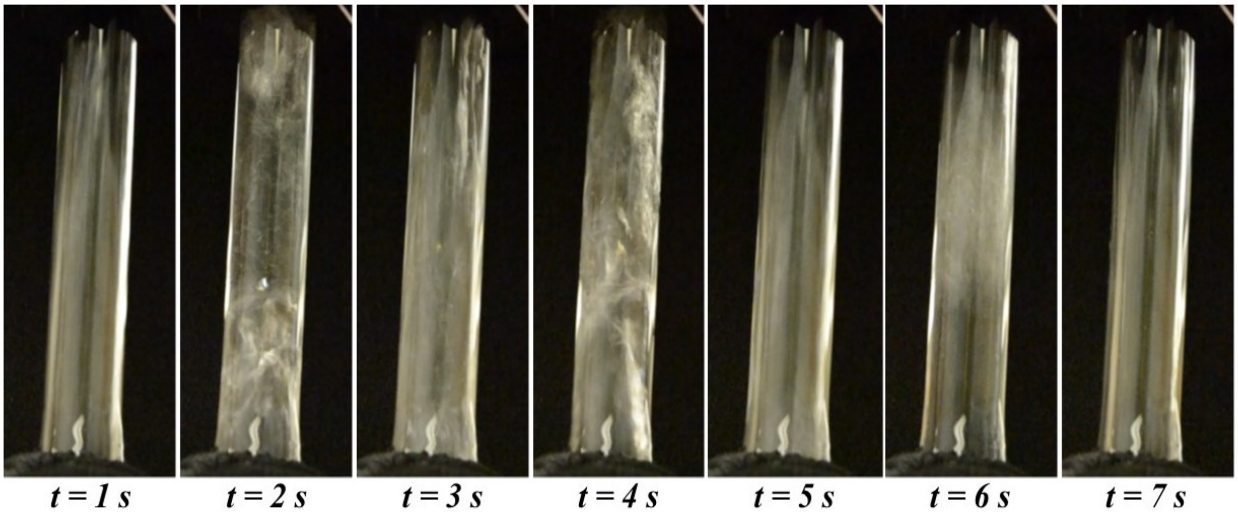

Figure 4.3 Flow visualization photographs at selected times during a period of nucleate boiling for Run # 11BM: *FR* = 150 % and $q_{in,tot} =$ 250.67 W.

In Figure 4.3, which corresponds to nucleate boiling conditions (Run # 11BM), the visualization photographs show an effectively *steady* (but broken, turbulent, and ruffled) condensate film flowing down the inner surface of the borosilicate glass tube and a vapor core (*thus*, pictures corresponding only to t = 1 s, 2 s, 3 s, 4 s, 5 s, 6 s, and 7 s are shown in this figure).

4.3 Experiments with the Proposed Techniques for Mitigating Geyser Boiling in the GHP, Results, and Assessment

In this work, four different techniques were proposed for mitigating the geyser boiling phenomenon (GBP) in the GHP: 1) single-layer-wire-mesh (SLWM) technique (discussed in Subsection 3.6.6.1); 2) triple-layer-wire-mesh (TLWM) technique (discussed in Subsection 3.6.6.2); 3) eight-disks-single-layer-wire-mesh (8DSLWM) technique (discussed in Subsection 3.6.6.3); and 4) ten-disks (10D) technique (discussed in Subsection 3.6.6.4). An overview of the experiments conducted with each of these four techniques is presented in the next subsection. Then, the results obtained in these experiments are presented in the next three subsections. An assessment of the effectiveness of the four techniques is presented in the final subsection.

4.3.1 Overview

The results of the benchmarking runs presented and discussed in Subsection 4.2.2 showed the following two main features: 1) the highest values of overall GHP conductance, C_{GHP}, were obtained with FR = 100 %; 2) the GBP occurred for values of $q_{in,tot}$ that ranged from 50 W (nominal) to about 140 W (nominal); and 3) nucleate boiling prevailed for $q_{in,tot}$ ≥ 150 W (nominal). Similar results were obtained in the preliminary and repeatability runs presented and discussed in Subsection 4.1.5. Thus, the experiments with the four different techniques proposed for mitigating the GBP in the GHP were conducted only for FR = 100 %, with values of $q_{in,tot}$ in the range 50 W (nominal) to 150 W (nominal).

In this context, another important point should also be noted: for values of $q_{in,tot}$ > 150 W (nominal), with each of the SLWM, 8DSLWM, and the 10D techniques deployed inside the evaporator section of the GHP, one or more values of T_{evap}^{wall} exceeded the safety cut-off temperature (which was set at 85 ºC in these experiments); and this problem occurred at $q_{in,tot}$ > 95 W (nominal) when the TLWM technique was deployed. The cause of this problem could not be conclusively ascertained, as it was not possible to see what was happening inside the evaporator section. In this context, it should be noted that the flow-visualization segment of the GHP was a part of its adiabatic section, which allowed viewing of parts of the (explosive) GBP and the condensate film which occurred *above* the evaporator section, but not the bubble generation and growth during boiling (geyser or nucleate) *inside* the evaporator section.

Nevertheless, the most likely cause of the problem mentioned above *appears* to be the following: when regular nucleate boiling is established for $q_{in,tot}$ > 150 W (nominal), or for $q_{in,tot}$ > 95 W in the case of the TLWM technique, the rates of generation and growth of the vapor bubbles on inner surface of the core tube in the evaporator section are relatively high (compared to those for geyser boiling at the lower values of $q_{in,tot}$); and under these conditions, because of surface-tension effects, it is easier for some of the vapor bubbles to coalesce and form a vapor film on the inner surface of the tube, in the gaps between it and the wire mesh or the outer edge of the disks, than to push through the openings in the wire mesh or the perforations in the disks. Some support for this proposition is obtained from the observation that this problem occurred at

$q_{in,tot}$ > 95 W (rather than 150 W) for the TLWM technique, for which the effective size of the openings with the three overlapping layers of the wire mesh is smaller than that with just one layer of the mesh. It may be possible to solve this problem by attaching the wire mesh or the outer edge of the perforated disks to the inner surface of the tube (using a thin layer of a high-conductivity water-proof glue, for example) and thus eliminating the above-mentioned gaps. However, due to time and funding restrictions in this project, it was not possible to try out this idea. Thus, it is suggested as a possible extension of this work.

4.3.2 Variations of GHP overall conductance with total rate of heat input for the benchmarking runs and the four different GBP mitigation techniques

The variations of the C_{GHP} with $q_{in,tot}$ for the benchmarking runs and the experiments with each of the four techniques proposed for mitigating the GBP in the GHP are depicted graphically in Figure 4.4. For the reasons discussed the previous subsection, the nominal range of the $q_{in,tot}$ values was 50 W to 150 W when the SLWM, 8DSLWM, and the 10D techniques were deployed in the GHP, and only 50 W to 95 W when the TLWM was deployed.

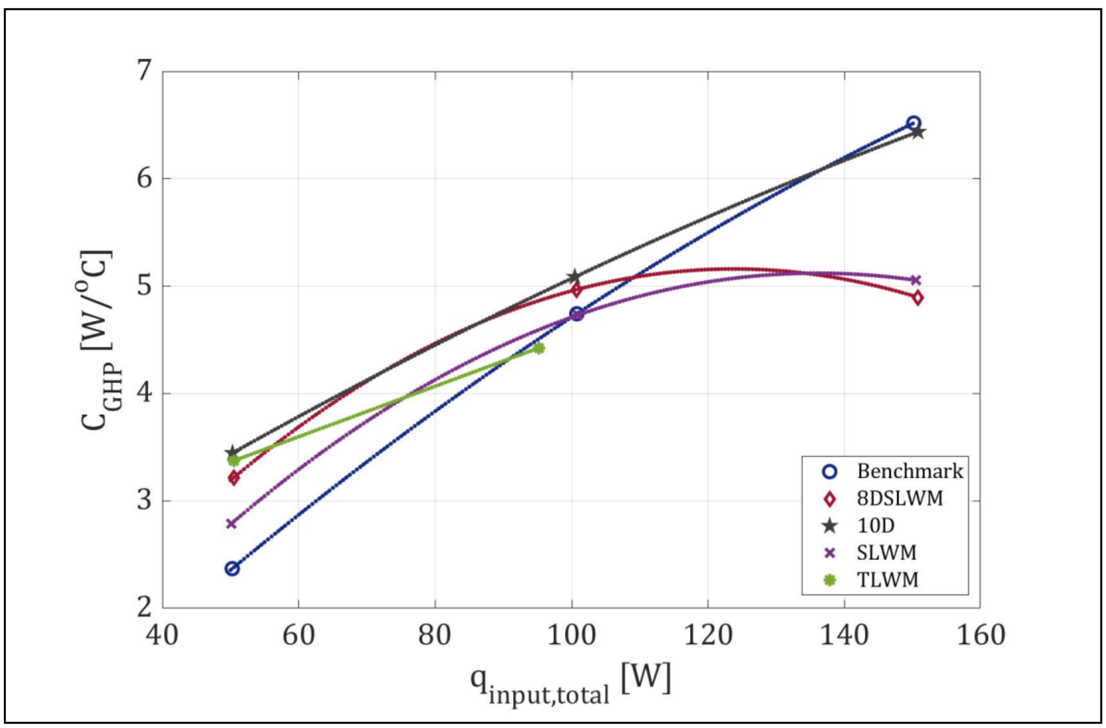

Figure 4.4 Variations of the overall conductance of the GHP with total rate of heat input for the benchmarking runs and each of the four GBP mitigation techniques (*FR* = 100 %).

The results in Figures 4.4 show that for 50 W (nominal) $\leq q_{in,tot} \leq$ 100 W (nominal) the values of C_{GHP} obtained with the 8DSLWM, 10D, and SLWM techniques are all higher than those obtained in the benchmarking runs; and this statement applies for 50 W (nominal) $\leq q_{in,tot} \leq$ 95 W with the TLWM technique, which could not be used for $q_{in,tot} >$ 95 W (nominal). For values of $q_{in,tot}$ in the range 100 W (nominal) $< q_{in,tot} \leq$ 150 W (nominal), the values of C_{GHP} obtained with the 8DSLWM and SLWM techniques flatten out to levels below those obtained with in the benchmarking runs (possibly due to the build-up of a vapor film next to the inner surface of the core tube of the evaporator section, for reasons presented in Subsection 4.3.1); but the values of C_{GHP} obtained with the 10D technique remain either above or almost equal to those obtained in the benchmarking runs.

4.3.3 Variations of the maximum change in evaporator-wall temperature and the corresponding time-period with the total rate of heat input for the benchmarking runs and the four different GBP mitigation techniques

The maximum change in the evaporator-wall temperature and the time-period associated with this change are denoted here simply as $(\Delta T)_{\max}$ and t_{period}, respectively. The above mentioned variations of $(\Delta T)_{\max}$ and t_{period} were determined by examining screenshots of the displays of the experimental data (on the monitor of the PC) created by a *National Instruments* LabView program. This program was specially designed, written, and used for data acquisition and control in the benchmarking runs and the experiments with the four different GBP mitigation techniques. Examples of such screen shots for conditions corresponding to geyser boiling in the evaporator are shown in Figures 4.5 and 4.6 for Runs # 1BM (FR = 100%, $q_{in,tot} =$ 50 W) and 2BM (FR = 100%, $q_{in,tot} =$ 100 W), respectively. Such screen shots were recorded for all benchmarking runs in which the GBP occurred (setting and conditions are given in Table 4.4) and the experiments with the four different GBP mitigation techniques (FR = 100% and 50 W $\leq q_{in,tot} \leq$ 150 W). They were all similar to those illustrated in Figures 4.5 and 4.6.

It should be noted that the values of $(\Delta T)_{\max}$ and t_{period} for each experimental run were obtained by averaging data from 15 to 25 consecutive oscillations of the evaporator-wall temperatures. Another point to note is that in each of the screen shots, akin to those in Figures 4.5

and 4.6, the abscissa corresponds to the number of data sets: the elapsed time between successive data sets in each of the experimental runs was about 1 s to 2 s.

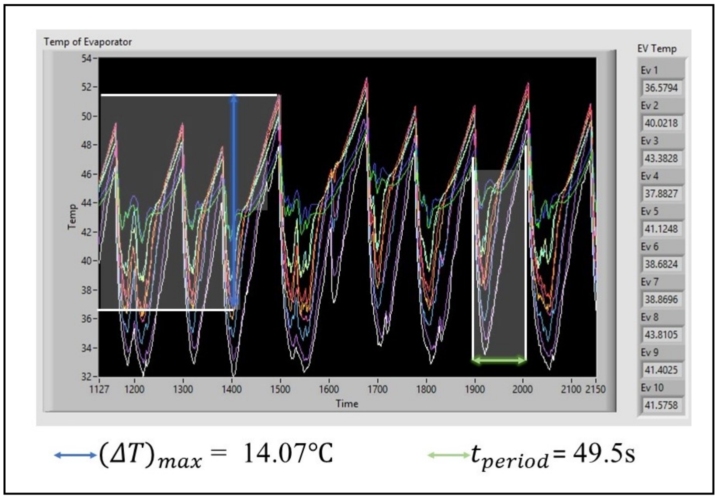

Figure 4.5 Screenshot of the PC monitor display of experimental data for Run # 1BM (FR = 100% and $q_{in,tot} = 50.25$ W).

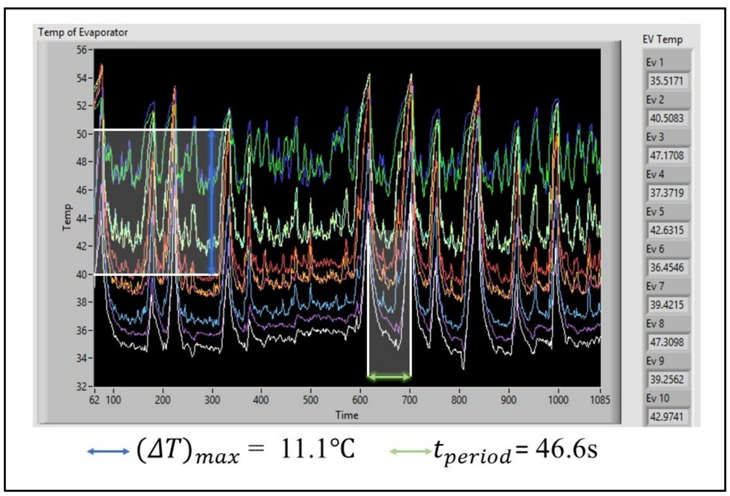

Figure 4.6 Screenshot of the PC monitor display of experimental data for Run # 2BM (FR = 100% and $q_{in,tot} = 100.75$ W).

In summary, the results obtained using screenshots similar to those illustrated in Figures 4.5 and 4.6, for the benchmarking runs in which GBP occurred (setting and conditions given in Table 4.4) and the experiments with the four different GBP mitigation techniques (FR = 100% and 50 W $\leq q_{in,tot} \leq$ 150 W), showed the following trends: 1) *in the benchmarking runs*, the values of t_{period} decrease with increasing values of the values of $q_{in,tot}$, because at the higher power inputs, vapor bubbles are generated at a higher rate, so the cycles of the GBP (for an example, see Figure

4.2) occur with increasing frequency (or shorter t_{period}); 2) *in the benchmarking runs*, the values of $(\Delta T)_{\max}$ decrease with increasing values of $q_{in,tot}$ and the related values of t_{period} lower (for the reasons given above), thus there is less time for significant excursions of T_{evap}^{wall} about it mean values for each run; and 3) *in the experiments with each of the four different GBP mitigation techniques*, nucleate boiling was effectively achieved for 50 W $\leq q_{in,tot} \leq$ 150 W (50 W $\leq q_{in,tot} \leq$ 95 W with the TLWM technique), so the frequency of the vapor-bubble generation was much higher and the mean size of the vapor bubbles was much smaller than those for the GBP in the benchmarking runs, the values of t_{period} and $(\Delta T)_{\max}$ were much smaller than those for the benchmarking runs, and the variations of $(\Delta T)_{\max}$ with $q_{in,tot}$ were effectively negligible. It should also be noted here that at $q_{in,tot}$ = 150 W (nominal), nucleate boiling prevailed in all cases. These variations of $(\Delta T)_{\max}$ with $q_{in,tot}$ are illustrated in Figure 4.7.

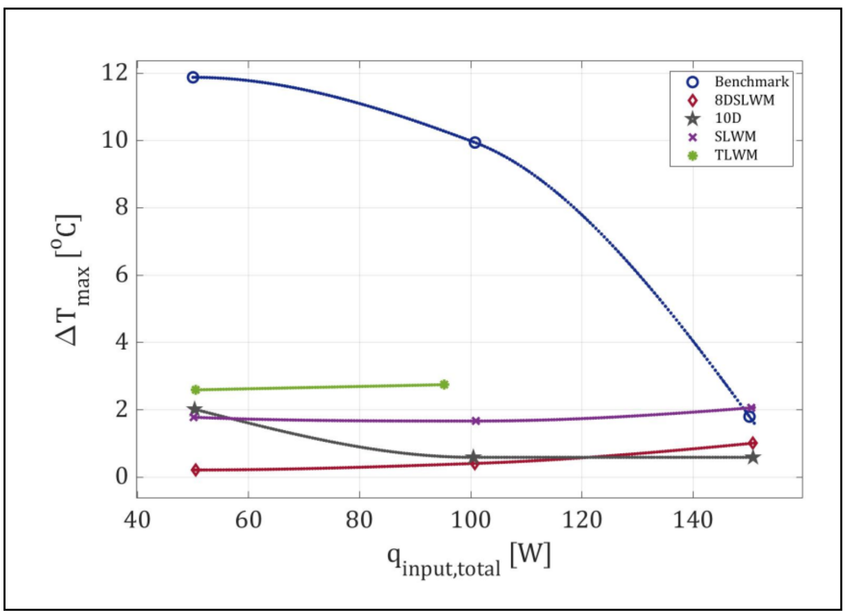

Figure 4.7 Variations of $(\Delta T)_{\max}$ with $q_{in,tot}$ for the benchmarking runs and each of the four GBP mitigation techniques (*FR* = 100 %).

4.3.4 Fast-Fourier-Transform (FFT) analyses of the evaporator-wall temperature

The video recordings of the fluid-flow phenomena in the segment of the adiabatic section of the GHP (discussed in Subsection 4.2.3) and the graphical representations of the measured (T_{evap}^{wall} *vs* t) data (discussed in Subsections 4.3.3) were used to obtain a good *qualitative* feel for the nature of the GBP. In addition, to obtain a *quantitative* assessment of the four proposed techniques for mitigation of the GBP, the Fast-Fourier-Transform (FFT) technique [Ramirez (1985)] was adopted for analyses of the (T_{evap}^{wall} *vs* t) data. As was mentioned previously in Chapters 1 and 3, this appears to be the first use of the FFT technique for analyses of data related to the GBP in a *single-tube* GHP; however, in a recent work [Elkholy and Kemper (2020)], the FFT technique was used to analyze the pressure signal corresponding to the GBP in a two-phase *loop* thermosyphon.

The preliminary runs (Runs # 1 to 15) and the benchmarking runs (Runs # 1BM to 12BM) showed that the (T_{evap}^{wall} *vs* t) data obtained from the eighth of the 10 thermocouples deployed on the core tube of the evaporator section displayed either the highest or close to the highest absolute values of the amplitude of the time-oscillations ($|(T-T_{av})_{evap}^{wall}|$; where $T_{av,evap}^{wall}$ is the time-average value of T_{evap}^{wall}) during conditions corresponding to the GBP. This eighth thermocouple (denoted as Ev8) was located 2 inches above the start of the active-heating portion of the evaporator section. Thus, the $(T-T_{av})_{Ev8}$ *vs* t data were chosen for the FFT analyses. They were done using a special computer program (written using MATLAB R2018a) for FFT analyses of digital data in which the sampling times are not uniform [Ramirez (1985)].

The FFT analyses of the $(T-T_{av})_{Ev8}$ *vs* t data are presented in Figure 4.8 for FR = 100 % and $q_{in,tot}$ = 50 W (nominal) and in Figure 4.9 for FR = 100 % and $q_{in,tot}$ = 100 W (nominal) for the benchmarking runs (1BM and 2BM, respectively) and the corresponding experiments with the four techniques for mitigating GBP. In the plots presented in these figures, the absolute amplitude of the FFT spectrum is presented on the ordinate, and the frequency is presented on the abscissa. These plots show that *all* four GBP mitigation techniques are quite effective in cutting down the amplitude of the oscillations in $(T-T_{av})_{Ev8}$ *vs* t data for the cases considered in this work.

For FR = 100 % and $q_{in,tot}$ = 50 W (nominal), the plots in Figure 4.8, show that the 8DSLWM technique is the most effective in mitigating the GBP encountered in the benchmarking runs, but it is only slightly better than the 10D technique. For FR = 100 % and $q_{in,tot}$ = 100 W (nominal), the plots in Figure 4.9, show that the 10D technique is the most effective, but it is only marginally better than the 8DSLWM technique. Similar conclusions could be drawn from the FFT analyses of the other experimental runs (therefore, graphical presentations of these other FFT analyses are not included here).

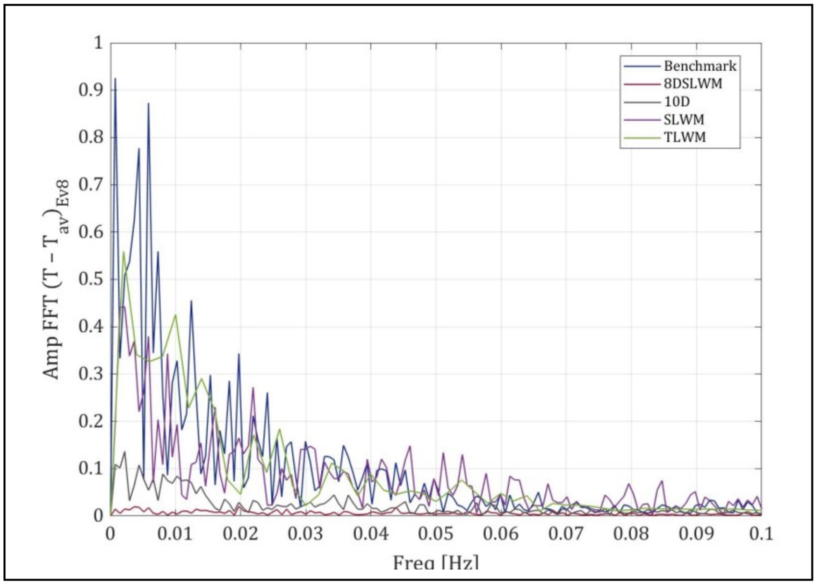

Figure 4.8 Graphical presentation of the FFT analyses of the $(T - T_{av})_{Ev8}$ *vs* t data for *FR* = 100 % and $q_{in,tot}$ = 50 W (nominal).

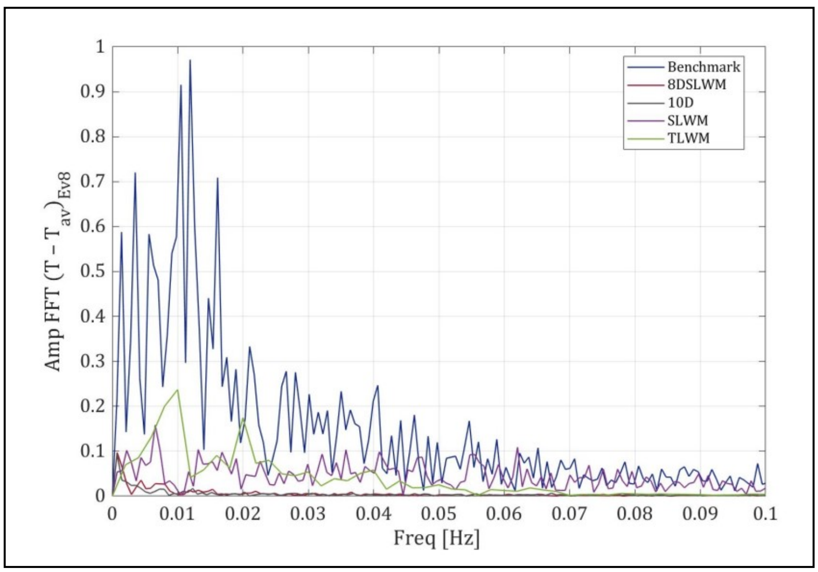

Figure 4.9 Graphical presentation of the FFT analyses of the $(T - T_{av})_{Ev8}$ *vs* t data for *FR* = 100 % and $q_{in,tot}$ = 100 W (nominal).

4.3.5 Assessment of the four proposed techniques for mitigating geyser boiling

Based on the results and discussions presented in Subsections 4.3.1 to 4.3.5, the following main conclusions can be made regarding the four proposed techniques for mitigation GBP in the

GHP investigated in work, for FR = 100 % and the corresponding experimental settings and conditions presented in Tables 4.1 to 4.4.

1) With regard to the desirability of obtaining high values of C_{GHP}, the 10D technique is clearly better than the other three techniques; the 8DSLWM technique could be considered as the second best, but it significantly reduces the value of C_{GHP} below that obtained with the 10D technique for $q_{in,tot}$ > 100 W (nominal); and the TLWM technique is not suitable for $q_{in,tot}$ > 95 W (nominal) with the GHP used in this work.

2) The main finding from the FFT analyses of the $(T - T_{av})_{Ev8}$ *vs t* data can be summarized as follows: i) the 8DSLWM and 10D techniques are the most effective in reducing the amplitude of the oscillations in the $(T - T_{av})_{Ev8}$ *vs t* data (almost completing mitigating the GBP encountered in the corresponding benchmarking runs); ii) the 8DSLWM technique is only slightly better than the 10D technique in some cases; and iii) in the other cases, the 10D technique is only marginally better than the 8DSLWM technique.

3) The evaporator-wall temperature exceeded the safety cut-off temperature (85 ^{o}C was the set value in the experiments with the mitigation techniques) for $q_{in,total}$ > 150 W (nominal) when the SLWM, 8DSLWM, and 10D techniques were deployed; and for $q_{in,total}$ > 95 W (nominal) when the TLWM technique was deployed. The most likely cause of this problem for these conditions *appears* to be the formation of a vapor film on the inner surface of the tube, in the gaps between it and the wire mesh or the outer edge of the perforated disks (as surface-tension effects and the relatively high rates of production of the bubble and their growth adversely affect the ability of the vapor bubbles to push through the openings in the wire mesh or the perforations in the disks).

Final assessment: In the light of the main findings summarized in all three points given above, the 10D technique is the most effective of the four techniques proposed for mitigating the GBP in the GHP investigated in this work. However, additional investigations are needed to find an effective way to overcome the overheating problem mentioned above in point three.

Chapter 5: Conclusion

This final chapter contains a review of the earlier chapters of this thesis, a summary of the main findings and contributions of this work, and some recommendations for extensions of this work.

5.1 Review of the earlier Chapters of this Thesis

In Chapter 1, the background, motivation, and overall goal of this work were presented and discussed first. Then, a review of the pertinent literature was presented. The specific objectives of this work were presented next. In the final section of this chapter, the plan or organization of the thesis was given.

In Chapter 2, the theoretical considerations that were used for developing a basic understanding of the various thermofluid phenomena that occur within gravity heat pipes (GHPs) were discussed briefly. The dimensionless geometric parameters and some of the dimensionless thermofluid parameters that govern GHPs (and the physical interpretations of the latter) were also presented in Chapter 2, along with the values or ranges of values of these dimensionless parameters that apply to the GHP experiments conducted in this work.

Brief descriptions of the GHP and the supporting experimental setup that were originally designed and implemented by Boopathy (2017), and refurbished, improved, and used in this work, were presented first in Chapter 3. After that, the improvements effected in this work were presented and discussed. Then, some of the options that have been proposed in the literature for mitigating the geyser boiling phenomena (GBP) in GHPs were presented and discussed concisely. After that, the full details of four different techniques that were proposed in this work for mitigating the GBP in GHPs were presented along with a discussion of the rationale behind each of them. Finally, the procedures that were used to run the experiments in this work were presented.

The experimental results obtained in this work, and an assessment of the four proposed techniques for mitigating the GBP in GHPs, were presented and discussed in Chapter 4.

5.2 Summary of the Main Findings and Contributions of this Work

The main findings and contributions of this work are summarized below:

1. A GHP and the supporting experimental setup originally designed and implemented by Boopathy (2017) were refurbished and then improved (the related details were presented and discussed in Chapter 3, Sections 3.1 and 3.2). One of the key improvements was the design and implementation of a new LabVIEW code for data acquisition and control. It speeded up the sampling rate of a set of 10 thermocouples attached to the outer surface of the evaporator tube of the GHP, by a factor of over 10 compared to that provided by the previous code. This faster sampling rate was critically important for proper Fast Fourier Transform (FFT) analyses of the temperature measurements (the FFT analyses were used in this work for a quantitative examination of the GBP in the GHP).
2. Fifteen preliminary experiments were conducted with the refurbished GHP, and the results were shown to be repeatable to within acceptable limits (the related details were provided and discussed in Chapter 4, Section 4.1). For the settings and conditions investigated in this work (full details are given in Tables 4.1 to 4.3), the main findings, based on an examination of the results of the preliminary runs, were the following: i) the GBP occurred when the total rate of heat input to the evaporator section, $q_{in,total}$, was less than or equal to 140 W; ii) nucleate pool boiling prevailed for $q_{in,total} \geq$ 150 W; iii) the conditions in the evaporator transitioned from geyser boiling to nucleate pool boiling, haphazardly, for values of $q_{in,total}$ between 140 W to 150 W; iv) the overall thermal conductance of the GHP, C_{GHP}, increased with increasing values of, $q_{in,total}$, for a fixed value of fill ratio, *FR*; v) for a fixed value of $q_{in,total}$, C_{GHP} decreased with increasing values of *FR*; and vi) the highest values of C_{GHP} were obtained with *FR* = 100 %. These findings were discussed in detail in Chapter 4, Section 4.1. Based on these findings, it was decided to conduct the detailed investigations of the GBP with only one value of fill ratio, *FR* = 100 %.
3. Following the preliminary and repeatability runs, 12 benchmarking runs were conducted with *FR* = 100 %, to establish a suitable set of baseline results for the assessment of the proposed techniques for mitigating the GBP. These benchmarking runs were all conducted with the new LabVIEW code mentioned in the first point above, so the sampling rate of the set of 10 temperatures on the outer surface of the evaporator-tube wall was high enough to allow a proper FFT analysis of these measurements.

4. Some of the techniques available in the published literature for mitigating the GBP in GHPs were reviewed in Chapter 3, Subsection 3.6.1. Then, after due consideration of several possibilities, two key components were selected for the proposed techniques: a 60 $\times$ 60 stainless steel (SS 316) wire mesh (bought from *McMaster-Carr*) to create roughness on the inner surface of the evaporator-tube wall (intended to increase the number of nucleation sites and control the maximum bubble-departure diameter); and specially designed and fabricated stainless steel (SS 316) perforated disks (intended to serve as bubble-breakers, and prevent the formation of large Taylor bubbles within the evaporator section). These two key components were used (individually and in combination) to construct the following four proposed techniques to mitigate the GBP in the GHP: i) single-layer-wire-mesh (SLWM) technique; ii) triple-layer-wire-mesh (TLWM) technique; iii) eight-disks-single-layer-wire-mesh (8DSLWM) technique; and (iv) ten-disks (10D) technique. The details of these four proposed techniques for mitigating the GBP in the GHP were presented, along with discussions of the rationale behind each of them, in Chapter 3, Sections 3.6.2 – 3.6.6. *It is to be noted that the use of bubble-breakers to control GBP in GHPs has not been reported in the published literature. Thus, this is a novel (original) contribution of this work.*
5. Experiments were carried out with each of the four proposed techniques to mitigate the GBP in the GHP, using the new LabVIEW code for data acquisition and control. *The measured temperatures on the outer surface of the evaporator-tube wall were analyzed using a specially designed and implemented computer program (written using MATLAB R2018a) for FFT analyses of digital data in which the sampling times are not uniform.* As was mentioned in Chapters 1 and 3, *this appears to be the first use of the FFT technique for analyses of data related to the GBP in a <u>single-tube</u> GHP: thus, it is considered as another novel (original) contribution of this work.*
6. The main findings based on an examination of the results of the benchmarking experiments and the experiments with the four proposed techniques to mitigate the GBP in the GHP, and the FFT analyses mentioned above, were the following: i) the absolute amplitudes of the temperature oscillations about the mean levels were reduced by all four proposed techniques (compared to those encountered during the GBP in the benchmarking runs); ii) the 10D technique produced the highest values of C_{GHP} for 50 W $\leq q_{in,total} \leq$ 150 W; iii)

with respect to the reduction of the absolute amplitudes of the temperature oscillations about the mean levels, there 8DSLWM technique was slightly better than the 10D technique in some of the cases and the reverse was true in the other cases, and both these techniques were significantly better than the other two techniques; iv) the evaporator-wall temperature exceeded the safety cut-off temperature (85 ºC was the set value in the experiments with the mitigation techniques) for $q_{in,total}$ > 150 W (nominal) when the SLWM, 8DSLWM, and 10D techniques were deployed, and for $q_{in,total}$ > 95 W (nominal) when the TLWM technique was used (it was concluded that the most likely cause of this problem for the conditions considered in this work was the formation of a vapor film on the inner surface of the tube, in the gaps between it and the wire mesh or the outer edge of the perforated disks); and v) based on the findings given above, *the 10D technique was judged to be the best of the four proposed techniques for mitigating the GBP in the GHP*.

5.3 Recommendations for extensions of this work

The following extensions of this work are recommended:

1. It is necessary to solve the problem of local overheating of the evaporator-tube wall when using any one of the four proposed techniques for mitigating the GBP in the GHP. One possible way to do this is by attaching the wire mesh or the outer edge of the perforated disks to the inner surface of the tube (using a thin layer of a high-conductivity water-proof glue, for example) and thus eliminating the possibility of a vapor film in the gaps between inner surface of the tube and the wire mesh or the outer edge of the disks.
2. It would be useful to design, construct, and use a GHP with the entire evaporator section made of a borosilicate glass tube (akin to that used for the adiabatic section of the GHP used in this work), with a thin semi-transparent gold film heater attached to its outer surface. Such an evaporator section would allow full visualization of the boiling phenomena during the operation of the GHP. Guidance for the design and construction of such an evaporator section could be obtained from the works of Bernier and Baliga (1992) and Lagana and Baliga (2012).
3. The formulation and solution of simple mathematical models, based on empirical correlations for boiling, condensation, and forced-convection cooling, and classical

thermodynamics, may allow predictions and optimization of the GHP performance in the nucleate pool boiling regime. Guidance in this regard could be obtained from the works of Tien (1975), Carey (1992), Whalley (1996), Incropera and DeWitt (2002), Thome (2003), Jafari et al. (2016), and Guichet et al. (2019). It would be very worthwhile to implement such a model and fine-tune it by using the experimental data obtained in this work.

4. It would be worthwhile to design, setup, and conduct additional experiments to obtain data that would allow at least an approximate optimization of the 10D technique for mitigating the GBP in the GHP (perhaps, using several different perforation patterns and thicknesses of the disks, akin to that illustrated in Figures 3.15 and 3.16). As such experiments would involve several different parameters, guidance from Design of Experiments (DOE) techniques would be useful [Anderson and Whitcomb (2000); Antony (2014)].

In conclusion, the author would like to express the fond hope that the work presented in this thesis will encourage other researchers to pursue one or more of the extensions recommended above.

List of References

Abreu, S. L. and Colle, S. (2004). An experimental study of two-phase closed thermosyphons for compact solar domestic hot-water systems. *Solar Energy*, **76**, 141-145.

Alammar, A. A., Al-Dadah, R. K., and Mahmoud, S. M. (2018a). Effect of inclination angle and fill ratio on geyser boiling phenomena in a two-phase closed thermosiphon–Experimental investigation. *Energy Conversion and Management*, **156**, 150-166.

Alammar, A. A., Al-Dadah, R. K., and Mahmoud, S. M. (2018b). Experimental investigation of the influence of the geyser boiling phenomenon on the thermal performance of a two-phase closed thermosyphon. *Journal of Cleaner Production*, **172**, 2531-2543.

Alklaibi, A. M. (2008). Evaluating the possible configurations of incorporating the loop heat pipe into the air-conditioning systems. *International Journal of refrigeration*, **31**, 807-815.

Al-Marafie, A. M. R., Suri, R. K., and Maheshwari, G. P. (1989). Energy and power management in air-conditioned buildings in Kuwait. *Energy*, **14**, 557-562.

Al-Mudhaf, H. F., Abu-Shady, A. S. I., and Al-Khulaifi, N. M. (2013). Indoor and outdoor volatile organic compounds at office buildings in Kuwait. *Air, Soil and Water Research*, **6**, ASWR-S12153.

Alotaibi, S. (2011). Energy consumption in Kuwait: Prospects and future approaches. *Energy Policy*, **39**, 637-643.

Anderson, M. J. and Whitcomb, P. J. (2000). Design of experiments. *Kirk-Othmer Encyclopedia of Chemical Technology*, 1-22.

Antony, J. (2014). *Design of Experiments for Engineers and Scientists*. Elsevier, London, U.K.

ASME Standard PTC (2005). *Test Uncertainty*, 19.1-2005, American Society of Mechanical Engineers, New York, NY.

Azad, E., Bahar, F., and Moztarzadeh, F. (1985). Design of water-to-air gravity-assisted heat pipe heat exchanger. *Journal of Heat Recovery Systems*, **5**, 89-99.

Azad, E. and Geoola, F. (1984). A design procedure for gravity-assisted heat pipe heat exchanger. *Journal of Heat Recovery Systems*, **4**, 101-111.

Bernier, M. A. and Baliga, B. R. (1992). Visualization of upward mixed-convection flows in vertical pipes using a thin semitransparent gold-film heater and dye injection. *International Journal of Heat and Fluid Flow*, **13**, 241-249.

Bezrodnyi, M. K. and Beloivan, A. I. (1976). Investigation of the maximum heat-transfer capacity of closed two-phase thermosiphons. *Journal of Engineering Physics*, **30**, 377-383.

Boopathy, J. (2017). *Design, Implementation, and Characterization of a Gravity Heat Pipe*. M.Eng. Thesis, McGill University (Canada).

Burns, G. W. and Scroger, M. G. (1989). *The calibration of thermocouples and thermocouple materials*. U.S. Department of Commerce, National Institute of Standards and Technology, NIST Special Publication No. 250-35, Washington D.C.

Carey, V. (1992). *Liquid-Vapor Phase Change Phenomena, an Introduction of Vaporization and Condensation Processes in Heat Transfer Equipment.* Taylor & Francis, Washington D.C.

Casarosa, C., Latrofa, E., and Shelginski, A. (1983). The geyser effect in a two-phase thermosyphon. *International Journal of Heat and Mass Transfer*, **26**, 933-941.

Chen, J., Yang, S., Liao, S., and Cao, X. (2015). Experimental investigation of effective parameters on geyser periodicity in a vertical heated system. *Experimental Thermal and Fluid Science*, **68**, 163-176.

Chen, S. J., Reed, J. G., and Tien, C. L. (1984). Reflux condensation in a two-phase closed thermosyphon. *International Journal of Heat and Mass Transfer*, **27**, 1587-1594.

Chi, S. W. (1976). *Heat Pipe Theory and Practice*. Hemisphere, Washington D.C.

Choudhari, C. S. and Sapali, S. N. (2017). Performance investigation of natural refrigerant R290 as a substitute to R22 in refrigeration systems. *Energy Procedia*, **109**, 346-352.

Cole, R. (1967). Bubble frequency and departure volumes at subatmospheric pressures. *AIChE Journal*, *13*, 779-783.

Cotter, T. P. (1965). *Theory of heat pipes*. Los Alamos Scientific Laboratory of the University of California, Report No. LA-3246-MS, Albuquerque, New Mexico.

Danielewicz, J., Sayegh, M. A., Śniechowska, B., Szulgowska-Zgrzywa, M., and Jouhara, H. (2014). Experimental and analytical performance investigation of air to air two phase closed thermosyphon based heat exchangers. *Energy*, **77**, 82-87.

Davies R. M. and Taylor, G. I. (1950). The mechanics of large bubbles rising through extended liquids and through liquids in tubes. *Proc. Royal Society London A*, **200**, 375–390.

Dhir, V. K., Abarajith, H. S., and Li, D. (2007). Bubble dynamics and heat transfer during pool and flow boiling. *Heat Transfer Engineering*, **28**, 608-624.

Dhir, V. and Lienhard, J. (1971). Laminar film condensation on plane and axisymmetric bodies in nonuniform gravity. *ASME Journal of Heat Transfer*, **93**, 97-100.

Dobran, F. (1985). Steady-state characteristics and stability thresholds of a closed two-phase thermosyphon. *International Journal of Heat and Mass Transfer*, **28**, 949-957.

Dobson, M. and Chato, J. (1998). Condensation in smooth horizontal tubes. *ASME Journal of Heat Transfer,* **120**, 193-213.

Du, J., Bansl, P., and Huang, B. (2012). Simulation model of a greenhouse with a heat-pipe heating system. *Applied Enegry,* **93**, 268-276.

Dunn, P. and Reay, D. (2012). *Heat Pipes.* Elsevier, New York.

El Hajal, J., Thome, J., and Cavallini, A. (2003). Condensation in horizontal tubes, part 1: two-phase flow pattern map. *International Journal of Heat and Mass Transfer,* **46**, 3349-3363.

El-Genk, M. and Saber, H. (1997). Flooding limit in closed, two-phase flow thermosyphons. *International Journal of Heat and Mass Transfer,* **40**, 2147-2164.

El-Genk, M. and Saber, H. (1999). Determination of operation envelopes for closed, two-phase thermosyphons. *International Journal of Heat and Mass Transfer,* **42**, 889-903.

Elkholy, A. and Kempers, R. (2020). Experimental investigation of geyser boiling in a small diameter two-phase loop thermosyphon. *Experimental Thermal and Fluid Science*, 118, 110170-1-16.

Emami, M. R. S., Noie, S., Khoshnoodi, M., Hamed Mosavian, M., and Kianifar, A. (2009). Investigation of geyser boiling phenomenon in a two-phase closed thermosyphon. *Heat Transfer Engineering,* **30**, 408-415.

Faghri, A. (1995). *Heat Pipe Science and Technology.* Taylor & Francis, Boca Raton.

Faghri, A. (2012). Review and advances in heat pipe science and technology. *ASME Journal of Heat Transfer,* **134**, 123001(1-18).

Faghri, A. (2014). Heat pipes: review, opportunities and challenges. *Frontiers in Heat Pipes,* **5**, 1-48.

Firouzfar, E., Soltanieh, M., Noie, S., and Saidi, M. (2011). Application of heat pipe heat exchangers in heating, ventilation and air conditioning (HVAC) systems. *Scientific Research and Essays,* **6**, 1900-1908.

Fox, R. and McDonald, A. (1985). *Introduction to Fluid Mechanics, 3rd Edition.* John Wiley, New York.

Fritz, W. (1935). Berechnung des maximal volumes von dampfblasen. Physik. Zeitschr, 36, 379-384.

Frost, C. W. and Li, K. W. (1971). On the Rohsenow pool-boiling correlation. *ASME Journal of Heat Transfer,* **93**, 232-234.

Gadallah, A. and Siddiqui, K. (2015). Bubble breakup in co-current upward flowing liquid using honeycomb monolith breaker. *Chemical Engineering Science,* **131**, 22-40.

Gao, W., Qi, J., Yang, X., Zhang, J., and Wu, D. (2019). Experimental investigation on bubble departure diameter in pool boiling under sub-atmospheric pressure. *International Journal of Heat and Mass Transfer*, **134**, 933-947.

Griffith, P. (1962). Geysering in liquid-filled lines. *ASME- AlChE Heat Transfer Conference and Exhibit*, *Houston, USA*.

Grover, G. M. (1963). *Evaporation-Condensation Heat Transfer Device,* U.S. Patent No. 3229759.

Gaugler, R. (1944). *Heat Transfer Device.* US Patent 2350348.

Guichet, V., Almahmoud, S., and Jouhara, H. (2019). Nucleate pool boiling heat transfer in wickless heat pipes (two-phase closed thermosyphons): A critical review of correlations. *Thermal Science and Engineering Progress,* **13**, 100384-1-32.

Guo, W. and Nutter, D. (2009). An experimental study of axial conduction through a thermosyphon pipe wall. *Applied Thermal Engineering,* **29**, 3536-3541.

Hamzekhani, S., Maniavi Falahieh, M., and Akbari, A. (2014). Bubble departure diameter in nucleate pool boiling at saturation: Pure liquids and binary mixtures. *International Journal of Refrigeration,* **46**, 50-58.

Hamzekhani, S., Maniavi Falahieh, M., Kamalizadeh, M., and Salmaninejad, M. (2015). Bubble dynamics for nucleate pool boiling of water, ethanol and methanol pure liquids under the atmospheric pressure. *Journal of Applied Fluid Mechanics,* **8**, 893-898.

Haynes, F., Zarling, J., and Gooch, G. (1992). Performance of a thermosyphon with a 37-meter-long horizontal evaporator. *Cold Region Science and Technology,* **20**, 261-269.

Heris, S., Fallahi, M., Shanbedi, M., and Amiri, A. (2016). Heat transfer performance of two-phase closed thermosyphon with oxidized CNT/water nanofluids. *Heat and Mass Transfer,* **52**, 85-93.

Hewitt, G. (1998). Boiling, in W. Rohsenow, J. Hartnett, and Y. Cho, *Handbook of heat transfer, 3rd Edition* (Chapter 15). McGraw-Hill, New York.

Hijikata, K., Chen, S. J., and Tien, C. L. (1984). Non-condensable gas effect on condensation in a two-phase closed thermosyphon. *International Journal of Heat and Mass Transfer*, **27**, 1319-1325.

Hussein, H., El-Ghetany, H., and Nada, S. (2006). Performance of wickless heat pipe flat plate solar collectors having different pipes cross sections geometries and filling ratios. *Energy Conversion and Management,* **47**, 1539-1549.

Imura, H., Kusuda, H., Ogata, J., Miyazaki, T., and Sakamoto, N. (1979). Heat transfer in two-phase closed-type thermosyphons. *Transactions of Japan Society of Mechanical Engineers*, **45**, 712-722.

Imura, H., Sasaguchi, K., and Kozai, H. (1983). Critical heat flux in a closed two-phase thermosyphon. *International Journal of Heat and Mass Transfer,* **26**, 1181-1188.

Incropera, F. and DeWitt, D. (2002). *Fundamentals of Heat and Mass Transfer, 5th Edition.* John Wiley, New York.

Jafari, D., Franco, A., Filippeschi, S., and Marco, P. (2016). Two-phase closed thermosyphons: A review of studies and solar applications. *Renewable and Sustainable Energy Reviews,* **53**, 575-593.

Jafari, D., Filippeschi, S., Franco, A., and Di Marco, P. (2017). Unsteady experimental and numerical analysis of a two-phase closed thermosyphon at different filling ratios. *Experimental Thermal and Fluid Sciences*, **81**,164-174.

Jouhara, H., Fadhl, B., and Wrobel, L. (2016). Three-dimensional CFD simulation of geyser boiling in a two-phase closed thermosyphon. *International Journal of Hydrogen Energy,* **41**, 16463-16476.

Jouhara, H. and Robinson, A. (2010). Experimental investigation of small diameter two-phase closed thermosyphon charged with water, FC-84, FC-77 and FC-3283. *Applied Thermal Engineering,* **30**, 201-211.

Kalbfleisch, A. and Siddiqui, K. (2017). The effect of mesh-type bubble breaker on two-phase vertical co-flow. *International Journal of Multiphase Flow,* **94**, 1-16.

Khazaee, I., Hosseini, R., and Noie., S. (2010). Experimental investigation of effective parameters and correlation of geyser boiling in a two-phase closed thermosyphon. *Applied Thermal Engineering,* **30**, 406-412.

Kim, S. and No, H. (2000). Turbulent film condensation of high pressure steam in a vertical tube. *International Journal of Heat and Mass Transfer,* **43**, 4031-4042.

King, C. R. (1931). Perkins hermetic tube boiler. *The Engineer,* **152**, 405-406.

Kolev, N. I. (2007). *Multiphase Flow Dynamics 2: Thermal and Mechanical Interactions*. Springer, Berlin, Germany.

Kubín, M., Hirš , J., and Plášek, J. (2016). Experimental analysis of steam condensation in vertical tube with small diameter. *International Journal of Heat and Mass Transfer,* **94**, 403-410.

Kujawska, A., Zajaczkowski, B., Wilde, L., and Buschmann, M. (2019). Geyser boiling in a thermosyphon with nanofluids and surfactant solution. *International Journal of Thermal Sciences,* **139**, 195-216.

Kuncoro, H., Rao, Y., and Fukda, K. (1995). An experimental study on the mechanism of geysering in a closed two-phase thermosyphon. *International Journal of Multiphase Flow,* **21**, 1243-1252.

Lagana, A. and Baliga, B. R. (2012). Visualization of mixed convection flows in vertical, horizontal, and inclined pipes. *9th International Conference on Heat Transfer, Fluid Mechanics and Thermodynamics* (*HEFAT 2012*), 16-18 July, Malta.

Lataoui, Z. and Jemni, A. (2017). Experimental investigation of a stainless steel two-phase closed thermosyphon. *Applied Thermal Engineering,* **121**, 721-727.

Lee, Y. and Mital, U. (1972). A two-phase closed thermosyphon. *International Journal of Heat and Mass Transfer,* **15**, 1695-1707.

Lemmon, E. W., Huber, M. L., and McLinden, M. O. (2013). *Standard Reference Database 23: Reference Fluid Thermodynamic and Transport Properties - REFPROP*, Version 9.1, National Institute of Standards and Technology (NIST), Standard Reference Data Program, Gaithersburg.

Lin, S., Broadbent, J., and McGlen, R. (2005). Numerical study of heat pipe application in heat recovery system. *Applied Thermal Engineering,* **25**, 127-133.

Lin, T., Lin, W., Tsay, Y., and Wu, J. (1995). Experimental investigation of geyser boiling in an annular two-phase closed thermsyphon. *Internaional Journal of Heat and Mass Transfer,* **38**, 295-307.

Liu, J. and Wang, J. (1992). On the pulse boiling frequency in thermosyphons. *ASME Journal of Heat Transfer,* **114**, 290-292.

Liu, Y., Li, Z., Li, Y., Kim, S., and Jiang, Y. (2018). Experimental investigation of geyser boiling in a two-phase closed loop thermosyphon with high filling ratios. *International Journal of Heat and Mass Transfer,* **127**, 857-869.

Ma, C., Wu, X., and Gao, S. (2013). Analysis and applications of a two-phase closed thermosyphon for improving the fluid temperature distribution in wellbores. *Applied Thermal Engineering,* **55**, 1-6.

Marto, P. (1998). Condensation, in W. Rohsenow, J. Hartntt, & Y. Cho (Eds.), *Handbook of Heat Transfer, 3rd Edition* (Chapter 14). McGraw-Hill, New York.

Mathioulakis, E. and Belessiotis, V. (2002). A new heat-pipe type solar domestic hot water system. *Solar Energy,* **72**, 13-20

Mikic, B. and Rohsenow, W. (1969). A new correlation of pool-boiling data including the effect of heating surface characteristics. *ASME Journal of Heat Transfer,* **91**, 245-250.

Mikic, B., Rohsenow, W., and Griffith, P. (1970). On bubble growth rates. *International Journal of Heat and Mass Transfer,* **13**, 657-666.

Moran, M. J. and Shapiro, H. N. (1998). *Fundamentals of Engineering Thermodynamics, 3rd Edition*. John Wiley, New York.

Murphy, D. W. (1965). An experimental investigation of geysering in vertical tubes. In *Advances in Cryogenic Engineering*, 353-359. Springer, Boston, MA.

Naresh, Y. and Balaji, C. (2017). Experimental investigations of heat transfer from an internally finned two phase closed thermosyphon. *Applied Thermal Engineering,* **112**, 1658–1666.

Negishi, K. and Sawada, T. (1983). Heat transfer performance of an inclined two-phase closed thermosyphon. *International Journal of Heat and Mass Transfer,* **26**, 1207-1213.

Nethaji, N. and Mohideen, T. (2017). Application of heat pipes in HVAC systems: A review. *Advances in Natural and Applied Sciences,* **11**, 277-284.

Nguyen-Chi, H. and Groll, M. (1981). Entrainment or flooding limit in a closed two-phase thermosyphon. *Journal of Heat Recovery Systems,* **1**, 275-286.

Niro, A. and Beretta, G. (1990). Boiling regimes in a closed two-phase thermosyphon. *International Journal of Heat and Mass Transfer,* **33**, 2099-2110.

Noie, S. (2005). Heat transfer characteristics of a two-phase closed thermosyphon. *Applied Thermal Engineering,* **25**, 495-506.

Noie, S., Emami, M., and Khoshnoodi, M. (2007). Effect of inclination angle and filling ratio on thermal performance of a two-phase closed thermosyphon under normal operating conditions. *Heat Transfer Engineering,* **28**, 365-371.

Nukiyama, S. (1966). The maximum and minimum values of the heat Q transmitted from metal to boiling water under atmospheric pressure. *International Journal for Heat and Mass Transfer,* **9**, 1419-1433.

Nusselt, W. (1916). Die oberflachenkoondensation des wasserdampfes (rough translation of German to English: The surface condensation of water vapor). *Z. Ver. Deut. Ing.*, **60**, 541-546.

Pabón, N., Mera, J., Vieira, G., & Mantelli, M. (2019). Visualization and experimental analysis of geyser boiling phenomena in two-phase thermosyphons. *International Journal of Heat and Mass Transfer,* **141**, 876-890.

Park, Y., Kang, H., and Kim, C. (2002). Heat transfer characteristics of a two-phase closed thermosyphon to the fill charge ratio. *International Journal of Heat and Mass Transfer,* **45**, 4655-4661.

Pashkevich, R. and Muratov, P. (2015). Film condensation in a large diameter tube with upward steam flow. *International Journal of Heat and Mass Transfer,* **81**, 804-810.

Perkins, J. (1836). UK Patent No. 7059.

Peterson, G. (1998). Heat Pipes, in W. Rohsenow, J. Hartnett, and Y. Cho (Eds.), *Handbook of Heat Transfer, 3rd Edition* (Chapter 12). McGraw-Hill, New York.

Plesset, M. and Zwick, S. (1954). The growth of vapor bubbles in superheated liquids. *Journal of Applied Physics,* **25**, 493-500.

Prenger, F. C., Keddy, E. S., and Sena, J. T. (1986). Performance characteristics of gravity-assisted potassium heat pipes. *Journal of Spacecraft,* **23**, 407-410.

Ramirez, R. W. (1985). *The FFT – Fundamentals and Concept, Prentice Hall*. Englewood Cliffs, New Jersey, U.S.A.

Rayleigh, L. (1917). VIII. On the pressure developed in a liquid during the collapse of a spherical cavity. *The London, Edinburgh, and Dublin Philosophical Magazine and Journal of Science,* **34**, 94-98.

Reay, D., Kew, P., and McGlen, R. (2013). *Heat Pipes: Theory, Design and Applications, 6th Edition.* Butterworth-Heinemann, Oxford, U.K.

Reed, J. and Tien, C. L. (1987). Modeling of the two-phase closed thermosyphon. *ASME Journal of Heat Transfer,* **109**, 722-730.

Rohsenow, W. M. (1951). *A method of correlating heat transfer data for surface boiling of liquids.* Technical Report No. 5, M.I.T. Division of Industrial Cooporation, Cambridge, MA.

Rohsenow, W. M. (1973). Boiling, in J. Hartnett and W. Rohsenow (Eds.), *Handbook of Heat Transfer* (Chapter 13). McGraw-Hill, New York.

Rohsenow, W. M. (1985). Film condensation, in W. M. Rohsenow, J. Hartnett, and E. Ganic, *Handbook of Heat Transfer Fundamentals, 2nd Edition* (Chapter 11). McGraw-Hill, New York.

Rohsenow, W. M., Choi, H. Y., and Choi, H. Y. H. (1961). *Heat, Mass, and Momentum Transfer*. Prentice-Hall, New York.

Seban, R. and Faghri, A. (1984). Film condensation in a vertical tube with a closed top. *International Journal of Heat and Mass Transfer,* **27**, 944-948.

Seban, R. and Hodgson, J. (1982). Laminar film condensation in a tube with upward vapor flow. *International Journal of Heat and Mass Transfer,* **25**, 1291-1300.

Shabgard, H., Robak, C., Bergman, T., and Faghri, A. (2012). Heat transfer and exergy analysis of cascaded latent heat storage with gravity-assisted heat pipes for concentrating solar power applications. *Solar Energy,* **86**, 816-830.

Shabgard, H., Xiao, B., Faghri, A., Gupta, R., and Weissman, W. (2014). Thermal characteristics of a closed thermosyphon under various filling conditions. *International Journal of Heat and Mass Transfer,* **70**, 91-102.

Shabgard, H., Allen, M., Sharifi, N., Benn, S., Faghri, A., and Bergman, T. (2015). Heat pipe heat exchangers and heat sinks: Opportunities, challenges, applications, analysis, and state of the art. *International Journal of Heat and Mass Transfer,* **89**, 138–158.

Shanbedi, M., Heris, S., Amiri, A., and Baniadam, M. (2014). Improvement in heat transfer of a two-phased closed thermosyphon using silver-decorated MWCNT/water. *Journal of Dispersion Science and Technology,* **35**, 1086-1096.

Shanbedi, M., Heris, S., Baniadam, M., Amiri, A., and Maghrebi, M. (2012). Investigation of heat-transfer characterization of EDA-MWCNT/DI-water nanofluid in a two-phase closed thermosyphon. *Industrial & Engineering Chemistry Research,* **51**, 1423-1428.

Shiraishi, M., Kikuchi, K., and Yamanishi, T. (1981). Investigation of heat transfer characteristics of a two-phase closed thermosyphon. *Journal of Heat Recovery Systems*, **1**, 287-297.

Smith, K., Siedel, S., Robinson, A., and Kempers, R. (2016). The effects of bend angle and fill ratio on the performance of a naturally aspirated thermosyphon. *Applied Thermal Engineering,* **101**, 455-467.

Smith, K., Kempers, R., and Robinson, A. (2018a). Confinement and vapour production rate influences in closed two-phase reflux thermosyphons Part A: flow regimes. *International Journal of Heat and Mass Transfer,* **119**, 907-921.

Smith, K., Robinson, A., and Kempers, R. (2018b). Confinement and vapour production rate influences in closed two-phase reflux thermosyphons Part B: Heat transfer. *International Journal of Heat and Mass Transfer,* **120**, 1241-1254.

Solomon, A. B., Daniel, V. A., Ramachandran, K., Pillai, B. C., Singh, R. R., Sharifpur, M., and Meyer, J.P. (2017). Performance of a two-phase closed thermosiphon with a thin porous copper coating. *International Communications in Heat and Mass Transfer*, **82**, 9-19.

Stephan, K. (1992). *Heat Transfer in Condensation and Boiling.* Springer-Verlag, New York.

Stephan, K. and Abdelsalam, M. (1980). Heat-transfer correlations for natural convection boiling. *International Journal of Heat and Mass Transfer,* **23**, 73-87.

Táboas, F., Vallès, M., Bourouis, M., and Coronas, A. (2007). Pool boiling of ammonia/water and its pure components: comparison of experimental data in the literature with the predictions of standard correlations. *International Journal of Refrigeration,* **30**, 778-788.

Taylor, B. N. and Kuyatt, C. E. (1994). Guidelines for the Evaluation and Expression of Uncertainty in NIST Measurement Results. *NIST Technical Note 1297*, National Institute of Standards and Technology (NIST), Gaithersburg, MD.

Tecchio, C., Oliveira, J., Paiva, K., Mantelli, M., Galdofi, R., and Ribeiro, L. (2017). Geyser boiling phenomenon in two-phase closed loop thermosyphons. *International Journal of Heat and Mass Transfer,* **111**, 29-40.

Thome, J. (2003). On recent advances in modeling two-phase flow and heat transfer. *Heat Transfer Engineering,* **24**, 46-59.

Thumm, S., Philipp, C., and Gross, U. (2001). Film condensation of water in a vertical tube with countercurrent vapour flow. *International Journal of Heat and Mass Transfer,* **44**, 4245-4256.

Tien, C. L. (1975). Fluid mechanics of heat pipes. *Annual Review Fluid Mechanics,* **7**, 167-185.

Tritton, D. J. (1988). *Physical Fluid Dynamics*, 2nd Edition, Oxford Univ. Press, Oxford, U.K.

Tsai, T.-E., Wu, H.-H., Chang, C.-C., and Chen, S.-L. (2010). Two-phase closed thermosyphon vapor-chamber system for electronic cooling. *International Communications in Heat and Mass Transfer,* **37**, 484-489.

Vieira, G. C., Flórez M, J. P., and Mantelli, M. B. H. (2020). Improving heat transfer and eliminating geyser boiling in loop thermosyphons: Model and experimentation. *International Journal of Heat and Mass Transfer*, **156**, 119832-1-15.

Wadowski, T., Akbarzadeh, A., and Johnson, P. (1991). Characteristics of a gravity-assisted heat pipe-based heat exchanger. *Heat Recovery Systems,* **11**, 69-77.

Wang, J. and Ma, Y. (1991). Condensation heat transfer inside vertical and inclined thermosyphons. *ASME Journal of Heat Transfer,* ***113***, 777-780.

Wang, X., Wang, Y., Chen, H., and Zhu, Y. (2018). A combined CFD/visualization investigation of heat transfer behaviors during geyser boiling in two-phase closed thermosyphon. *International Journal of Heat and Mass Transfer,* **121**, 703-714.

Whalley, P. (1996). *Two-Phase Flow and Heat Transfer.* Oxford University Press, U.K.

White, F.W. (2015). *Fluid Mechanics*, *8th Edition*, McGraw-Hill, New York.

Xia, G., Wang, W., Cheng, L., and Ma, D. (2017). Visualization study on the instabilities of phase-change heat transfer in a flat two-phase closed thermosyphon. *Applied Thermal Engineering,* **116**, 392-405.

Xu, J. and Goering, D. (2008). Experimental validation of passive permafrost cooling systems. *Cold Regions Science and Technology,* **53**, 283-297.

Yang, F., Yuan, X., and Lin, G. (2003). Waste heat recovery using heat pipe heat exchanger for heating automobile using exhaust gas. *Applied Thermal Engineering,* **23**, 367-372.

Zeng, L., Klausner, J., and Mei, R. (1993). A unified model for the prediction of bubble detachment diameter in boiling systems - I. Pool boiling. *International Journal of Heat and Mass Transfer,* **36**, 2261-2270.

Zhang, X. and Che, H. (2013). Reducing heat loss of fluids in heavy oil wellbore using two-phase closed thermosyphon sucker rod. *Energy,* **57**, 352-358.

Zhao, Z., Jiang, P., Zhou, Y., & Zhang, Y. (2019). Heat Transfer characteristics of two-phase closed thermosyphons modifies with inner surfaces of various wettabilities. *International Communications in Heat and Mass Transfer*, **103**, 100-109.

Zhou, X. and Collins, R. (1991). Measurement of condensation heat transfer in a thermosyphon. *International Journal of Heat and Mass Transfer,* **34**, 369-376.